QUANTITATIVE CHARACTERIZATION AND MODELING OF THE MICROSTRUCTURE OF SOLID OXIDE FUEL CELL COMPOSITE ELECTRODES

A Thesis

Presented to

The Academic Faculty

by

Shenjia Zhang

In Partial Fulfillment

of the Requirements for the Degree

Doctor of Philosophy in the

School of Material Science and Engineering

Georgia Institute of Technology

December 2010

QUANTITATIVE CHARACTERIZATION AND MODELING OF THE MICROSTRUCTURE OF SOLID OXIDE FUEL CELL COMPOSITE ELECTRODES

Approved by:

Dr. Arun M. Gokhale, Advisor
School of Material Science and Engineering
Georgia Institute of Technology

Dr. Meilin Liu
School of Material Science and Engineering
Georgia Institute of Technology

Dr. Hamid Garmestani
School of Material Science and Engineering
Georgia Institute of Technology

Dr. Kennith A. Gall
School of Materials Science and Engineering
Georgia Institute of Technology

Dr. Karl I. Jacob
School of Polymer, Textile & Fiber Engineering
Georgia Institute of Technology

Date Approved: August 11,2010

ACKNOWLEDGEMENTS

Foremost, I would like to give most sincere thanks to my advisor Dr. Arun Gokhale for his constant support, abundant help and invaluable advice for my research and study in Georgia Tech. With patience and motivation, he has given me timely guidance in the critical stages of my research and especially towards the completion of this thesis. I would also like to thank Dr. Meilin Liu for his help and support in the collaboration of our research. He has given me invaluable advice in the field of solid oxide fuel cells. The research that leads to this thesis would not be possible without his support.

I would express my gratitude towards my colleagues in the Lab of Stereology as well in Dr. Liu's group of solid oxide fuel cells. I would like to give thanks to Song Gi Lee, Arun Sreeranganathan, Hapreet Singh and Yuxiong Mao for sharing their experience, knowledge and insights in their fields of expertise. I would like to thank Zhe Cheng, Matt Lynch and Lei Yang for their help from the field of solid oxide fuel cells. Their collaborations are of critical importance to the research that leads to this thesis. I would also give thanks to my committee members, Dr. Hamid Garmestani, Dr. Kenneth A. Gall, Dr. Karl I. Jacob and Dr. Meilin Liu and for their invaluable advice and support.

Financial support of this research comes from Division of Materials Research, U.S. National Science Foundation (grants number DMR 0404668 and 0813630). The support is gratefully acknowledged.

Last but most importantly, I would like to thank my wife Huayu Liu for her caring love and selfless support, which makes my life, study and research in Georgia Tech an enjoyable experience.

TABLE OF CONTENTS

Page

LIST OF TABLES

Page

LIST OF FIGURES

Page

LIST OF SYMBOLS

λ the length of each circular triple phase boundary in Sunde's [4] random packing sphere model

C_{YSZ}: the probability that the electrolyte particle belongs to a connected ion pathway

C_{LSM}: the probability that the electronic powder particle belongs to an electron conducting chain pathway

θ_i: the volume fraction of phase i

A_A: the fraction of the area of representative metallograhphic plane occupied by the phase of interest

I_L: the number of intersections between the test lines and the surfaces of interest per unit test line length

L_A: the number of intersections between the test lines and the surfaces of interest per unit test line length

P_P: the fraction of number of test points contained in the phase of interest

S_V, S_V^{ij}: area of the surface/interface between phase i and phase j per unit volume

$P_{ij}(r,\theta,\phi)$: the two-point correlation function between phase i and j, defined as the probability that a randomly placed line segment of length r and orientation (θ,ϕ) has one of its end contained in phase i and the other in phase j

P_A: number of triple point junctions observed per unit area of the metallographic plane

$(\theta_Y)_{ex}$, $(\theta_L)_{ex}$, $(\theta_P)_{ex}$: volume fraction of YSZ, LSM and porosity in the *extended* microstructure

θ_Y , θ_L , θ_P: volume fraction of YSZ, LSM and porosity in the *real* microstructure

α: relation proportions of YSZ and LSM, $(\theta_Y)_{ex}/(\theta_L)_{ex}$

$(L_{TPB})_{ex}$: total length of triple phase boundaries in the *extended* microstructure per unit volume of the microstructural space

L_{TPB}: total length of triple phase boundaries in the *real* microstructure per unit volume of the microstructural space

$(S_{YZ})_{ex}$, $(S_{LM})_{ex}$: total surface area of YSZ and LSM in the extended microstructure

S_{YP} , S_{LP}: total surface areas of YSZ/porosity surfaces and LSM/porosity surfaces per unit volume in the real microstructure

$\langle S_Y \rangle$, $\langle S_L \rangle$: mean surface areas of YSZ and LSM particles

$\langle V_Y \rangle$, $\langle V_L \rangle$: mean volume YSZ and LSM particles

$\langle D_Y{}^2 \rangle, \langle D_L{}^2 \rangle$: mean squared caliper diameters of YSZ and LSM particles

$\langle D_Y{}^3 \rangle, \langle D_L{}^3 \rangle$: mean cubed caliper diameters of YSZ and LSM particles

K_{1Y}, K_{1L}: surface area shape factors of YSZ and LSM particles.

K_{2Y}, K_{2L}: volume shape factors of YSZ and LSM particles.

D_Y, D_L: caliper diameters of YSZ and LSM particles

CV_Y, CV_L: coefficient of variance of YSZ and LSM particle size distributions.

γ_Y , γ_L : skewness of the YSZ and LSM particle size distributions

N_Y, N_L : numbers of YSZ and LSM particles per unit volume

$F_1(\alpha)$: the function that reflects the dependence of *TPB* on α

$F_2(\theta_P)$: the function that reflects the dependence of *TPB* on θ_P

$F_3(K)$: the function that reflects the dependence of TPB on K(morphology/shape factors).

$F_4(CV,\gamma)$: the function that reflects the dependence of TPB on CV and γ.

S_1: the total area of the surfaces of interest

$\sum$: total volume of the microstructure of the specimen

S_{probe}: total area of the probe surfaces

L_{total}: total length of the lines of intersections between the surfaces of interest and the probes

L_A: total length of the boundary traces observed in random two-dimensional sections per unit

d_o: initial density of the random packing sphere model

d: final density of the random packing sphere model

Z: mean coordination number

ϕ_{io} : volume fraction of the ionic conductor(i.e. YSZ) in the random packing sphere model

H: local mean curvature

χ: local dihedral angle of an edge element

S_{cyl}: surface area of a cylinder

V_{cyl}: volume of a cylinder

R: radius of a cylinder

L: height of a cylinder

$L(P)$: the phase assignment of a voxel P

M: the orientation matrix returned by Arvo's [5] algorithm

$\vec{\mathbf{R}}$: the set of vectors specifying surface points on a convex shaped particle

$\mathbf{d}^{i}(P)$: the distance vector between P and the nearest particle center of phase i

LISTS OF ABBREVIATIONS

SOFC	solid oxide fuel cell
TPB	triple phase boundary
YSZ	yittria-stablised zirconia
LSM	strontium-doped lanthanum manganite
BZCY	$Ba(Zr_{0.1}Ce_{0.7}Y_{0.2})O_{3-\delta}$
LSCF	$La_{1-x}Sr_xCo_{1-x}Fe_xO_3$
AFM	atomic force microscopy
SEM	scanning electron microscope
BSE	basckscatter electron imaging
EDS	energy dispersive X-Ray spectroscopy

SUMMARY

Three-phase porous composites containing electrolyte (ionic conductor), electronic conductor, and porosity phases are frequently used for solid oxide fuel cell (SOFC) electrodes. Performance of such electrodes is microstructure sensitive. Topological connectivity of the microstructural phases and total length of triple phase boundaries are the key microstructural parameters that affect the electrode performance. These microstructural attributes in turn depend on numerous process parameters including relative proportion, mean sizes, size distributions, and morphologies of the electrolyte and electronic conductor particles in the powder mix used for fabrication of the composites. Therefore, improvement of the performance of SOFC composite electrodes via microstructural engineering is a complex multivariate problem that requires considerable input from microstructure modeling and simulations. This dissertation presents a new approach for geometric modeling and simulation of three-dimensional (3D) microstructure of three-phase porous composites for SOFC electrodes and provides electrode performance optimization guidelines based on the parametric studies on the effects of processing parameters on the total length and topological connectivity of the triple phase boundaries. The model yields an equation for total triple phase boundary length per unit volume (L_{TPB}) that *explicitly* captures the dependence of L_{TPB} on relative proportion of electrolyte and electronic conductor phases; volume fraction of porosity; and mean size, coefficient of variation, and skewness of electrolyte and electronic conductor particle populations in the initial powder mix. The equation is applicable to electrolyte and electronic conductor particles of any convex shapes and size distributions. The model is validated using experimental measurements performed in this

research as well as the measurements performed by other researchers. Computer simulations of 3D composite electrode microstructures have been performed to further validate the microstructure model and to study topological connectivity of the triple phase boundaries in 3D microstructural space. A detailed parametric analysis reveals that (1) non-equiaxed plate-like, flake-like, and needle-like electrolyte and electronic conductor particle shapes can yield substantially higher L_{TPB}; (2) mono-sized electrolyte and electronic conductor powders lead to higher L_{TPB} as compared to the powders having size distributions with large coefficients of variation; (3) L_{TPB} is inversely proportional to the mean sizes of electrolyte and electronic conductor particles; (4) a high value of L_{TPB} is obtained at the lowest porosity volume fraction that permits sufficient connectivity of the pores for gas permeability; and (5) L_{TPB} is not sensitive to the relative proportion of electrolyte and electronic conductor phases in the composition regime of interest in composite electrode applications.

CHAPTER 1

INTRODUCTION

1.1 Motivation and Objectives

A fuel cell is an energy conversion device that directly converts chemical energy to electrical energy via electrochemical reactions. Fuel cells are classified on the basis of the material used for the electrolyte. Solid oxide fuel cells (SOFCs) are class of fuel cells that utilize solid oxide electrolytes. Advantages of SOFCs over other categories of fuel cells include low emissions and fuel flexibility [1, 6]. Nonetheless, to be economically competitive and commercially viable, the performance of SOFCs must be further improved and the cost must be reduced. The performance of SOFCs is often limited by the *interfacial energy losses* arising from the resistances to charge and mass transfer along surfaces; across interfaces; and through the electrodes, in particular, through the cathode where oxygen reduction takes place [7]. Therefore, it is of interest to study the factors that govern these energy losses so that practical strategies can be developed to minimize the losses in order to improve the performance.

Yttria-stabilized zirconia (YSZ) is the most commonly used electrolyte material in SOFCs. Lanthanum doped strontium manganite (LSM), is the frequently used cathode material for the SOFCs containing YSZ electrolyte because of its thermal and chemical compatibility with YSZ. However, at low operating temperatures (typically, below 800^{o}C), poor ionic conductivity of LSM limits its catalytic activity. As a result, the electrochemical oxygen reduction reaction primarily occurs at the one-dimensional lineal junctions common to the electronic conductor (LSM), electrolyte (YSZ), and oxidant (air or oxygen), called triple phase boundaries [8, 9]. Consequently, the low temperature catalytic activity (and hence the performance) of the SOFC cathodes can be improved by increasing the total length of the triple phase boundaries that are active sites for the core electrochemical oxygen reduction reaction. In the SOFCs having monolithic electronic conductor (such as LSM) cathode, the triple phase boundary length is very small because the triple phase boundaries exist only at the junction of the electrolyte (YSZ), electronic conductor (LSM), and oxidant (air or oxygen). Therefore, an important approach to increase the catalytic activity in the SOFC cathodes (and hence the performance of SOFCs) is to increase the total length of the triple phase boundaries where the electrochemical oxygen reduction reaction occurs. This can be achieved through the use of porous *mesoscale (or nanoscale) composite cathodes* containing three phases, namely, electronic conductor (such as LSM), electrolyte (such as YSZ), and porosity containing oxidant (such as air or oxygen) [10-13]. Similarly, the electrochemical activity of SOFC *anodes* can be also improved by using porous composites containing electronic conductor (such as Ni), electrolyte (such as YSZ), and porosity (containing fuel such as hydrogen). The performance of porous composite electrodes (cathodes as well as anodes) can be further enhanced by increasing the total length of the triple phase boundaries in their three-dimensional microstructures.

Porous composite electrodes can be fabricated by using well-known powder processing techniques [14-16]. Total triple phase boundary length in porous composite electrodes depends on the volume fractions and numerous other geometric microstructural attributes of the constituent phases. As a result, the performance of porous composite electrodes is *microstructure sensitive* [7, 14, 15, 17, 18]. The microstructure is in turn governed by the processing conditions and geometric characteristics of the initial electrolyte and electronic conductor powders [14, 15, 18]. Therefore, experimental and modeling/simulation studies of these processing-microstructure-properties relationships are of fundamental interest for the development of science and technology of SOFCs having porous composite cathodes.

There have been numerous analytical modeling [4, 19] and computer simulation [3, 4, 19-26] studies on various aspects of processing-microstructure-performance relationships in the porous composite SOFC electrodes. Nonetheless, most of the modeling and simulation studies reported in the literature assume that the electrolyte and electronic conductor particles are spherical and/or mono-sized. Therefore, these investigations do not capture the effects of the electrolyte and electronic conductor particle shapes/morphologies and the distribution attributes such as the variance and the skewness of the size distributions in the initial powder mix on the total triple phase boundary length. On the other hand, the major difficulty in the experimental studies on *unbiased* and *quantitative* processing-microstructure-performance relationships in the porous composite SOFC cathodes has been lack of convenient microscopy techniques that can enable simultaneous observation all *three* phases and *quantitative* characterization of triple phase boundaries in the microstructures of interest [27, 28]. Accordingly, the major objectives of this research are as follows.

(1) To develop atomic force microscopy (AFM) and digital image processing based technique for direct simultaneous experimental observations of all three phases (YSZ,

LSM, and porosity) and triple phase junctions in the porous composite cathode microstructures.

(2) To develop and apply stereological and image analysis techniques for *unbiased* quantitative measurements of total triple phase boundary length in the three-dimensional porous composite cathode and anode microstructures of interest.

(3) To develop a general and flexible analytical model to predict the total triple phase boundary length in the three-phase porous composite microstructures; to utilize the model to perform detailed parametric studies on the effects volume fractions, mean sizes, variance and skewness of the size distributions, and shapes/morphologies of electrolyte and electronic conductor powders in the powder mix on the total triple phase boundary length; and to validate the model via comparison of the predictions of the model with the quantitative experimental data.

(4) To perform computer simulations to validate the analytical model; to visualize the simulated three-dimensional microstructures; and to determine the extent of *topologically* connected triple phase boundary length in the modeled three-phase porous composites and its dependence on the geometric attributes of initial powder mix.

This dissertation will present a new modeling approach for the calculation of the total triple phase boundary length in the SOFC composite electrodes and provide cell performance optimization guidelines based on the parametric studies on the effects of process parameters on the length and topological connectivity of the triple phase boundaries.

1.2 Organization of the Thesis

The dissertation is composed of seven chapters. The next chapter presents background and literature review on the topics that are pertinent to the material systems, characterization techniques, and modeling approaches. The third chapter is devoted to the development of microscopy and image analysis based technique for observation and quantitative characterization of the triple phase boundaries and its application to characterization of two types of SOFC cathodes and YSZ-Ni anodes. Mathematical formulation of the stochastic geometry based analytical model of three-phase microstructure that predicts triple phase boundary length and detailed parametric study on the windows of the processing conditions that can optimize the triple phase boundary length are given in the fourth chapter. The fifth chapter describes the simulation algorithm for a voxel-based implementation of the model formulated in chapter 4. The sixth and seventh chapters present computer simulations and analysis of the topological connectivity of the triple phase boundaries in the three-phase porous composite microstructures, respectively. The last chapter provides summary and conclusions of this research.

CHAPTER 2

BACKGROUND AND LITERATURE REVIEW

Central objectives of this research are to develop the experimental techniques for observation and quantitative characterization of SOFC porous composite electrode microstructures with emphasis on the characterization of the triple phase boundaries; to develop a general geometric model for the triple phase boundaries; and to simulate and visualize three-dimensional porous composite electrode microstructures and quantify their topology. The present research builds on the existing literature on SOFCs, current stereological and image analysis techniques for microstructure characterization, and geometric microstructure modeling and simulation methodologies reported in the literature. Accordingly, a brief literature review on the basic concepts of fuel cells and material issues relevant to SOFCs is presented in the next section, which is followed by a critical analysis of the existing models and simulations of SOFC porous composite electrode microstructures and the processing-microstructure-properties relationships. The stereological and digital image analysis techniques relevant to the present research are reviewed in the last section.

2.1 Fuel Cells

A fuel cell is an electrochemical energy conversion device that *directly* converts chemical energy to electrical energy through electrochemical reactions between a fuel (for example, hydrogen) and an oxidant (for example, air or oxygen) [1]. The main components of a fuel cell are anode, electrolyte, and cathode (see Figure 1(a)). The electrochemical reactions occur at the interfaces of the electrodes and the electrolyte. Reduction of oxygen occurs at the cathode that leads to formation of oxygen ions. Fuel cell electrolyte is an *ionic conductor*, and an electronic *insulator*. Therefore, the oxygen ions travel through the electrolyte and reach the anode. The oxygen ions that reach the anode combine with the fuel and create electrons and reaction products like water or CO_2 through an electrochemical reduction reaction. The electrons produced by the oxidation of the fuel cannot pass through the electrolyte; they travel through a wire connected to cathode creating an electrical current[1]. Thus, the two electrochemical reactions lead to consumption of the fuel; formation of reaction products such as water or carbon dioxide; and generation of electrical current. Continuous fuel and oxidant flows are essential for operation of a fuel cell, and therefore, unlike a battery, a fuel cell is an open thermodynamic system. There are numerous varieties of fuel cells. Fuel cells are classified on the basis of the material used for the electrolyte. Table 1 gives a brief summary of important categories of fuel cells [6]. The present research only concerns solid oxide fuel cells. The basic concepts and materials issues related to the solid oxide fuel cells are described in the next section.

2.2 Solid Oxide Fuel Cells

SOFC is a class of fuel cells that utilize solid-state oxide electrolytes. SOFCs have numerous potential applications ranging from auxiliary power units in vehicles to stationary power generation units with outputs ranging from 100 W to 2 MW [6]. A

---

[1] This process describes the mechanism of a typical oxygen ion conducting electrolyte based fuel cell; the mechanism of an proton conducting electrolyte based fuel cell(see Figure 1(a)) is different in that: (1) proton flows through the electrolyte and (2) products (e.g. water and CO_2) are produced at the cathode.

stand-alone SOFC has an energy efficiency of 50% to 60%, while the thermally combined power generator has an efficiency of 80%, which is significantly higher than any available power source [1]. SOFCs are appealing because they are compact; they have high efficiency and low emissions; they can utilize a wide variety of fuels (for example, hydrogen, butane, methanol, and other petroleum products); they do not require a catalyst; they do not have moving parts; and they do not contain any liquids that may cause flooding in the electrodes [1]. The main disadvantage of the SOFCs is high operating temperatures (typically, 800^{o}C or higher) that lead to long start-up times and serious mechanical/chemical compatibility and material degradation issues [6]. Therefore, to produce economically competitive and commercially viable SOFCs, the technology must be developed to improve the performance (efficiency) of the SOFCs at low temperatures so that they can be operated at lower temperatures. Microstructural engineering of SOFC components that can improve the cell performance is of considerable significance; some of these microstructural aspects are of core interest in the present research. The main components of a SOFC are electrolyte, anode, and cathode. The material and microstructural aspects of these components are briefly reviewed below.

2.2.1 Solid Electrolyte

As mentioned earlier, SOFCs utilize solid-state oxide electrolytes. The electrolyte material substantially influences the performance of the SOFC. A solid electrolyte suitable for SOFCs must have high ionic conductivity but should be an insulator for electronic conduction; it should have chemical stability at high temperatures in both oxidizing and reducing environments; it should be chemically compatible with anode and cathode materials and should have thermal expansion coefficient comparable to that of the electrode materials; and it should have high resistance to thermal cycling [29]. Yttria stabilized zirconia (YSZ), scandia stabilized zirconia (ScSZ), and gadolinium doped ceria (CGO) are oxygen ion conducting solid electrolytes that satisfy these requirements [30, 31]. CGO has higher ionic conductivity than YSZ, but it has higher electronic conductivity than YSZ at high temperatures, which is undesirable [30]. ScSZ is more expensive than YSZ due to the presence of Scandium in ScSZ. As a result, YSZ is the most commonly used solid-state electrolyte material in SOFCs.

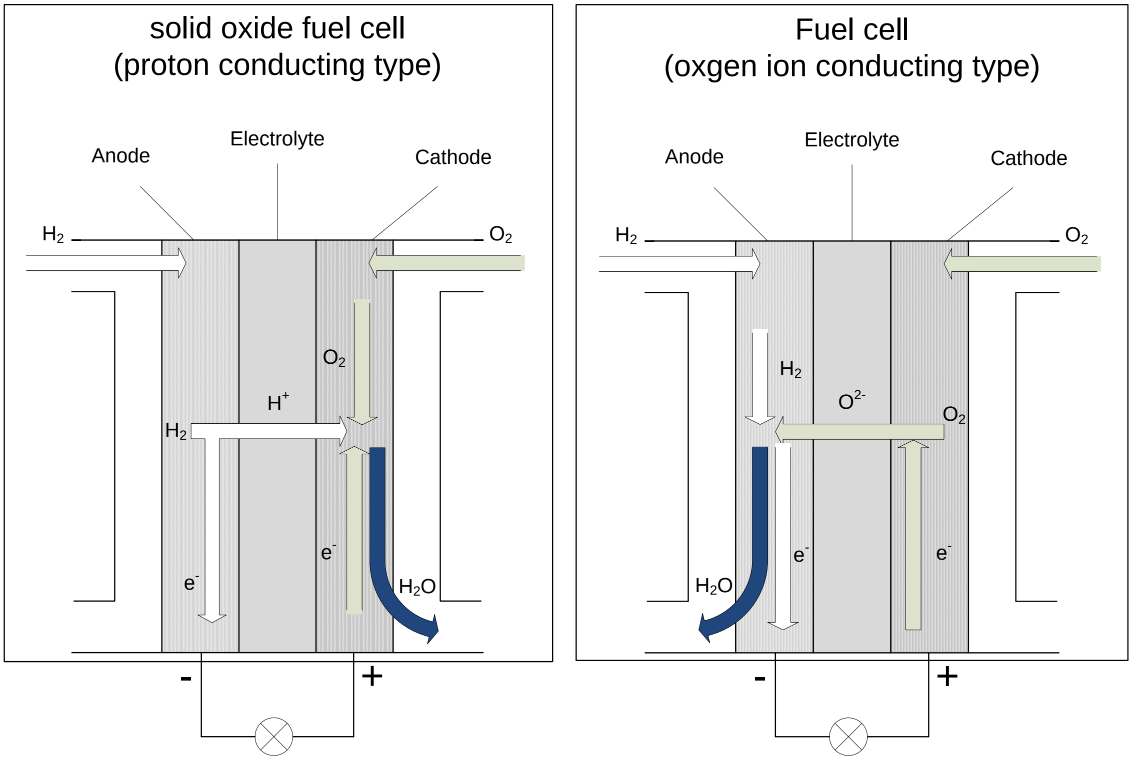

(a) (b)

Figure 1 Schematic of a (a) proton conducting electrolyte based fuel cell and (b) oxygen ion conducting electrolyte based fuel cell.

Table 1 A summary of fuel cells[1, 2]

	alkaline fuel cell	**proton exchange membrane fuel cell**	**direct methane fuell cell**	**phosphoric acid fuel cells**	**molten carbonate fuel cell**	**Ssolid oxide fuell cell**
Cathode material	Carbon paper or carbon cloth supported Pt				NiO	LSM, LSCF*
Anode material	Carbon supported Pt	Carbon supported Pt/Ru	Carbon supported Pt/Ru	Carbon supported Pt	Ni/Al or Ni/Cr alloys	YSZ,BZCY*
Electrolyte material	KOH or NaOH solution	Nafion	Nafion	Phosphoric acid in SiC matrix	LiK or LiNa carbonate in $LiAlO_2$ supported by Al_2O_3 fibers	Ni*
Operation temperature (°C)	60-90	80-110	80-110	160-200	600-800	800-1000 (500 possible)
Fuel type	Pure hydrogen	hydrogen	methanol	hydrogen	CO/H_2	CO/H_2
Advantages	● Simple design	● Faster startup ● No leakage of electrolyte ● Portable	● Methanol is easy to store	● CO and CO_2 tolerant ● CHP application	● High efficiency ● Internal reforming possible ● CO and CO_2 tolerant ● No Pt	● High efficiency ● Internal reforming possible, ● CO and CO_2 tolerant ● No electrolyte creeping ● No Pt
Disadvantages	● CO_2 intolerant	● CO poisoning ● Water management ● Requiring Pt	● CO poisoning ● Water management ● Methanol migration ● Requiring Pt	● Electrolyte leak ● Phosphoric acid conductivity low ● Requiring Pt	● Longer startup ● Electrolyte creep ● NiO creep cause short circuit	● Longer start up ● High temperature challenge materials ● Carbon/sulfur poisoning

Recently a new type solid electrolyte which conducts hydrogen ions (or protons) has emerged and drawn interest from researchers [32]. The activation energy for the motion of hydrogen ions is lower than that of oxygen ions, which gives hydrogen ion conductors a higher conductivity than oxygen ion conductors. The proton conductor $Ba(Zr_{0.1}Ce_{0.7}Y_{0.2})O_{3-\delta}$ shows adequate proton conductivity over a range of operation temperatures and is compatible with numerous cathode materials [33-35]. Yang [36] has also shown that proton conductor based SOFCs is more tolerant to sulfur content in the fuel, which has remained a major challenge for oxygen conductor based SOFCs.

2.2.2 Anode

In a solid oxide fuel cell, oxidation of fuel takes place at the interface of the anode and the electrolyte. The anode is the thickest component of SOFC; it provides mechanical support and strength to the fuel cell. The anode must be porous and should have topologically connected porosity because the fuel must continuously flow through the pores in the anode to electrolyte for the fuel cell to function. In addition, unlike the electrolyte, the anode must be an electronic conductor because it must conduct the electrons generated by the oxidation reaction to the external circuit for generation of electrical current.

Ni, among numerous metals studied [6], has been used most widely in the anodes of SOFC. Ni has excellent high temperature corrosion and oxidation resistance; it has very good high temperature strength and creep resistance; and it is an excellent electronic conductor. Porous Ni having topologically connected porosity permits flow of gases and therefore can be used for SOFC anodes. Composites containing Ni, YSZ, and porosity phases are most commonly used for SOFC anodes [37, 38]. The porous Ni-YSZ composite anodes can be made by using well-known powder processing techniques [37, 38]. Ni is an electronic conductor, whereas YSZ is an ionic conductor. Therefore, if the Ni and YSZ phases are both topologically connected in the three-dimensional (3D) microstructure, then the Ni-YSZ composite anode conducts both electrons (due to Ni) and ions (due to YSZ). In such anode, the oxygen ions are conducted from the cathode and the electrons are conducted to the external circuit. Consequently, for high efficiency and performance all the three phases must be topologically continuous and connected: connected porosity is essential for continuous fuel flow, connected Ni phase is required for electronic conduction, and connected YSZ enables ionic conduction. As a result, the relative amounts of the three phases in the composite must be such that the volume fraction of each phase is higher than that required for it topological percolation threshold [39]. Note that the topological percolation threshold of a phase in a 3D microstructure depends on its volume fraction *and* numerous other microstructural attributes such as particle/feature shapes/morphologies, size distribution, morphological anisotropy, and spatial arrangements of the features [40]. Accordingly, the performance of porous composite SOFC anodes depends on microstructure.

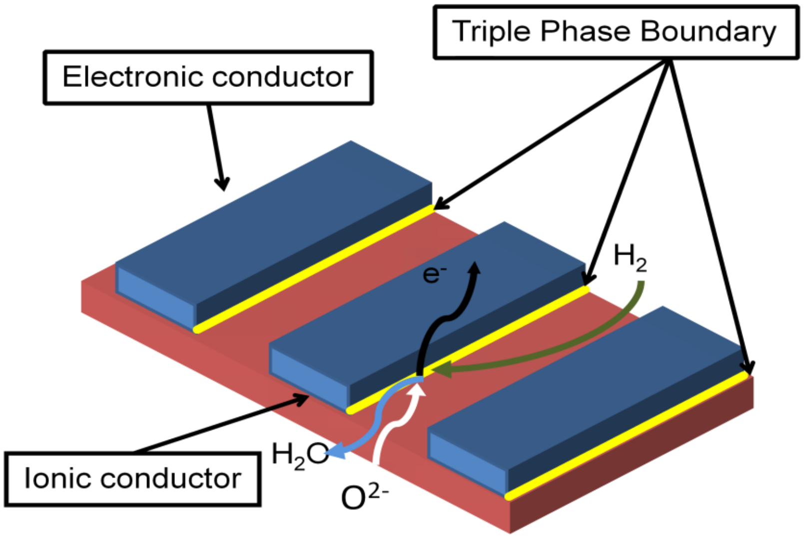

Figure 2 Schematic of TPB in an anode

In the SOFCs having porous Ni metal anode, the oxidation reaction is localized: it can take place only at the two-dimensional (2D) interface of the anode and the electrolyte [41]. On the other hand, in the 3D porous Ni-YSZ composite anodes, the oxidation reaction can occur at all junctions of the Ni, YSZ, and pores. In the 3D microstructure, such junctions are one-dimensional lineal microstructural features where Ni grains, YSZ grains, and pores meet (see Figure 2). These one dimensional microstructural features are called triple phase boundaries, which are the potential sites for the oxidation reaction in the anode. Thus, the potential sites for oxidation reaction are orders of magnitude larger in the porous Ni-YSZ anode as compared to those in the porous Ni metal anode. Therefore, porous Ni-YSZ composite anode facilitates the oxidation reaction and improves the performance of the SOFC. The performance of the porous Ni-YSZ anode depends on the total length of the triple phase boundaries in the anode microstructure: an increase in the total triple phase boundary length is expected to improve the performance.

Clearly, the performance of the porous Ni-YSZ composite anode is *microstructure sensitive* because it depends on the topological connectivity of the Ni, YSZ, and pore phases (for electronic, ionic, and gas phase conduction), and on the total triple phase boundary length in the 3D microstructure (for oxidation reaction). The microstructural triple phase boundary length in turn depends on the relative amounts of Ni, YSZ, and porosity in the composite, the powder processing conditions, and geometric attributes of the initial powder mix such as mean sizes of Ni and YSZ powders, morphology of the powder particles, etc. Therefore, improvement of the performance of SOFC via microstructural engineering is a complex multivariate problem that requires considerable efforts on microstructure modeling and simulations. Major part of this research is devoted to geometric modeling and simulations of three-phase composite microstructures prepared by powder processing.

2.2.3 Cathode

SOFC cathode is an electronic conductor or mixed ionic electronic conductor in the form of a thin porous layer (10-20μm) deposited on the solid electrolyte where the oxygen reduction reaction takes place. A material suitable for SOFC cathode should facilitate the oxygen reduction reaction, should have high electronic conductivity, should have high chemical and structural stability at high temperatures in oxidizing atmospheres, should be chemically compatible with the electrolyte, and should have low coefficient of thermal expansion mismatch with the electrolyte [29]. Lanthanum doped strontium manganite (LSM), $La_{1-x}Sr_xMnO_{2-\delta}$, is the most widely used cathode for the SOFCs based on YSZ electrolyte because of its excellent chemical and thermal compatibility with YSZ

[1, 6, 29]. LSM is a mixed ionic electronic conductor (MIEC), which conducts both electrons and oxygen vacancies. Lanthanum manganite is an intrinsic p-type semiconductor. The electronic conductivity of the pure species is due to the multi-valenced manganese ion and is enhanced via doping with bivalent strontium ion. The oxygen non-stochiometry in LSM responds to oxygen partial pressure and provides some ionic conductivity. Nonetheless, the ionic conductivity of LSM is not high. Consequently, the catalytic activity of LSM is severely limited by its poor ionic conductivity, especially at low operating temperatures. Therefore, in the monolithic porous LSM cathode, the oxygen reduction reaction is highly localized: it occurs only at the 2D interface of the YSZ electrolyte and LSM cathode (see Figure 3(a)). The performance of SOFCs is substantially limited by the *interfacial energy losses* arising from the resistances to charge and mass transfer across interfaces and through the cathode where oxygen reduction takes place [7]. Therefore, it is of interest to study the factors that govern these energy losses so that practical strategies can be developed to minimize such losses in order to improve the performance.

An important strategy to improve the performance of the cathode (and therefore, of the SOFC) is to use porous LSM-YSZ composite cathode [42, 43]. In the 3D porous LSM-YSZ composite cathodes, the reduction reaction can occur at all junctions of the LSM, YSZ, and porosity phases. As mentioned earlier, in the 3D microstructure, such junctions are the triple phase boundaries, i.e., one-dimensional lineal microstructural features where LSM grains, YSZ grains, and pores meet (see Figure 3(b)). The triple phase boundaries are the potential sites for the electrochemical reaction in the composite LSM-YSZ cathode [7, 44, 45]. Thus, the potential sites for the reduction reaction are orders of magnitude larger in the porous LSM-YSZ cathode as compared to those in the monolithic porous LSM cathode. For the fuel cell to function, the porous LSM-YSZ composite cathode microstructural space must provide sufficient continuous connected paths for the flow of oxidant (typically, air or oxygen), for the flow of electrons, and for the flow of ions. Therefore, all three phases of the composite cathode, namely, pores, LSM, and YSZ must have high degree of topological connectivity. Therefore, a 3D composite cathode microstructure having high total triple phase boundary length and high topological connectivity of all three phases is expected to improve the performance of the cathode (and therefore of the SOFC).

Porous LSM/YSZ composite cathodes are typically fabricated using powder processing techniques involving printing and sintering of a powder mix consisting of YSZ and LSM powders. It has been reported that the meso-scale microstructure of the porous composite cathodes is sensitive to the process parameters such as the mean sizes of the initial powders [14, 15, 17] and sintering temperature [17, 18], and the microstructure in turn affects the properties such as the polarization resistance and ohmic resistance that dictate the performance of the cathode. The key microstructural parameters that affect the electrochemical response of porous LSM/YSZ cathodes are the connectivity of the phases and the total length of the LSM-YSZ-pores triple phase boundaries in the three-dimensional (3D) microstructure per unit volume (i.e., the length density). These microstructural parameters depend on the volume fractions of LSM, YSZ, and porosity in the composite, the powder processing conditions, mean size of LSM and YSZ powders, the spreads in the particle size distributions, morphology of the powder particles, etc. Therefore, improvement in the performance of SOFC via microstructural engineering of cathode and anode materials is a complex multivariate problem that requires considerable efforts in the area of microstructure modeling and simulations. There have been numerous contributions in the literature that report different microstructure models and simulations [3, 4, 19-26, 39, 46, 47]. A critical review of these studies is given in the next section. Significant portion of this research is devoted to geometric modeling and simulations of three-phase composite microstructures prepared by powder processing. The results of the present modeling and simulation efforts are reported in chapters 4 and 5.

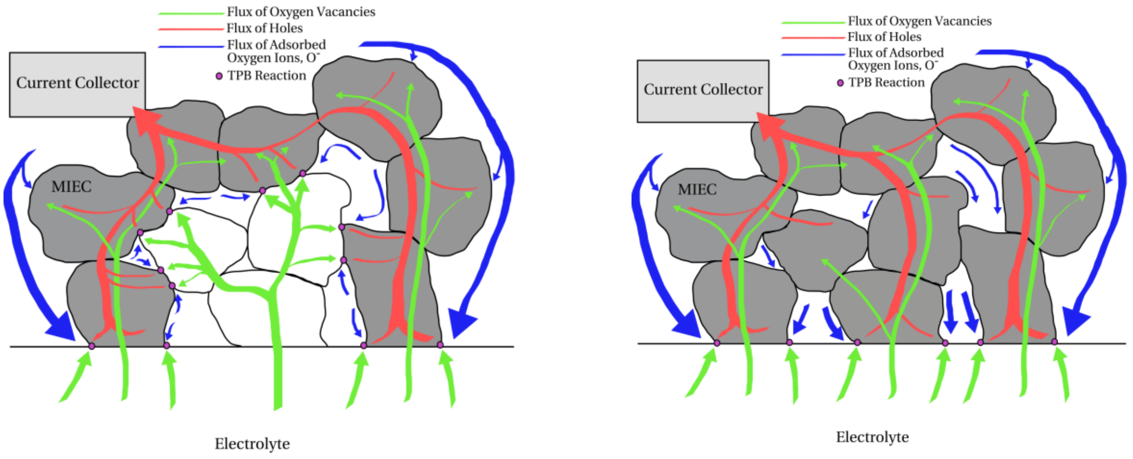

(a) (b)

Figure 3 Schematic of a composite cathode(a) and a monolithic porous MIEC cathode. (Reproduced with the permission of Mr. Matt Lynch).

2.3 Composite electrode modeling

Development of quantitative relationships among process parameters, microstructural geometry, and electrochemical response of porous composite electrode materials is vital to the effective optimization of the performance of SOFCs. As pointed out in the last section, total triple phase boundary length per unit volume of microstructure L_{TPB} is the key microstructural parameter that affects the performance of the porous composite electrodes. In turn, L_{TPB} is, to a large extent, determined by the parameters of the powder processing technique used for porous composite electrode fabrication. Therefore, it is of interest to develop quantitative relationships that express the effects of the process variables such as morphology, mean sizes and size distributions of constituent powders in the initial powder mix prior to sintering on L_{TPB}. There have been numerous theoretical studies on processing-microstructure-performance relationships in the porous composite electrodes of the SOFCs. The relationships between L_{TPB} and the geometric characteristic of the powder mix prior to sintering have been studied using analytical microstructure modeling [4, 19, 39, 46, 47] as well as via geometric computer simulations of the 2D and 3D porous composite electrode microstructures [3, 4, 19-26]. A critical review of important analytical modeling and simulation studies reported in the literature is presented in the following sub-sections.

2.3.1 Analytical Modeling Porous Composite Electrode Microstructures

First analytical microstructure model of porous composite electrode was developed by Sunde [4]. The model assumes that (i) spherical particles of the electronic conductor and ionic conductor are loosely packed in space, (ii) powder particles of each constituent have the same size but different constituents can be of different mono-size, (iii) all triple phase boundaries are of the same length, and (iv) all particles have the same coordination number. Simple geometric reasoning shows that for such idealized microstructural geometry, the total topologically connected triple phase boundary length per unit volume of microstructure is simply equal to the product of the length of each circular triple phase boundary λ, the number of electronic conductor powder particles (LSM) per unit volume N_V, the number of electrolyte (YSZ) particles in contact with each electronic conductor (LSM) particle (i.e., the coordination number) Z, the probability that the electrolyte particle belongs to a connected ion pathway C_{YSZ}, and the probability that the electronic powder particle belongs to an electron conducting chain pathway C_{LSM}:

$$L_{TPB}^{active} = \lambda \cdot N_V \cdot Z \cdot C_{YSZ} \cdot C_{LSM} \tag{2.1}$$

Unfortunately, the length of each circular triple phase boundary λ cannot be computed without further drastic simplifying assumptions concerning the geometry of the particle pairs in contact. Sunde [39] approximates λ by an empirical value of 3 times the radius of electronic conductor powder particle, which is a drastic oversimplication. If the electrolyte particles and electronic conductor particles are spheres of the same radius r, then λ can be calculated from the following geometric relationship given by Chen [46]:

$$\lambda = 2\pi r \sin\frac{\chi}{2} \tag{2.2}$$

In Eqn. (2.2), χ is the dihedral angle between the ionic and electronic conductor particle pair in contact. Chen measured the dihedral angle by measuring the circumferences of the necks formed by the contact between a monolithic porous LSM cathode and a YSZ electrolyte. However, it has been demonstrated that the contact angle between YSZ and LSM changes with polarization [48].

Schneider et al. [19] modified Sunde's equation for the total active triple phase boundary length and arrived at the following analytical equation based on random packing of mono-size spheres of radius r.

$$L_{TPB} = \frac{3d}{r^2}\sqrt{1-\left(\frac{d_0}{d}\right)^{1/3}}\,\varphi_{io}\left(1-\varphi_{io}\right)Z \tag{2.3}$$

$$\phi_{io} = \frac{\theta_Y}{\theta_Y+\theta_L} \tag{2.4}$$

In Eqn. (2.3), L_{TPB} is the length of triple phase boundary per unit volume of the composite electrode; d_o and d are the initial and final relative densities of the composite electrode, respectively. θ_Y and θ_L are the volume fractions of the ionic conductor (e.g., YSZ) and the electronic conductor (e.g., LSM), respectively. ϕ_{io} is the relative volume fraction of the ionic conductor. Z is the coordination number of the particles. Unfortunately, Eqn. (2.3) leads to a physically unacceptable limit as d approaches 1 (i.e., fully dense material). In the limit of $d \rightarrow 1$ (i.e., porosity volume fraction approaching zero) the L_{TPB} must approach zero because YSZ-LSM-porosity triple phase boundaries cannot exist when there are no pores. However, Eqn. (2.3) predicts a non-zero value of L_{TPB} as $d \rightarrow 1$, which is physically untenable. Further, to compute the total triple phase boundary length per unit volume using either Sunde's approach or Eqn. (2.3) it is necessary to *assume* a value for the mean coordination number Z.

The above review of the analytical models for total triple phase boundary length reported in the literature leads to the following conclusions.

(i) The models assume that electrolyte and electronic conductor powder particles in the powder mix are spherical and mono-sized. Consequently, the existing models do not capture the effects of powder particle shapes/morphologies and particle size distributions on the total triple phase boundary length.

(ii) All analytical models assume that all triple phase boundaries are of the same length and

there is no distribution of coordination numbers present in the microstructure. These assumptions are unrealistic.

(iii) To compute total triple phase boundary length using the existing analytical models, it is essential to know the mean coordination number for the particle populations, which cannot be measured experimentally, except via reconstruction of the 3D microstructure [49], and is difficult to compute from theoretical considerations without making numerous simplifying assumptions. Further, a distribution of coordination numbers usually exists in the real microstructures having a distribution of particle sizes, and there is often a strong correlation between the particle size and the coordination number: larger particles have higher coordination numbers [49].

The above analysis reveals that there is a need to develop more realistic geometric models for the total triple phase boundary length that are applicable to powder particles of different shapes/morphologies and can be applied to poly-size powders so that the effects of the powder particle morphologies and size distribution characteristics on the total triple phase boundary length can be studied. In the next chapter, such analytical model has been developed and utilized for detailed parametric studies on the effects of volume fractions, mean particles sizes, and numerous other geometric attributes of the electrolyte and electronic conductor powders in the initial powder mix on the total tripe phase boundary length in the powder processed porous composite electrode microstructures.

2.3.2 Computer Simulations of Porous Composite Electrode Microstructures

Numerous studies have been reported in the literature that simulate the effects of powder process parameters on the 2D and 3D microstructures of porous composite electrodes [3, 4, 19-26]. All geometric microstructure simulations must allow overlaps among the electrolyte (YSZ) and electronic conductor (LSM) particles to create the triple phase boundaries (TPBs) because simulations based on non-overlapping particles (so called hard-core simulations) contain only point contacts among the particles. Consequently, the simulated total triple phase boundary length depends on the extent of the overlaps permitted.

The earliest simulations of composite electrode microstructure were based on placement of mono-size spherical electrolyte and electronic particles on the lattice points of a periodic lattice with the probabilities proportional to the volume fractions of the two constituents. Sunde [24] and Ali [21] performed such 2D two-phase simulations without incorporating porosity using a Monte-Carlo based algorithm. These studies assume that each simulated interface between electrolyte and electronic conducting particle pair creates a triple phase boundary, which is unrealistic. Ali [19] concluded that the total tripe phase boundary length is optimized at the 50% volume fractions of electrolyte and electronic conductor phases. This conclusion is reasonable. Nonetheless, these simplistic simulations do not capture the effects of porosity volume fraction; mean particle sizes;

particle shape and size distributions; and 3D geometric effects on the total triple phase boundary length.

Ji [20] has reported Monte Carlo based simulations of composite cathode microstructures where individual powder particles are placed at lattice points of FCC lattice. Each lattice point was randomly assigned as the ionic conductor, electronic conductor or porosity and the simulations were implemented in 3D. Therefore, these simulations capture the effects of 3D geometry and porosity on the triple phase boundary length. Nonetheless, these simulations are based on mono-size particles of unrealistic *parallelepiped* shape. Therefore, they do not reveal the effects of mean particle size, size distribution, and morphology of the particles on the simulated total triple phase boundary length.

Fabrication of a composite electrode is geometrically similar to random packing of particles rather than periodic lattice based simulation. Therefore, compared to the simplistic lattice based simulations, random sphere packing simulations of composite electrode microstructures have better fidelity to the real microstructures and they reveal effects of numerous powder particle characteristics on the total triple phase boundary length. Schneider [19] developed a random packing model for composite electrode microstructure. The simulation employs discrete element method (DEM) in which spherical particles of each component are randomly packed in a given volume with density d_0 and then numerically sintered by pulling the particle centers together by a specified amount so that: (a) the density is increased to d, and (b) overlaps are created between particles, which lead to formation of simulated triple phase boundaries. As a result, the simulated triple phase boundary length per unit volume depends on the extent of the overlaps permitted, which is in turn governed by the ratio of initial density d_0 and the final density d. This is possible only when the two constituent powders in the powder mix have the same sintering characteristics. In reality, the sintering characteristic of the two components can be markedly different. For example, in a Ni-YSZ anode, Ni is easier to sinter than YSZ. Another limitation of this model is that the particle sizes of the electrolyte and electronic conductor particles are assumed to be equal, which makes it impossible to quantify the effects of particle size ratio on the total triple phase boundary length. This key assumption made by Schneider [19] is removed by Ali [3] in his simulations of composite electrode microstructure. In Ali's study, porous composite electrodes are modeled by randomly packing spherical particles of the constituents followed by enlargement of the particle radii to achieve overlaps between the particles. Ali performed a detailed parametric study of the effects of electrode thickness, particle size ratio, and volume fractions of the constituents on the total length of topologically connected triple phase boundaries. Ali showed that the total triple phase boundary length is inversely proportional to the square of the mean particle size when both the powder constituents are of the same mono-size as predicted earlier by Costamagna [23]. The limitation of Ali's model is that it does not take into consideration the effects of particle size distribution and particle morphology on the total triple phase boundary length.

Recently, Kenney [26] has developed a random spherical particle packing model in which the sizes of the spherical particles of the two constituents have *normal* distributions having different mean sizes. The overlaps between the particles are created via a simulated sintering process in which the minimum allowable distance between particle centers is adjusted until the desired porosity volume fraction is reached.

Kenney's simulations reveal that a coefficient of variation (CV) of 0.4 lowers the triple phase boundary length by 35% compared to mono-dispersed particles (CV=0). Interestingly, Kenney's simulations also reveal that the total triple phase boundary length need not be maximum in a composite having equal volume fractions of electrolyte and electronic conductor phases if the powder particles have a size distribution. It is important to point out that in the random sequential adsorption (RSA) based simulations (such as those of Kenney) the simulated microstructure does depend on the order in which the particles are placed in the simulation when particles are of different sizes [50]. Therefore, it is likely that some of Kenney's conclusions are affected by this bias. Kenney's simulations are based on spherical particles, and therefore, do not capture the effects of particle morphologies on the total triple phase boundary length. Further, these simulations are based on normal distribution of particles sizes, and therefore, do not reveal the effects of skewness of the size distribution on the total triple phase boundary length.

Recent developments in simulation based modeling approaches indicate an increasing awareness and attention on the microstructure sensitivity of the composite electrodes of SOFCs. As more and more process parameters get included in the simulations, the simulated microstructures are expected to have better fidelity to the corresponding real microstructure. Nonetheless, such realistic microstructure simulations involving large degrees of freedom are also computationally more intensive, complex, and expensive. On the other hand, the analytical models are free from the computational cost of 3D simulations. Nonetheless, as concluded in the previous section, the analytical models reported in the literature do not capture the effects of the parameters such as particle morphologies, size distributions, and mean particle size ratio on the total triple phase boundary length in the composite electrode microstructures. Therefore, there is a need to develop more realistic analytical microstructure models for prediction of total triple phase boundary length in the 3D microstructures of porous composite electrodes that capture the effects of powder particle shapes/morphologies, mean particle sizes, size distributions, volume fractions, etc on the total triple phase boundary length. In the next chapter, a new analytical model for composite electrodes is presented that is capable of *explicitly* predicting the effects composition, porosity, particle size distribution and particle morphology on the total triple phase boundary length in 3D porous composite electrodes.

2.4 Microstructure Characterization of Composite Electrodes

Experimental studies on porous composite electrode microstructures require suitable practical microscopy techniques for observation and characterization of the microstructural features present in the 2D metallographic sections and 3D microstructural volumes. To observe and characterize the triple phase boundaries, it is essential to *simultaneously* observe the electrolyte, electronic conductor, and porosity phases present in the porous composite electrode microstructures because, by definition, the triple phase boundaries are the microstructural junctions of these three phases. This is a major challenge in the characterization of porous composite electrode microstructures, particularly in the characterization of the microstructures of porous composite cathodes. The microstructure characterization generally involves the following three steps.

1. Materialography: preparing the specimen for microscopy.

2. Imaging: acquisition of images (2D or 3D) of the microstructure windows

3. Quantitative characterization of the acquired microstructural mages

While there are well-established general stereological techniques for the quantification of microstructural images, which are reviewed in the following section, the specimen preparation and microscopy techniques are specific to the material chemistry and the microstructural length scales of interest. Substantial of efforts have been made on the microstructure characterization of YSZ-LSM porous composite cathodes. Due to the sub-micron microstructural length scales of interest in these composite cathode microstructures, optical microscopy is not useful. The conventional SEM techniques are also not useful because they do not provide sufficient contrast between YSZ and LSM phases due to their comparable average atomic numbers [28, 51]. Consequently, the triple phase boundaries in porous composite cathode microstructures cannot be unambiguously identified and characterized using conventional optical or SEM based microscopy. Although a high-resolution electron backscatter technique has been reported to yield sufficient contrast between YSZ and LSM phases in coarse microstructures produced via sintering at temperatures above 1200^{o}C [52], such coarse grained microstructures are not useful for SOFC applications. A combination of focused ion beam (FIB), Auger electron spectroscopy (AES) elemental mapping, and secondary electron imaging has been successfully used for imaging the YSZ and LSM phases [28], but the technique has not been used for the characterization of the triple phase boundaries. Further, the use of FIB for preparation of microstructural sections is time consuming and only a small 2D microstructural section area section (~ 50 μm^2) can be prepared, which may not be a statistically representative microstructural segment for any meaningful quantitative characterization. Recently, Wilson [53, 54] has developed a FIB-SEM technique to reconstruct the 3D microstructure of YSZ-LSM cathode. The technique utilizes an energy-selective backscatter electron (ESB) imaging to acquire images in which the all three phases (YSZ, LSM and porosity) can be observed simultaneously. In this study, the total length of the triple phase boundaries, among other microstructure attributes, was measured in the reconstructed 3D microstructure. Unfortunately, such specialized equipment is not available in most research laboratories and the use of FIB limits the area or volume of the microstructure that can be observed and characterized. Further, removal of material by focused ion beam for generation of successive microstructural serial sections for 3D microstructure reconstruction is very time consuming. Therefore, there is a need to further develop efficient practical specimen preparation and microscopy techniques that enable unambiguous observations of all three microstructural constituents of porous composite cathodes, namely, electrolyte (such as YSZ), LSM, and pores, *simultaneously* in the microstructure using equipment that are readily available, and permit unbiased quantitative estimation of 3D microstructural parameters such as total length of triple phase boundaries per unit volume. In this research, such technique has been developed using atomic force microscopy (AFM). The details are reported in chapter 3.

Compared to the YSZ-LSM cathode, there has been substantial success in the characterization of Ni-YSZ porous composite anodes. Wilson [55] has reported a 3D reconstruction of Ni-YSZ composite anode microstructure, in which all three phases (Ni, YSZ and gas pores) are identified and color-coded, using a FIB-SEM technique. Again, since the FIB is used to polish the specimen, the reconstructed volume is rather limited.

Thydén [56] presented a method to acquire microstructural images of Ni-YSZ composite anode using backscatter electron imaging (BSE) in SEM. The method exploits the differences in the secondary and backscatter electron yields between Ni and YSZ under low acceleration voltages (1~2 kV). Thydén [56] did not report quantitative characterization of triple phase boundaries using the acquired images, though. Therefore, it is of interest to combine the low voltage BSE imaging technique and stereological analysis so that reliable measurements of microstructure attributes of Ni-YSZ can be made available for processing-microstructure-performance studies on porous composite SOFC anodes.

2.5 Stereological Techniques for Quantitative Microstructure Characterization

Any microstructure can be regarded as a stochastic arrangement of points, lines, surfaces and interfaces, and volumes of different constituents in three-dimensional space. Therefore, a microstructure can be quantified by estimating relevant geometric parameters of these four basic features. In porous three-phase composite microstructures of the SOFC electrodes, the first order microstructural parameters of interest are relative amounts of the three phases represented by their volume fractions, total surface areas of interfaces between the phases per unit volume of microstructure, and total length of the lineal triple phase boundaries per unit volume. In addition, two-point correlation functions of these three-phase microstructures have been utilized for statistical representation of microstructures. Although all of these measures are three-dimensional microstructural attributes, they can be estimated in an efficient, unbiased and assumption-free manner from the design based measurements performed on representative two-dimensional metallographic sections using general stereological techniques [57-59]: it is *not* necessary to generate 3D microstructures using tomography or serial sectioning techniques, which requires considerable efforts and/or specialized equipment. The relevant stereological techniques are reviewed below.

2.5.1 Volume Fraction Measurement Techniques

Volume fraction of a phase or a constituent is a quantitative measure of its relative amount in the 3D microstructure. In the SOFC electrode 3D microstructures, it is of interest to estimate the volume fractions of electrolyte, electronic conductor, and porosity phases. Volume fraction is denoted by the symbol, V_V, where the subscript V signifies the normalization by the specimen volume. Volume fraction of a phase in any *arbitrary* 3D microstructure can be estimated from the measurements performed in the 2D metallographic sections without involving any assumptions concerning the shapes, sizes, orientations, or spatial randomness of the features of interest. Interestingly, as volume fraction is a dimensionless microstructural parameter, it is not necessary to know the microscope (or micrograph) magnification for its estimation. Volume fraction can be estimated from the measurements performed in the metallographic planes either by using the areal analysis method, or by using the point counting method. These techniques are described in the following sub-sections.

2.5.1.1 Areal Analysis

The areal analysis involves the measurement of the fraction of the area of representative metallographic planes A_A occupied by the phase of interest. The *population average* value (or more precisely, "expected value") $<A_A>$ of the area fraction A_A is equal to the volume fraction θ of that phase in the 3D microstructure [57-59]:

$$\theta = \langle A_A \rangle \tag{2.5}$$

The area fraction of the phase of interest A_A can be measured in the microstructural fields observed in a microscope, or from micrographs. Obviously, there are statistical variations in the local area fraction A_A measured in different microstructural fields. Therefore, it is essential to perform the measurements on numerous microstructural fields to obtain a representative average value of the area fraction. Areal analysis is a convenient method for estimation of volume fraction using digital image analysis. Once a gray scale microstructural image is converted into its color-coded image, the local area fraction of the phase of interest is simply equal to the number of pixels in the phase of interest divided by the total number of pixels in the measurement frame. Modern image analyzers can be interfaced with automatic specimen movement stage and auto-focus modules of the microscope to automatically scan large number (~100 or more) of microstructural fields at certain fixed distance intervals and perform area fraction measurements in such microstructural fields automatically to yield a precise average value of the volume fraction. Nonetheless, in some microstructures, it is difficult to obtain a representative color-coded image from gray scale microstructural image (see Figure 4). In such cases, digital image analysis is not useful, and one must resort to manual measurements. Areal analysis is not an efficient technique for estimation of volume fraction if manual measurements are required. In such cases, volume fraction can be efficiently estimated by using the point counting method discussed below.

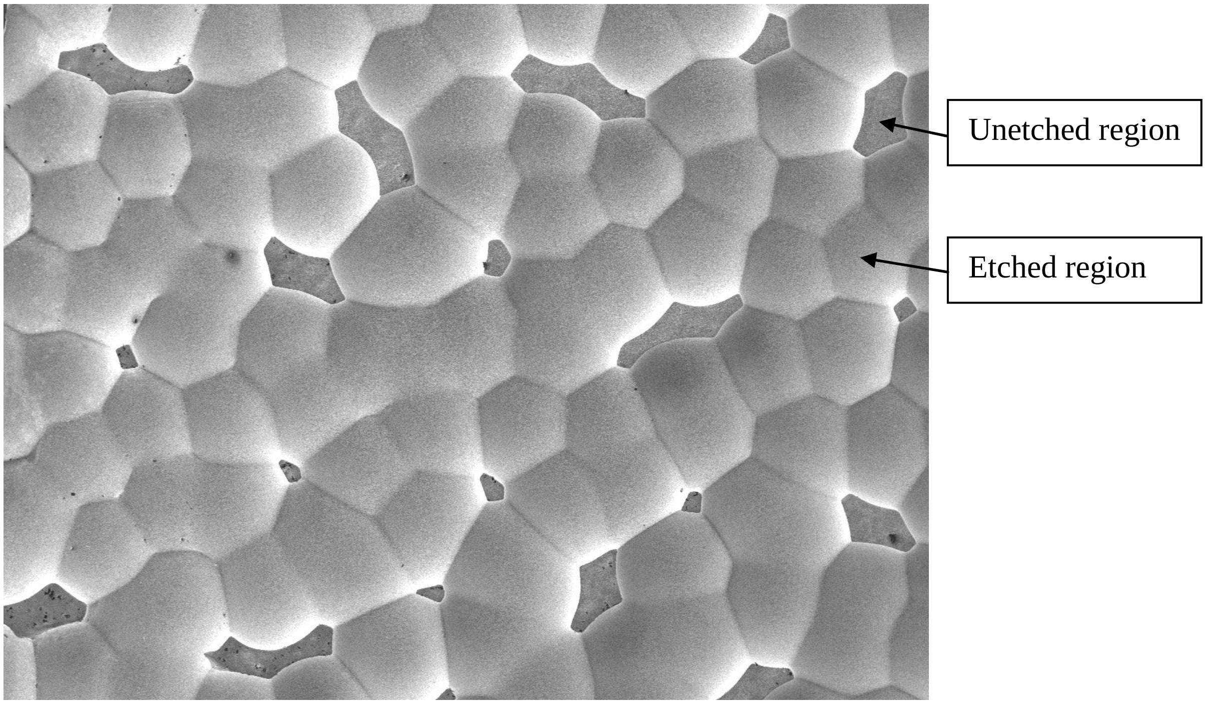

Figure 4 Optical microscope image of the surface of a laser-etched titanium alloy. It is difficult to color-code this grayscale image into a binary image of etched and unetched regions.

2.5.1.2 Point Counting

In this method, a set of test points is overlaid on a microstructural field, and the number of test points contained in the phase of interest is counted. The fraction of test points in the phase of interest P_P is calculated by dividing the number of test points in phase of interest by the total number of test points. The *population average* value of this point fraction $\langle P_P \rangle$ is precisely equal to the volume fraction of the phase of interest [57-59].

$$\theta = \langle P_P \rangle \tag{2.6}$$

Point counting can be performed by using a grid of regular array of test points, or by using randomly distributed test points. The procedure is called "systematic" point counting when a regular array of points is used, and it is called "random" point counting when random test points are used. The systematic point counting is easier to perform in practice, and it is more efficient than the random point counting.

2.5.2 Interface Area Measurement Techniques

In the SOFC electrode 3D microstructures, it is of interest to estimate the total surface area per unit volume of the electrolyte-porosity interfaces, of the electronic conductor-porosity interfaces, and of the electrolyte-electronic conductor interfaces. The total area of the internal microstructural surfaces of interest per unit volume of a given type of interfaces is the ratio of the sum of the areas of all that type interfaces in a specimen divided by the specimen volume, and it is denoted by the symbol S_V. This microstructural parameter can be used to characterize how finely (or coarsely) a microstructural phase/constituent is dispersed in the 3D microstructural volume. The dimensions of S_V are mm^2 / mm^3 or $(mm)^{-1}$. Since S_V is not a dimensionless parameter, it is essential to know the magnification of microscope (or micrographs) for its estimation.

Estimation of S_V involves unbiased sampling of the 3D microstructure using test lines. The number of intersections between the test lines and the surfaces of interest is counted. The *population average* value of the number of intersections between the test lines and the surfaces of interest per unit test line length, $\langle I_L \rangle$, is related to the total surface area per unit volume, S_V, through the following stereological equation [57-59].

$$S_V = 2\langle I_L \rangle \tag{2.7}$$

Eqn. (2.7) is general: it is applicable to microstructural surfaces of any arbitrary geometry. I_L has units of $(\mu m)^{-1}$, because it is the number of intersections per unit test line length. In practice, the test lines are placed in a metallographic plane to perform the intersection counting.

An alternate general and unbiased stereological relationship is available for estimation of S_V, which is particularly attractive when the measurements are performed using automatic digital image analysis. This method requires measurements of the total length of all the boundary traces observed per unit area of metallographic plane, L_A. It can be shown that [57-59],

$$S_V = \frac{4}{\pi}\langle L_A \rangle \tag{2.8}$$

In Eqn.(2.8), $<L_A>$ is the *population average* value of the total boundary length per unit area. It is easier to program an image analyzer to measure the lengths of all the boundaries of interest in the measurement frame as compared to counting the number of intersections of test lines with the boundaries of interest. Therefore, if automatic image analysis is to be used, Eqn.(2.8) can be used for estimation of S_V.

2.5.3 Total Length of Triple Phase Boundaries per Unit Volume

In the 3D microstructures of SOFC electrodes, the triple phase boundaries of interest are the triple lineal junctions of electrolyte, electronic conductor, and porosity phases. Let L_{TPB} be the total length of the triple phase boundaries per unit volume of microstructure. The units of L_{TPB} are $\mu m/\mu m^3$ or $(\mu m)^{-2}$. Since L_{TPB} is not dimensionless, it is necessary to know the microscope magnification for its estimation. In a 2D metallographic section, the triple phase boundaries that intersect the metallographic pane appear as *triple point* junctions of the three phases. Let P_A be the number of such triple point junctions observed per unit area of the metallographic plane. In general, P_A varies from one microstructural field to another a random statistical manner. Let $\langle P_A \rangle$ be the population average value of P_A obtained by averaging it over all possible microstructural fields in the specimen. It can be shown that [57-59],

$$L_{TPB} = 2\langle P_A \rangle \tag{2.9}$$

Therefore, L_{TPB} can be experimentally estimated in an unbiased and assumption-free manner in any 3D microstructure by using the above stereological relationship via measurements of P_A. 3D microstructure has been used for direct experimental estimation of L_{TPB} in the SOFC porous composite electrode microstructures. Inspection of Eqn. (2.9) reveals that an unbiased determination of total triple phase boundary length L_{TPB} does *not* require a 3D microstructure reconstruction, which involves significantly more metallographic efforts than acquisition images in the 2D metallographic sections.

2.5.4 Two-point Correlation Functions

The first order microstructural parameters such volume fractions do not provide any information concerning spatial arrangements, anisotropy, and morphologies of the microstructural features. Microstructural correlation functions implicitly contain information about such second order microstructural attributes. The correlation functions have been used in small angle radiation scattering theories [60]. The correlation functions have also been used in the statistical mechanics based models for computation of mechanical and physical properties of heterogeneous materials [61]. In a 3D microstructure containing m phases or constituents, a two-point correlation function $P_{ij}(r, \theta, \Phi)$ is the probability that a randomly located straight line of length r and angular orientation (θ, Φ) has its one end point in the phase i^{th} (where, $i = 1,2,\ldots\ldots, m$) phase or constituent *and* the other end point is in the jth (where, j = 1,2,……, m) phase or constituent (see Figure 5). For example, $P_{22}(r, \theta, \Phi)$ is the probability the both the end point of randomly located line of length r and orientation (θ, Φ) are in phase-2. The events associated with the two-point correlation functions only pertain to the *end points* of the line; the microstructure through the line itself is not relevant to these events. Although there are m^2 two-point correlation functions in a microstructure containing m phases/constituents, there are only [m(m-1)/2] independent two-point correlation functions due to the following general mathematical relationships [62]:

$$P_{ij} = P_{ji} \tag{2.10}$$

$$\sum_j P_{ij} = \theta_i \tag{2.11}$$

$$\lim_{r \to 0} P_{ij}(r) = \theta_i{}^2 \delta_{ij}, \delta_{ij} = \begin{cases} 1, i = j \\ 0, i \neq j \end{cases} \tag{2.12}$$

$$\lim_{r \to \infty} P_{ij}(r) = \theta_i \theta_j \tag{2.13}$$

$$\lim_{r \to 0} \frac{P_{ij}(r)}{r} = \frac{S_V^{ij}}{2}, i \neq j \tag{2.14}$$

θ_i denotes the volume fraction of phase i; S_V^{ij} is the interface area per unit volume between phase i and phase j. For a binary microstructure only one function is independent; for a three-phase microstructure such as a composite cathode, there are three independent two-point functions.

Inspection of Eqn. (2.14) reveals that the slope of function near origin is proportional to the interface area (short-range information) and Eqn. (2.13) shows that the function approximates the product of volume fractions when the distance(r) between points is large enough. Before the two-point function reaches this limit, the shape of the functions is essentially determined by the long-range structure, and the shortest distance(r) at which the functions reaches saturation ($\theta_i\theta_j$) is called the correlation distance, which is sometime used as a characteristic microstructure parameter.

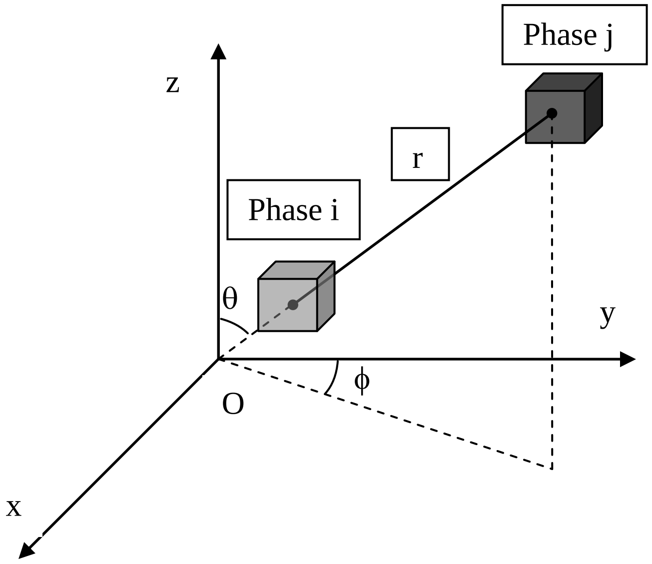

Figure 5 Schematic illustrating the definition of a two-point coorelation function of phase i and j, or $P_{ij}(r,\theta,\phi)$.

CHAPTER 3

CHARACTERIZATION OF SOFC COMPOSITE ELECTRODES

An important objective of this research is to quantitatively characterize the triple phase boundaries (TPBs) in the microstructures of porous composite anode and cathode materials for SOFCs using suitable microscopy, digital image processing, and stereological techniques. In this Chapter, a new atomic force microscopy (AFM) and digital image processing based technique is developed for simultaneous observations of YSZ, LSM, and porosity phases, and triple phase boundaries in the two-dimensional (2D) materialographic sections of porous YSZ-LSM cathode microstructure, which has been a major problem in the characterization of the triple phase boundaries in this composite cathode material. The total triple phase boundary length per unit volume L_{TPB} is then estimated from automated stereological measurements performed on the color-coded images of the 2D sections of the porous cathode microstructure. In addition, the triple phase boundaries are quantitatively characterized in the microstructures of porous Ni-YSZ composite anode material and two proton conductor LSCF-BZCY composite cathode materials using backscatter electron SEM imaging, digital image analysis, and stereology. These experimental quantitative microstructural data have been utilized to validate the stochastic geometry based model for L_{TPB} reported in the next Chapter. The next section describes microstructure characterization of porous YSZ-LSM composite cathode material and that is follows by characterization of microstructure of porous Ni-YSZ composite anode and porous LSCF-BZCY composite cathode.

3.1 Quantitative Characterization of YSZ-LSM Composite Cathodes Microstructure

The YSZ-LSM composite cathode is the most widely used composite cathode in SOFCs. Nonetheless, characterization of triple phase boundaries in these materials has been problematic. For unambiguous observations of the triple phase boundaries, it is essential to simultaneously observe of YSZ, LSM, and porosity phases in the microstructure. Due to the sub-micron microstructural length scales of interest in these composite cathode microstructures, optical microscopy is not useful. On the other hand, the conventional SEM techniques are not useful because they do not provide sufficient contrast between YSZ and LSM phases due to their comparable average atomic numbers [28, 51]. In this section, a new technique based on a combination of AFM and digital image processing is presented for observation and quantitative characterization of the triple phase boundaries in porous YSZ-LSM composite cathodes. The material processing is described in the next sub-section, and that is followed by materialography and microstructure characterization.

3.1.1 Material Processing

The porous YSZ-LSM composite specimens were prepared by Mr. M. Lynch of Professor M. Liu's research group at Georgia Tech. Powders of YSZ (approx. 40% volume) and LSM (approx. 60% volume) were mixed and ground together using mortar and pestle for 30 minutes in ethanol to obtain a homogenous slurry that was subsequently dried at 75^o C. The mean powder sizes of the mixed and ground LSM and YSZ powders were 1.04 μm and 0.37 μm, respectively. The powder mix was hand-pressed to form pellets of 1 cm diameter and 1.5 mm height. These pellets were sintered at 1100^{o} C for 3 hours to obtain a spatially uniform isotropic material containing three-phases, namely, YSZ, LSM, and porosity, and having the relative phase fractions and microstructural length scales in the same ranges as those in the porous composite cathodes of interest in the SOFC applications.

3.1.2 Specimen Preparation and Materialography

The disc shaped porous composite cathode specimen was sectioned along a plane perpendicular to the faces of the disc for microstructural observations. The sectioned porous specimen was infiltrated with methylmethacrylate (MMA) in a vacuum chamber (Struers Epovac) at 150 mbar pressure for 2 min. The MMA infiltration was then polymerized under ultraviolet light at room temperature for 5 hr. This leads to vacuum impregnation of the pores with MMA, which eliminates "pull-outs" of grains during subsequent polishing. The vacuum impregnated specimen was mounted in a cold-mounting epoxy for grinding and polishing. The mounted specimen was ground and polished using 240 and 800 grit SiC papers followed by fine polishing using diamond suspensions of different diamond sizes (9 μm, 6 μm, 3 μm and 1 μm). The final polishing was done using a colloidal silica suspension (0.05 μm size). The grinding and polishing steps were performed on Allied TechPrep polishing equipment. The polished sample was etched in a 3M hydrochloric acid solution for 45 seconds at room temperature. As LSM and YSZ phases have different chemical reaction rates with hydrochloric acid, this etching procedure creates a small but consistent "relief" between the two phases, which can be detected by atomic force microscope and can be used to distinguish these phases in the microstructure.

3.1.3 Atomic Force Microscopy

Atomic Force Microscope (AFM) is a high-resolution scanning-probe equipment that scans nano-scale topography of the specimen surface using a miniature cantilever. The AFM records the extent of deflection of the cantilever as the tip traverses the specimen surface, and thereby, generates a topographic map of the surface. The Z (depth) resolution of AFM is typically 1 nm, and therefore, a differential topographic "relief" between microstructural phases (YSZ and LSM in the present case) on the order of nanometers generated by chemical etching can be precisely detected by AFM. The resulting topographic map can be used to visualize the chemically etched microstructure of porous composite cathode containing YSZ, LSM, and porosity phases. Costa [63] has used a similar AFM based imaging technique to acquired multi-phase microstructure images of Nb-Al-Ni eutectic alloy.

In the present study, a Veeco Dimensions 3100 AFM equipped with VL 300-A Phosphorous (n) doped Si cantilever having front angle of 15 degrees and tip height of 15 μm was used. The images were recorded in tapping mode with a sampling frequency of 1Hz and X-Y resolution of 20 nm and Z resolution of 1 nm. At this resolution, each AFM image (topographic map) of a microstructural area of 100 μm^2 containing about 400 YSZ and LSM grains and about 500 triple phase boundaries could be recorded in about 8 minutes. The grain sizes of YSZ and LSM grains are on the order of 400 nm, and therefore, the X-Y resolution of 20 nm and Z resolution of 1 nm are quite sufficient to clearly observe the microstructure.

3.1.4 Digital Image Processing

The recorded AFM image is first processed using a commercial AFM imaging processing and analysis software, and these images are subsequently processed using an in-house computer code (see Appendix A.1) developed in this dissertation research to reveal the microstructure. The flow chart of the image processing procedure is given in Figure 7. The image processing steps are described as follows.

Step 1: The AFM images were first rendered with Gwyddion, an open-source AFM image processing system. During this step the line artifacts are removed and the images are leveled. The topographic data were transformed to grey-scale images with 256 levels. Nonlinear rendering was employed so that maximum visual contrast can be obtained with only 256 levels.

Step 2: The grey-scale images are converted to color-coded images in which each phase is represented by a specified color. The color-coding is implemented by using a image segmentation technique called thresholding, in which two threshold grayscale values were specified for each phase (YSZ, LSM and pores).

Step 3: The color-coded images contain a special artifact which causes a false “shell” of LSM around the YSZ phase. Ideally boundary between YSZ and pores is a square step but in reality the boundary always has a slope, which is caused by the mechanical polishing and/or the shape of the tip of the cantilever. During thresholding, the boundaries are color-coded into three phases: the lowest part as pores, the highest as YSZ and the middle part as LSM, which is the artificial “shell” as illustrated in Figure 6. Although the artificial “shell” is usually as thin as 1-2 pixels, its presence can bias the stereological measurements. A specialized in-house computer code has been developed to correct this artifact while preserving the details of the phase morphology. The code detects the boundary between YSZ and pores and reassigns the “shell” as YSZ or pore.

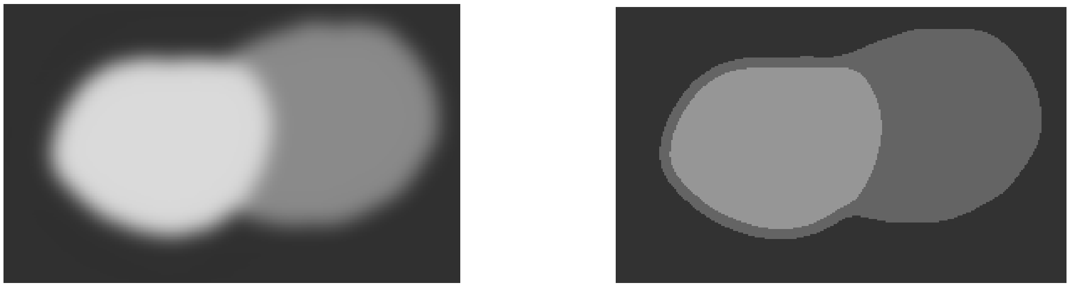

(a) (b)

Figure 6 An illustration of the "shell" thresholding artifacts : (a) original image; (b) color-coded image after thresholding

Step 4: The last image processing step is scrapping of features smaller than 0.012 μm^2 to remove noise in the grey-scale image (see Appendix A.2).

Figure 10(a) is a resulting grey-scale AFM image showing the three phases YSZ, LSM, and porosities revealed in this manner. In this image, the bright phase is YSZ, the darkest phase is the porosity, and the gray phase is LSM. Thus, atomic force microscopy enables clear distinction among the three phases. Figure 10(b) shows segmented color coded image of the microstructural field in Figure 10(a); quantitative stereological measurements were performed on such segmented images in an automated manner using image processing.

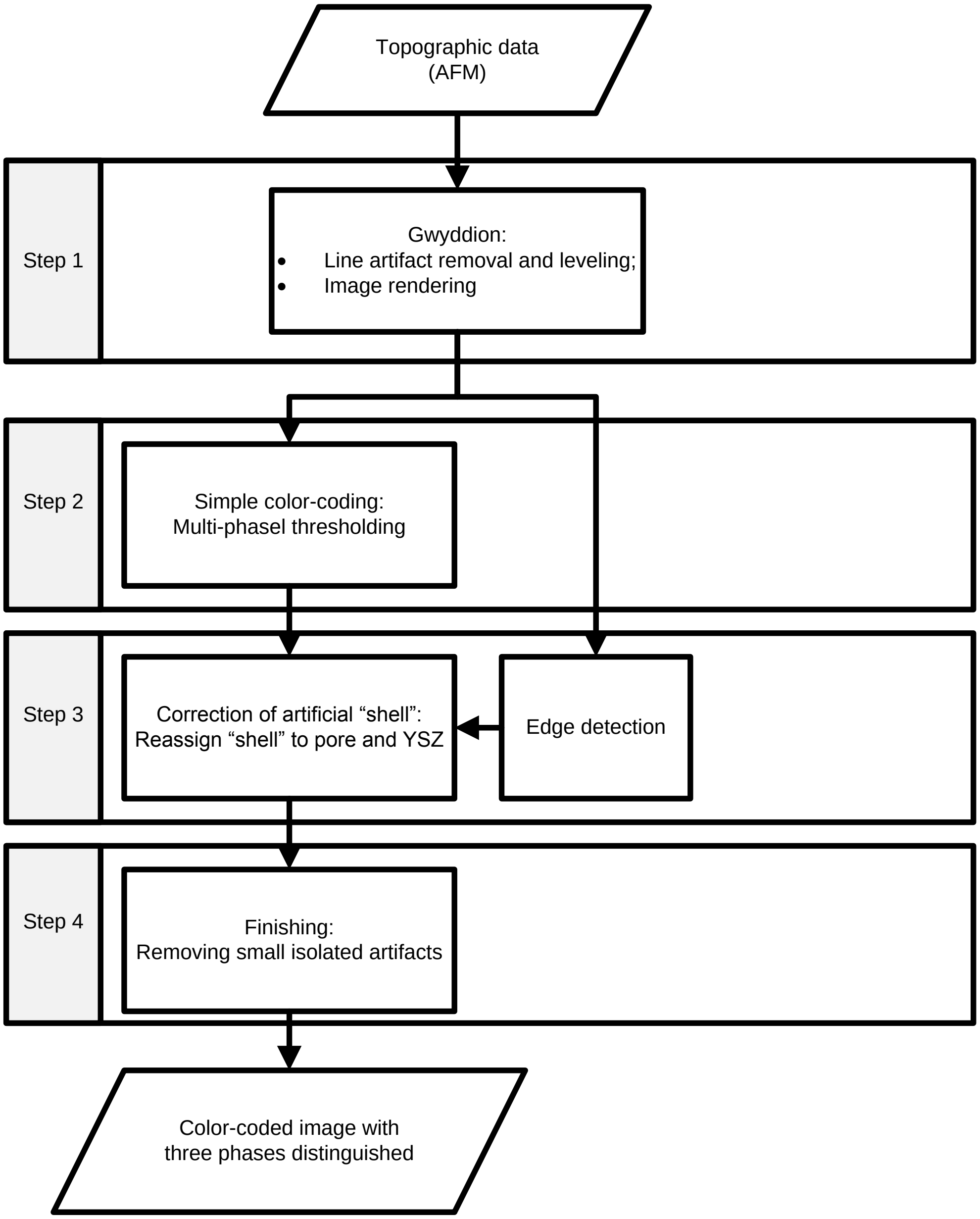

Figure 7 Flowchart of the AFM image processing

3.1.5 Validation of the AFM-Based Imaging Technique

It is necessary to validate the AFM based microstructural observation technique reported in the previous sub-section. For this purpose, four micro-hardness indents were placed in one region of a polished and etched specimen as markers and gray scale AFM and SEM (Joel 1530, InLens mode) images of exactly the same region were recorded, which are depicted in Figure 8. Observe that the porosity distribution in both the micrographs appears to be identical; the only difference between the two micrographs is that the YSZ and LSM phases cannot be distinguished in the SEM image. The two-point correlation function of each image was also produced using a in-house computer code (see Appendix A.8). The two-point correlation function captures both long-range and short-range microstructure geometric characteristics and thus comparison of the two-pint correlation functions of two microstructure images is a reliable way of validating the statistical similarity of two images (see section 2.5.4). In this study, the two-point correlation functions of the AFM and SEM images matches well both at the short-range and long-range (Figure 8), which quantitatively validates the AFM imaging technique.

To further confirm AFM based microstructural observations, energy dispersive spectra (EDS) were used to identify the phases in the polished sample surfaces based on their elemental compositions (see Figure 9). For YSZ-LSM composite, yttrium and lanthanum were selected as the indicative elements of YSZ and LSM, respectively. Regions of interest were chosen based on their local topographic height differentials with respect to the neighboring phases created by chemical etching. In Figure 9(a) the EDS signal was collected from a low topographic region with respect to its surrounding features. The EDS spectrum shows lack of zirconium and a more pronounced lanthanum peak and confirms the presence of LSM phase at that spot. In Figure 9(b), the EDS signal was collected from a raised region near a step. Such topography indicates that this region is YSZ. The strong zirconium peak in the EDS spectrum confirms the presence of the YSZ phase at that location. Therefore, these EDS observations validate the topography based distinction between YSZ and LSM phases generated by AFM for simultaneous observations of YSZ and LSM phases (and porosity) in the composite porous cathode microstructures.

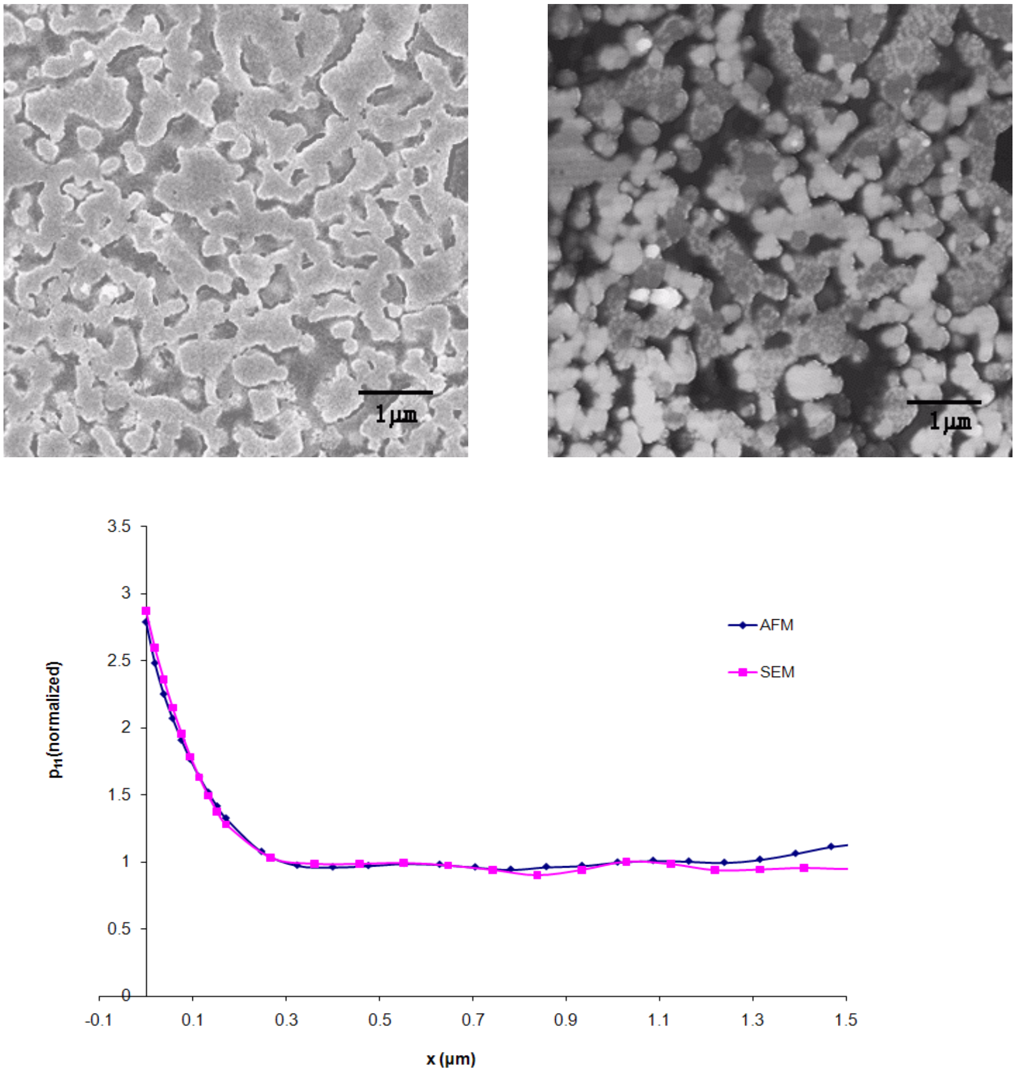

Figure 8 SEM (left) and AFM (right) images of the marked area and the comparison of two-point correlation functions (bottom)

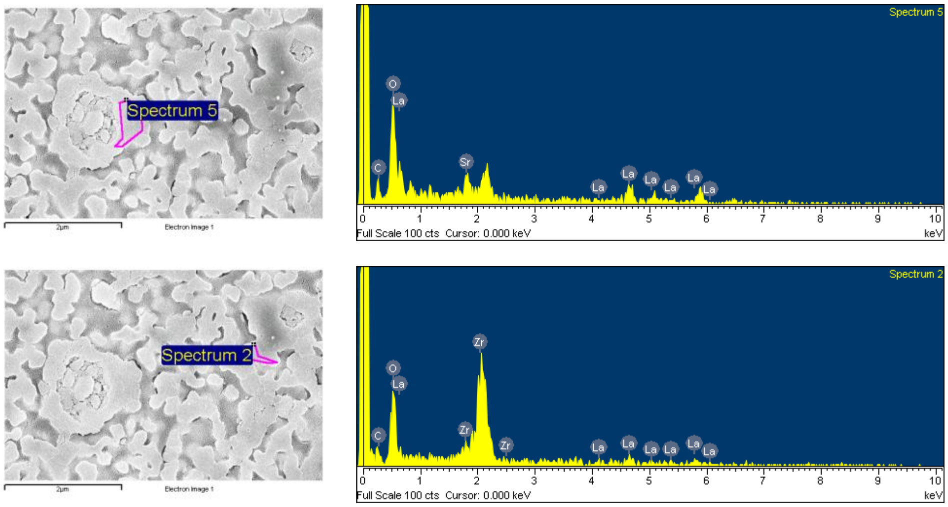

Figure 9 EDS analysis of hand-selected regions: (a) a region assumed to be LSM, and (b) a region assumed to be YSZ.

3.1.6 Stereology Based Quantitative 3D Microstructure Characterization

Volume fraction of a phase is estimated by measuring the area fraction of the phase in representative 2D sections. The area fraction of a phase is measured by dividing the total number of pixels belonging to that phase by the total number of pixels in the digital image (512×512 in the present case). In the present study, the triple phase boundary length per unit volume, the volume fractions of all the three phases (YSZ, LSM, and pores), and the total surface area interfaces between YSZ and pores, LSM and pores, and YSZ and LSM in the 3D microstructure per unit volume were estimated by performing the required measurements on a statistical microstructural sample consisting of 7 representative random segmented AFM images each covering microstrucutral area of 10 µm × 10 µm recorded with a X-Y resolution of 20 nm (source code implementing the stereological measurements in Appendix A.6 and A.7). These images contained approximately 2700 YSZ and LSM grains and 3500 triple phase boundary junctions, and therefore, constitute a large statistical sample. Consequently, the statistical estimates of the microstructural parameters obtained from these images are expected to be robust and reliable. The estimated values of volume fractions of the three phases, total surface area per unit volume of the YSZ-Pore, LSM-Pore, and YSZ-LSM interfaces per unit volume, and the corresponding statistical sampling errors are given in Table 2 and 3. The total length of the triple phase boundaries per unit volume (i.e., the length density) estimated from the measurement performed on the color-coded AFM images and the application of the stereological Eqn. (2.9) is equal to 10.8 ± 1.15 μm/μm^3. Note that the present procedure for estimation of triple phase boundary length per unit volume does not require reconstruction of opaque 3D microstructure. Wilson and co-workers [53] carried out detailed 3D microstructure reconstructions of numerous composite porous cathodes of different compositions containing YSZ, LSM, and pore phases using FIB based serial sectioning and backscattered SEM based imaging of the serial sections. They estimated the triple phase boundary length per unit volume to be in the range of 8-10 μm/μm^3. Therefore, the present data are in a good agreement with the measurements of Wilson and co-workers on reconstructed 3D microstructures. Nonetheless, the present technique does not require advanced SEM-based imaging procedures; serial sectioning using FIB (which is extremely slow process); and reconstruction of 3D microstructure. Therefore, the present AFM based microstructure observations and stereology based estimations of the microstructural properties are very efficient for simultaneous observations and quantitative characterization of the three phases (YSZ, LSM, and pores) and the triple phase boundaries in the composite porous cathode microstructures.

Table 2 Measurements of volume fraction of each phase. Porosity is calculated as the remaining volume fraction aside from YSZ and LSM.

	YSZ	**LSM**	**Porosity**
Volume fraction	28.34*	25.81%	45.84%
Sampling error[1]	2.68%	1.83%	

Table 3 Measurements of interface/surface areas per unit volume ($\mu m^2/\mu m^3$)

	YSZ/pore (S_1)	**LSM/pore (S_2)**	**YSZ-LSM (S_3)**	**Total surface area (S_1+S_2)**
Interface area ($\mu m^2/\mu m^3$)	3.87	2.32	0.63	6.19
Sampling error[1]	0.21	0.30	0.09	

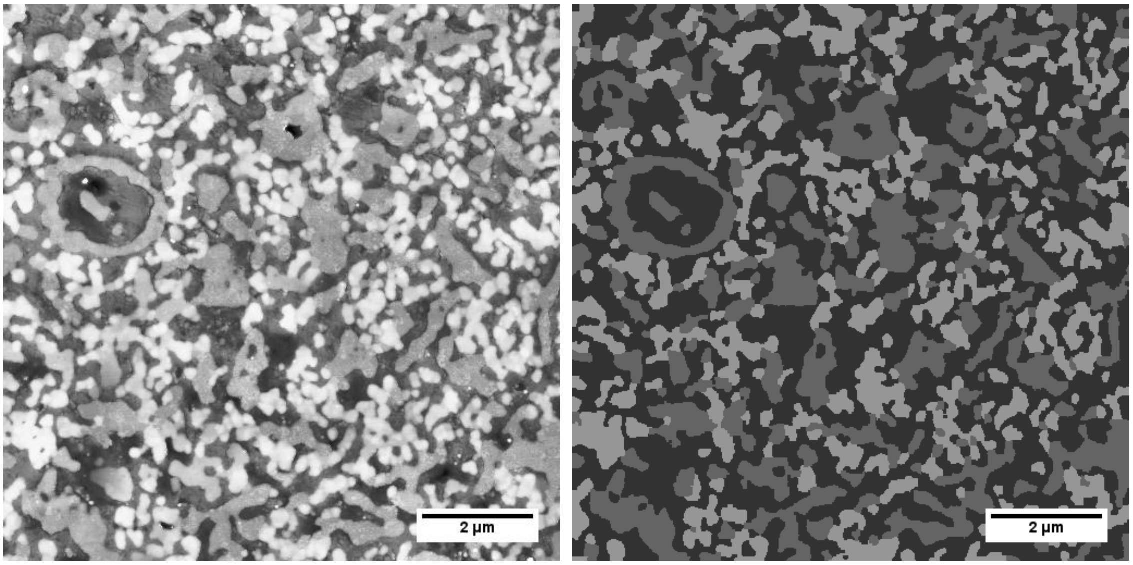

(a) (b)

Figure 10 AFM image of the etched electrode surface. (a) rendered AFM image;(b) color-coded image. In both images bright phase is YSZ, darker phase is LSM and rest are pores (PMMA filled).

3.2 Quantitative Characterization of BZCY-LSCF Composite Cathodes Microstructure

Recently, considerable research is being performed on a new electrolyte material $Ba(Zr_{0.1}Ce_{0.7}Y_{0.2})O_{3-\delta}$ (BZCY), which transports protons (hydrogen ions) rather than oxygen ions as in YSZ. A few candidate cathode materials have been investigated, including $Sm_{0.5}Sr_{0.5}CoO_3$ (SSC), $Ba_{0.5}Pr_{0.5}CoO_3$, $La_{0.5}Sr_{0.5}CoO_3$, $La_{0.6}Ba_{0.4}CoO_3$, $La_{0.7}Sr_{0.3}FeO_3$ and $La_{1-x}Sr_xCo_{1-x}Fe_xO_3$ (LSCF)[33-36]. LSCF, among the investigated cathode materials, has shown high oxygen reduction catalytic activity and excellent chemical compatibility with BZCY electrolyte [36]. Similar to the YSZ-LSM cathode, composite BZCY-LSCF cathode has shown better performance than pure LSCF cathode, which can be attributed to the increase in the length of TPB in the composite cathode [36]. While the electrochemical mechanisms in BZCY based SOFC are distinctly different from an oxygen ion conductor (e.g., YSZ) based SOFC, the role of triple phase boundaries is equally important in these next generation porous composite cathode. Accordingly, the microstructures of two BZCY-LSCF porous composites are characterized in this research. The resulting data are used in the next Chapter to validate the analytical model for L_{TPB}.

3.2.1 Material Processing

Three specimens of BZCY-LSCF porous composites having different relative amounts of BZCY and LSCF phases were prepared by Mr. Lei Yang of Professor M. Liu's research group at Georgia Tech. The LSCF powder was supplied by Fuel Cell Materials Inc., and the BZCY powder was produced in Professor Liu's laboratory. The

BZCY and LSCF powder were ultrasonically mixed with acetone in weight ratio of 1:1:1 to form a slurry. An ultrasonic cleaner was used to mix the constituents of the slurry uniformly instead of a ball-miller to eliminate any changes in the particle size distributions due to ball-milling. The slurry was brush-painted on the previously fired anode-supported electrolyte (BZCY-Ni/BZCY bilayer) and fired at 1000^oC for 3h. Three specimens with different compositions (Table 4) have been prepared.

Table 4 Compositions of BZCY-LSCF composite cathodes

Specimen ID	BZCY wt%	LSCF wt%
S1	0	100
S2	20	80
S3	40	60

3.2.2 Specimen Preparation and Metallography

The porous specimens were infiltrated with methylmethacrylate (MMA) in a vacuum chamber (Struers Epovac) at 150 mbar pressure for 2 min. The MMA infiltration was then polymerized under ultraviolet light at room temperature for 5 hr. This leads to vacuum impregnation of the pores with MMA, which eliminates “pull-outs” of grains during subsequent polishing. The vacuum impregnated specimens were mounted in a cold-mounting epoxy for grinding and polishing. The mounted specimens were polished with abrasive papers (400, 600,800 grits) and subsequently with diamond suspensions (9μm, 6 μm, 3 μm and 1 μm). Finally, the specimens were fine-polished with colloidal silica (0.06μm). The polished specimens were sputtered with gold for SEM analysis.

3.2.3 Scanning Electron Microscopy

The specimens were examined in SEM (Joel 1530 FEG-SEM) using back-scatter electron imaging mode (BSE) at a voltage of 10kV. Multiple fields of views were recorded to obtain reliable estimates of microstructure attributes (volume fractions, surface areas and L_{TPB}) using imaging processing and stereology. Figure 11 (a) (b) and (c) shows the BSE images of three specimens. There are three phases in the micrographs for (b) and (c), which can be visually identified by different grayscale levels or brightness. Since BSE images are usually dominated by atomic number contrast(Z contrast), the difference in grayscale can be accounted for by the difference in *average atomic numbers* of different phases(i.e. BZCY,LSCF and porosity) in the microstructure. An image including the electrolyte indicates that the bright phase is BZCY, which leaves the darkest phase to be porosity and the rest LSCF. An EDS analysis has also been conducted to confirm the phase identification (see Figure 12).

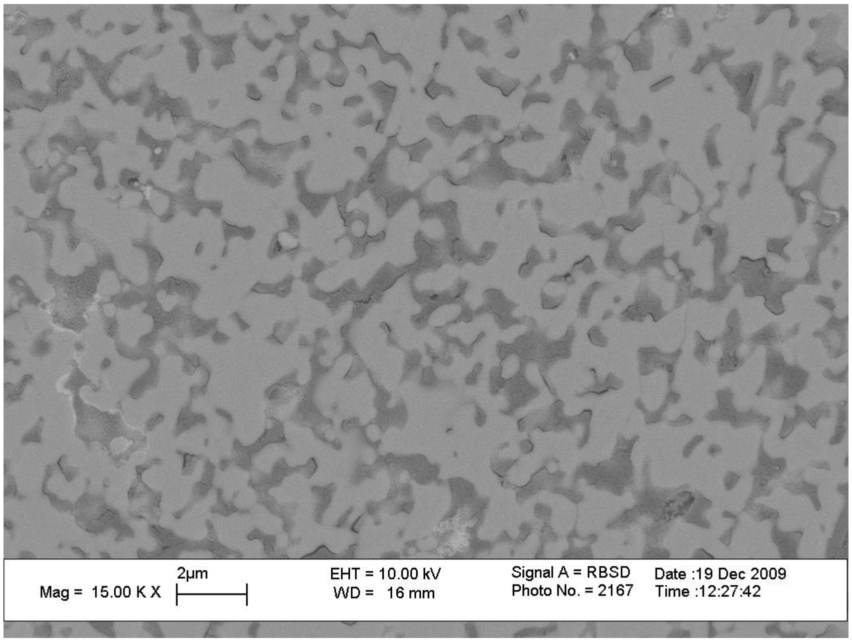

(a)

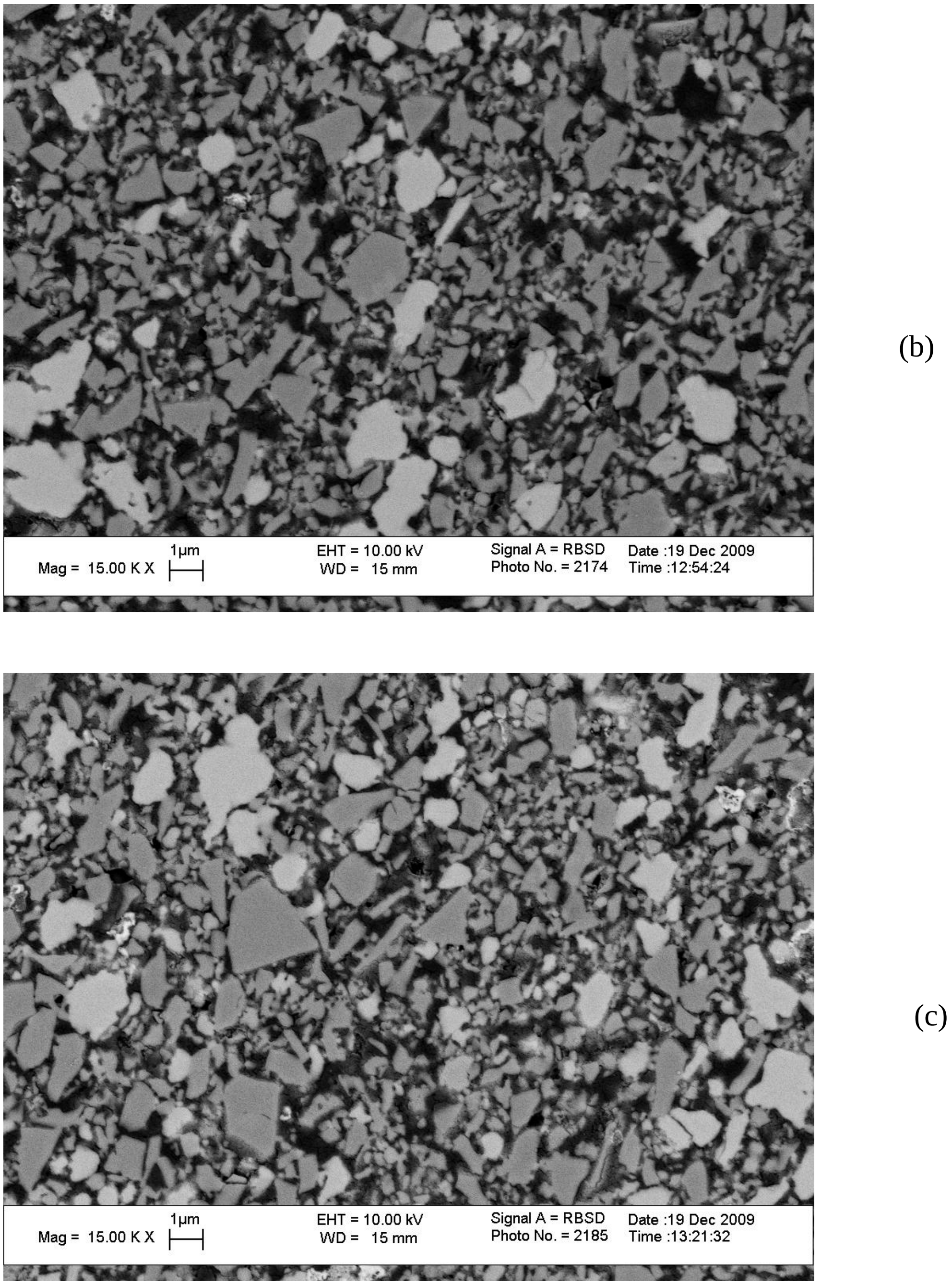

Figure 11 SEM images of LSFC-BZCY composite cathode of different compositions: (a) pure LSCF, (b) 80wt% LSCF and 20wt% BZCY and (c) 60wt% LSCF and 40wt% BZCY.

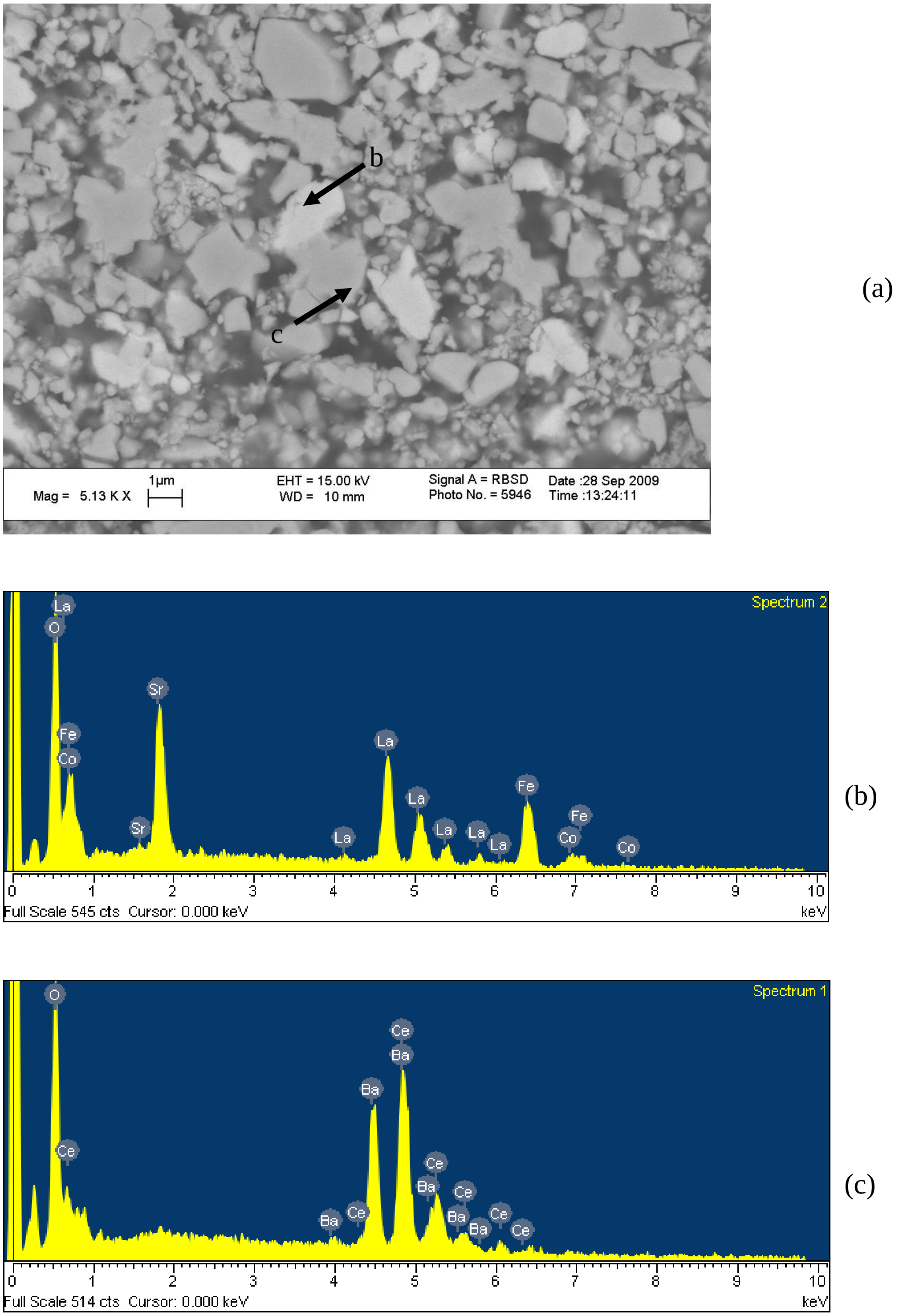

Figure 12 EDS analysis on the BZCY-LSCF composite cathode. (a) is BSE image of the microstructure;(b) and (c) are EDS spectrums of point b and c, respectively

3.2.3.1 Image Processing and Stereological Analysis

SEM images are recorded with enhanced contrast (Figure 11 (b) and (c)) so that the grayscale difference between LSCF and BZCY is large enough for automatic digital image analysis. However, image noise is also amplified because of the enhanced contrast. The SEM images for quantitative stereological analysis were record at a scanning speed of about 1min/field of view. The noise level in the as-acquired images is still not sufficiently low for automatic stereological analysis and a noise-reduction technique called anisotropic diffusion has also been used. Visual comparison between the raw SEM image and the image processed in this manner(see Figure 13 (a) and (b)) shows that anisotropic diffusion significantly reduces the noise without “smoothing out” the boundaries between LSCF, BZCY and air channels. The SEM images were then segmented using the same image analysis procedures reported in section 3.1.4 . A typical segmented image is shown in Figure 13(c). The triple phase boundary length per unit volume, the volume fractions of all the three phases (LSCF, BZCY, and pores), and the total surface area interfaces between LSCF and pores, BZCY and pores, and LSCF and BZCY in the 3D microstructure per unit volume were estimated by performing the required stereological measurements; the data are reported in Table 5. In Table 5, the difference in the measured L_{TPB} values of the two specimens is mainly due to the difference the volume fractions of BZCY and LSCF phases in the two microstructures.

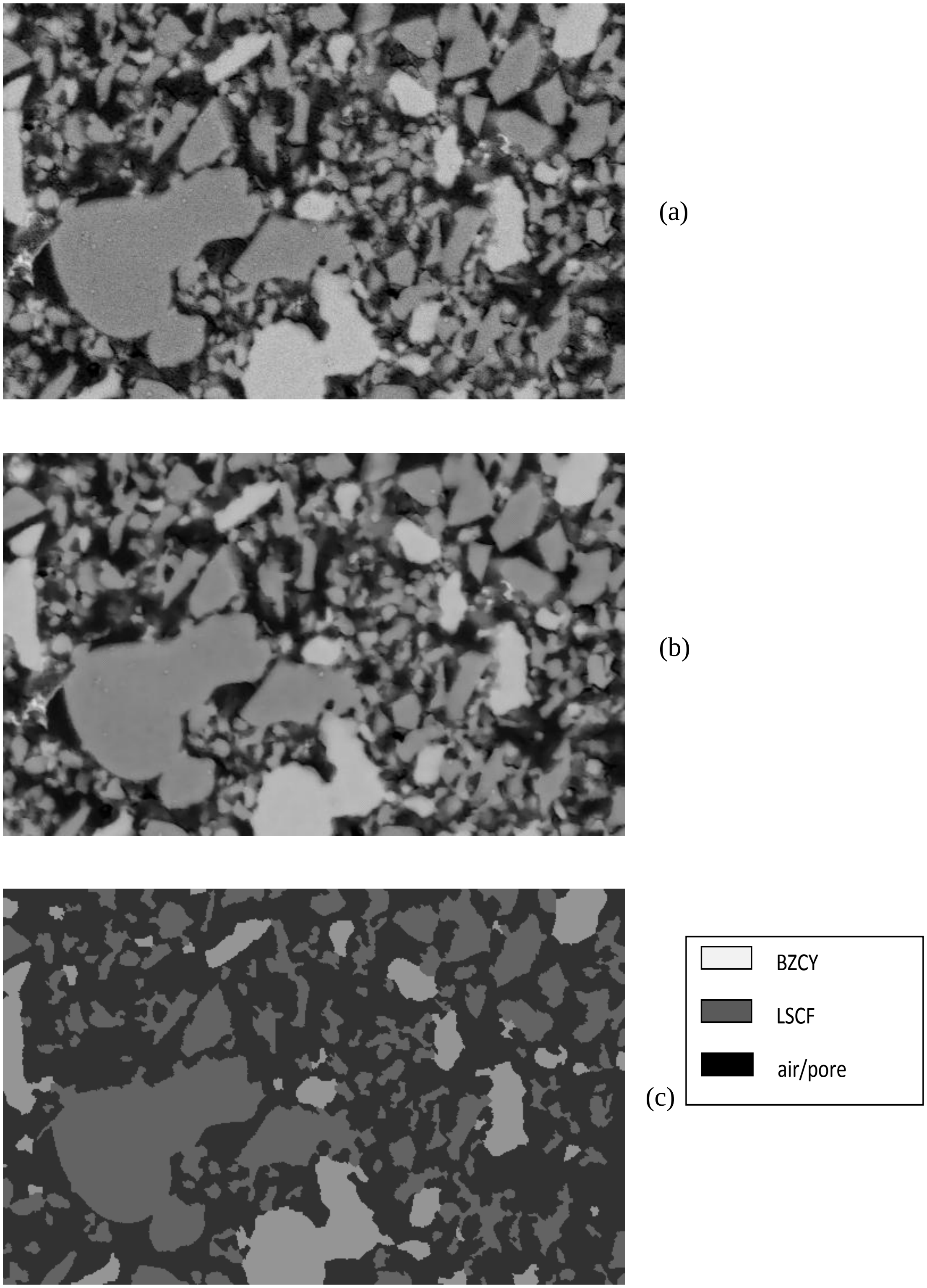

Figure 13 Digital image processing and segmentation of SEM images: (a) raw SEM image (b) noise-reduced image and (c) colored-coded image

Table 5 Microstructure attributes of BZCY-LSCF composite cathodes

ID	Composition	TPB ($\mu m/\mu m^3$)	Volume fractions			Surface/interface areas ($\mu m^2/\ \mu m^3$)		
			BZCY	LSCF	pore	BZCY -air	LSCF -air	LSCF-BZCY
S2	20wt% BZCY 80wt% LSCF	1.3	9.7%	45.1 %	45.0%	0.46	2.5	0.13
S3	40wt% BZCY 60wt% LSCF	1.8	15.0 %	24.1 %	60.7%	0.84	2.5	0.13

3.2.3.2 Powder Particle Size Profile

Geometric attributes of powder particles affect the microstructure of the composite cathode. Therefore, the powder particle size distribution is also needed for the investigation of the processing-microstructure relationships. While the particle size distribution of LSCF is available from the supplier, the BZCY powder particle size distribution was characterized using optical microscopy. BZCY powders are dispersed in cold-mounting epoxy resin. After the resin hardened, the mount was polished with SiC abrasive papers and diamond polishing fluids. The polished sections were then examined in an optical microscope (Zeiss Axiovert 200M MAT) and images were recorded. The images were converted to binary images for automatic stereological measurements (see Figure 14).

The particle size distribution (Figure 15) is estimated using Schwartz-Saltykov [58] diameter analysis. Important characteristics of the distribution are calculated from these data and summarized in Table 6.

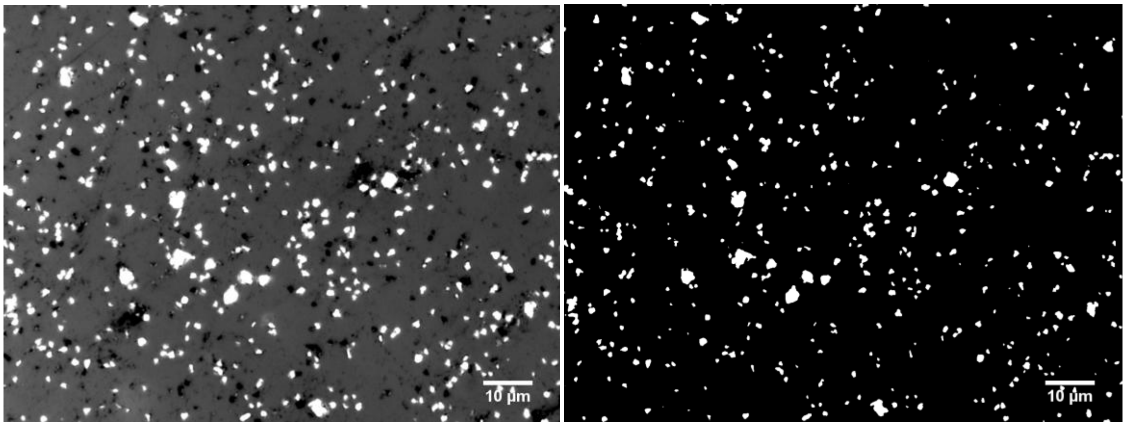

(a) (b)

Figure 14 Optical image of the a polished section of BZCY powder embedded in epoxy:(a) original optical image and (b) the corresponding segmented binary image

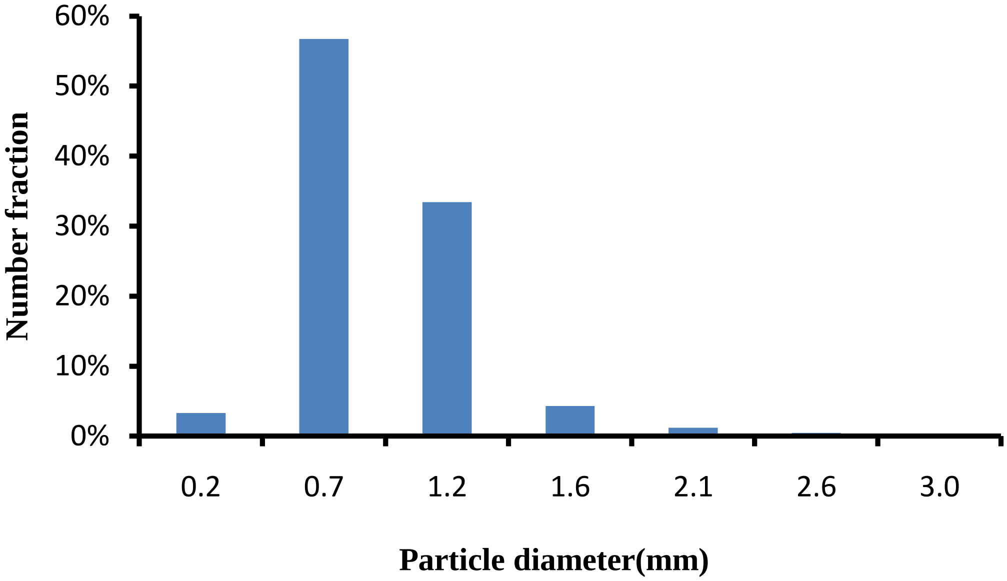

Figure 15 Particle size distribution of the BZCY powder

Table 6 Average diameter, coefficient of variation and skewness of LSCF and BZCY powder particle size distribution

Parameter	LSCF	BZCY
Average diameter($<D_L>$)	0.60μm	1.28μm
Coefficient of variation(CV_L)	0.45	0.27
Skewness(γ_L)	0.95	4.08

3.3 Microstructure Characterization of Ni-YSZ Composites for SOFC Anodes

Composites containing Ni, YSZ, and porosity phases are commonly used for SOFC anodes [6]. The performance of porous composite SOFC anodes is *microstructure sensitive*, and therefore, their microstructure characterization is of interest.

3.3.1 Material Processing

The Ni-YSZ specimen was provided by Dr. Janine Johnson and was fabricated at the Oak Ridge National Laboratories. A mixture of YSZ and NiO powders was fired at 1300^{o}C for 2h. The sintered specimen was then reduced in 4%H_2-96%Ar at 200psi, 1000^{o}C for 1h.

3.3.2 Specimen Preparation and Materialography

The porous Ni-YSZ specimen was mounted in cold-mounting epoxy (Buehler EpoFix) for handling during mechanical grinding and polishing. The resin filled the pores in the sample so that the microstructure became more resistant to possible smearing in the process of mechanical polishing. The mounted sample was polished on Buehler Phoenix Beta Grinder/Polisher with SiC abrasive papers (240, 400, 600 and 800 grits).

The sample was then polished with Buehler MetaDi Monocrystalline diamond suspension, 9μm, 6μm, 3μm and 1μm. Finally, the sample was fine-polished with Buehler MasterMet colloidal silica polishing suspension.

3.3.3 Scanning Electron Microscopy

The sample was examined in SEM (Joel 1530) without any conductive coating. At the acceleration voltage of 1kV, the Ni and YSZ showed substantial distinction in the images when the InLens detector was used for imaging; porosity was distinguished using SE2 detector. Therefore a mixed signal from InLens and SE2 detector was recorded so that all three phases (Ni, YSZ and porosity) were unambiguously identified on the SEM images.

3.3.3.1 Image Processing and Stereological Analysis

The SEM images were color-coded into three phases (Ni,YSZ and pore) to perform quantitatively analysis (volume fraction, two-point correlation functions, lineal path functions, *etc.*) using digital image analysis techniques. KS-400, a commercial software for micrograph processing, was utilized for image segmentation based on differences in grayscales (Table 7). A in-house computer code (see section 3.1.4) was used to correct the segmentation artifacts. Figure 16 shows one of the recorded SEM micrographs and the corresponding color-coded image. Each pixel in these images is 0.05μm×0.05μm.

Table 7 Grayscales thresholds for image segmentation in KS-400

Phase	Grayscale
Ni	>193
YSZ	[123,193]
Pore	<123

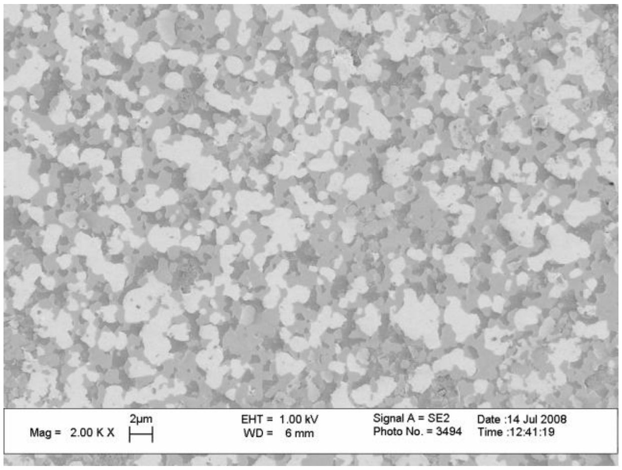

(a)

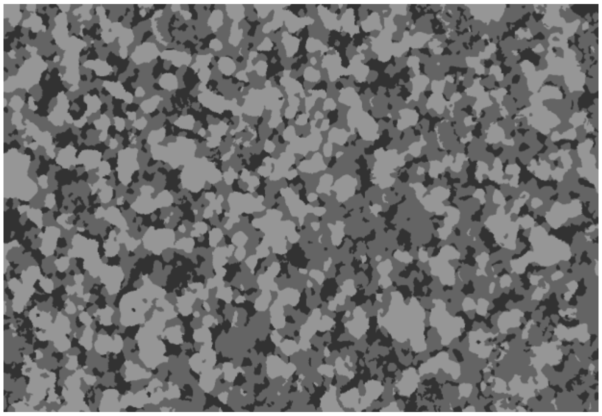

(b)

Figure 16 (a) SEM micrograph of porous Ni-YSZ cermet. (b) The color-coded image of the (a).

Surface/interface areas, volume fractions and L_{TPB} were measured on the color-coded images with the stereological techniques in section 3.1.4. The characterization results are given in Table 8.

Table 8 Surface/interface areas, volume fraction and L_{TPB} of the YSZ-Ni composite anode specimen

$L_{TPB}(\mu m/\mu m^3)$		1.41
Interface Area	Ni/YSZ($\mu m^2/\mu m^3$)	1.03
	Ni/pore ($\mu m^2/\mu m^3$)	0.28
	YSZ/pore ($\mu m^2 \mu m^3$)	1.15
Volume fractions	Pore	21.5%
	YSZ	43.2%
	Ni	35.2%

3.4 Summary

In this chapter, both composite cathodes and anodes have been microstructurally characterized. Different characterization techniques have been employed for different electrode materials. The YSZ/LSM composite cathode was characterized using AFM-based microstructure imaging; BZCY-LSCF composite cathodes were characterized using backscatter electron imaging (BSE) and the YSZ-Ni composite anode was characterized with InLens/SE2 mixed signal images. Special digital image processing algorithm has been developed to generate accurate and unbiased color-code the AFM/BSE/SEM images. The microstructure attributes were measured on the images of polished 2D sections using stereology. In the next chapter, a stochastic geometry based analytical model is developed for the microstructure of composite electrodes. An analytical expression of the length of triple phase boundaries is derived. The experimental measurements reported in this chapter have been used to validate the new model.

CHAPTER 4

ANALYTICAL MODELING OF COMPOSITE ELECTRODES

It is well known that performance of SOFC electrodes is microstructure sensitive. Therefore, development of quantitative relationships among process parameters, microstructural geometry, and electrochemical response of porous composite electrode materials is vital to the effective optimization of the performance of the SOFCs. Triple phase boundaries are the sites of key electrochemical reactions in the porous composite SOFC electrodes. As a result, total triple phase boundary length per unit volume is an important microstructural parameter that affects performance of the porous composite electrodes. The total triple phase boundary length is, to a large extent, determined by the parameters of the powder processing technique used for composite electrode fabrication [15, 43]. Therefore, it is of interest to develop quantitative relationships that express the effects of the variables such as relative amounts, morphologies, mean sizes and other distributions characteristics of the electrolyte and electronic conductor powders in the initial powder mix on the total triple phase boundary length per unit volume. Numerous theoretical studies on modeling and simulations of porous composite electrode microstructure have been reported in the literature, which are reviewed in Chapter 2. Critical analysis of these existing modeling and simulation studies reveals that (i) they are based on the central assumption that all particles are spherical, and therefore, do not capture the effects of the shapes/morphologies of the electrolyte and electronic conductor particles on the total triple phase boundary length, (ii) they do not capture the effects of powder particle size distribution characteristics such as the variance and skewness on the total triple phase boundary length, and (iii) they require critical auxiliary data such as mean 3D particle coordination number that are extremely difficult to measure experimentally or to compute theoretically without unrealistic simplifying assumptions, or generate substantial bias in the simulated total triple phase boundary length that can lead to erroneous conclusions. Therefore, there is a need to develop more general and realistic microstructure models for prediction of total triple phase boundary length in the 3D microstructures of porous composite electrodes that capture the effects of powder particle shapes/morphologies, mean particle sizes, size distributions, volume fractions, etc on the total triple phase boundary length. In this chapter, a stochastic geometry based analytical model for total triple phase boundaries in microstructures of porous composite electrodes is presented that *explicitly* expresses the effects composition, porosity, mean sizes of electrolyte and electronic conductor particles, and their size distributions and morphologies on the total triple phase boundary length per unit volume in 3D porous composite electrodes. The theoretical development of the model is presented in the next section. A detailed parametric study is performed in the subsequent section to explore the effects of numerous geometric attributes of the electrolyte and electronic conductor powder particles on the total triple phase boundary length. The parametric study leads to the suggestions for microstructure design that can optimize the total triple phase boundary length in the composite SOFC electrodes. Predictions of the new model are compared with the experimental data on the total triple phase boundary length in porous composite cathode and anode microstructures, and the predictions of the existing models and simulations. In the next chapter, the predictions of the new analytical model are further validated and the topology of the triple phase boundaries is studied using voxel-based 3D computer simulations.

4.1 Theoretical Development

Development of analytical model for total triple phase boundary length per unit volume involves three important components: (i) application of the concept of “extended” microstructure to three-phase porous composite electrode microstructure, (ii) application of stochastic geometry based stereological relationships to compute the total triple phase boundary length per unit volume in the extended microstructure and its relationship to the total triple phase boundary length in the corresponding real microstructure, and (iii) expressing the equation for total triple phase boundary length per unit volume in terms of the volume fractions of the three phases and attributes of the electrolyte and electronic conductor particle characteristics. These components of the derivation of total triple phase boundary length per unit volume are given as follows.

4.1.1 Extended Microstructure

Consider a 3D geometric microstructure model comprising an isotropic uniform random (IUR) collection of convex[2] particles of ionic conductor electrolyte (such as YSZ) and electronic conductor (such LSM in cathode or Ni in anode) in a 3D microstructural space, where the spatial arrangement of the particle centers is given by the Poisson process of spatial statistics [64], and the particles are allowed to freely

---

[2] A particle shape is convex if a line joining any (and all) two arbitrary points on its surface lies inside the particle. Spheres, ellipsoids, polyhedrons with flat faces, cylinders, cones, plates, needles, etc. are all convex.

intersect and overlap with one another depending on their spatial locations. All particles need not be of the same convex shape: a distribution of convex particle shapes is permissible. In such hypothetical microstructure, the particles have no preferred morphological orientations (i.e., they are isotropic), the probability of finding a particle center is the same at all locations in the microstructure, and there are no spatial correlations in the particle locations (i.e., uniform random spatial arrangement). The space not occupied by the electrolyte and/or electronic conductor particles is the porosity. Therefore, the microstructure contains three phases. Such geometric microstructure model is called an "extended" microstructure; the concept is widely used in modeling solid state transformations such as recrystallization and austenite to pearlite transformation in steels [65-70]. The concept of "extended" microstructure was initially developed for two-phase microstructures, but recently it has been modified to model microstructures containing three or more phases [68-70].

Clearly, in a real microstructure, the particles cannot overlap. Therefore, the properties of an extended microstructure (such as volume fractions of phases) are overestimates of the properties of the corresponding "real" microstructure. Nonetheless, the "real" microstructure model (i.e., microstructure model for composite electrode) can be recovered from the corresponding extended microstructure by subtracting the overlapped regions from it. The relationship between the volume fractions in extended *two-phase* microstructure and the corresponding real microstructure is essentially the classical Johnson-Mehl-Avrami equation, which is extensively used for modeling microstrucutral evolution during phase transformations [65-67]. Mathematically, each convex particle in an extended microstructure can be considered as a convex set, and an extended microstructure can be treated as an isotropic uniform random ensemble of convex sets. Therefore, the corresponding “real” microstructure is simply the *union* of these convex sets, which is amenable to an analytical treatment using Boolean algebra of convex sets [71]. The microstructural properties of the corresponding “real” microstructure obtained by subtracting the overlapped regions in the extended microstructure can be computed analytically from the properties of the extended microstructure [71-73]. Let $(\theta_Y)_{ex}$ and $(\theta_L)_{ex}$ be the volume fractions of YSZ and LSM in the extended microstructure. As the particles of YSZ and LSM are allowed to overlap in the extended microstructure, $(\theta_Y)_{ex}$ and $(\theta_L)_{ex}$ are not *equal to* their volume fractions θ_Y and θ_L in the corresponding real microstructure, but they are related as follows [68-70].

$$(1+\alpha)\theta_L = 1 - \exp\left\{-(1+\alpha)(\theta_L)_{ex}\right\} \tag{4.1}$$

and,

$$\frac{\alpha}{1+\alpha}\theta_Y = 1 - \exp\left\{-\frac{1+\alpha}{\alpha}(\theta_Y)_{ex}\right\} \tag{4.2}$$

Where,

$$\alpha = \frac{\theta_Y}{\theta_L} = \frac{(\theta_Y)_{ex}}{(\theta_L)_{ex}} \tag{4.3}$$

The parameter α is the relative proportion of YSZ and LSM phases in the microstructure. In a microstructure containing YSZ, LSM, and porosity, the sum of the *real* volume fractions of YSZ, LSM, and porosity must be equal to one[3]. Therefore,

---

[3] Note that in the present work, the volume fraction of a phase is equal to the total volume occupied by that phase in the microstructural space divided by the total volume of the microstrucutral space (i.e., specimen volume). This definition is different from the one used in the earlier papers on modeling of cathode microstructure [15, 17, 42].

$$\theta_Y + \theta_L + \theta_P = 1 \tag{4.4}$$

In Eqn. (4.4), θ_P is the volume fraction of the porosity phase in the real microstructure. Combining Eqn. (4.1) to (4.4) leads to the following equation for the *product* of the extended volume fractions of YSZ and LSM. This key equation will be needed subsequently.

$$(\theta_Y)_{ex}(\theta_L)_{ex} = \frac{\alpha}{(1+\alpha)^2}\left[\ln(\theta_P)\right]^2 \tag{4.5}$$

4.1.2 Relationship Between Total Triple Phase Boundary Lengths in Real and Extended Microstructures

In the extended microstructure, the YSZ and LSM particles are permitted to overlap and intersect. The lines of intersection of the YSZ and LSM particles are the lineal regions common to YSZ, LSM, and porosity, and therefore, they are the TPB of interest in the *extended* microstructure. Let $(L_{TPB})_{ex}$ be the total length of these lines of intersection in the *extended* microstructure per unit volume, and let L_{TPB} be their total length in the corresponding *real* microstructure per unit volume. In general, L_{TPB} is not equal to $(L_{TPB})_{ex}$ because not all segments of the TPB in the extended microstructure contribute to the L_{TPB} in the real microstructure: only those triple phase boundary line segments are present in the real microstructure that are not located in the space already occupied by other YSZ and/or LSM particles, i.e., those that are located in the space occupied by the porosity. In an IUR microstructure, the probability that a randomly located infinitesimal line element falls in the porosity phase is precisely equal to the volume fraction of the porosity [58, 59, 74-77], and the probability is the same for all such line elements and it is independent of the location. Therefore, the fraction of the total length of the TPB in the extended microstructure that is present in the corresponding real microstructure, $L_{TPB} / (L_{TPB})_{ex}$, is precisely equal to the volume fraction of the porosity phase, θ_P, i.e.,

$$\frac{L_{TPB}}{(L_{TPB})_{ex}} = \theta_P \tag{4.6}$$

Or,

$$L_{TPB} = (L_{TPB})_{ex}\,\theta_P \tag{4.7}$$

It remains to derive an expression for $(L_{TPB})_{ex}$ in terms of the geometric characteristics of YSZ and LSM particles to complete the derivation.

4.1.3 Relationship Between Total Triple Phase Boundary Length and Geometric Attributes of YSZ, LSM, and Porosity

Numerous geometric attributes of 3D microstructures can be statistically estimated from the measurements performed on lower dimensional manifolds such as random two-dimensional (2D) sections through the 3D microstructure using classical stereological relationships [58, 59, 74-77]. For example, volume fractions of the phases, total surface areas of microstructural surfaces per unit volume, and integral mean curvature of surfaces in a 3D microstructure can be estimated via unbiased sampling of the 3D microstructure using planes or surfaces as sampling probes [58, 59, 74-77]. Consider estimation of total surface area S_1 of surfaces of interest in the 3D microstructure of a specimen of volume $\sum$. Suppose this 3D microstructure is sampled in an unbiased[4] manner with another set of probe surfaces. This can be done by placing the probe surfaces of uniform random orientations at a large number of uniform random locations in the microstructural space of interest. Let S_{probe} be the total area of the probe surfaces. The intersections of the probe surfaces with the microstructural surfaces of interest create lines of intersection. Let L_{total} be the total length of these lines. Stochastic geometry gives the following general relationship [58, 59, 74-78].

$$\frac{S_1}{\Sigma} = \frac{4}{\pi}\frac{L_{total}}{S_{probe}} \tag{4.8}$$

Or,

$$\frac{S_1}{\Sigma} = \frac{4}{\pi}\frac{L_{total}/\Sigma}{S_{probe}/\Sigma} \tag{4.9}$$

Eqn. (4.8) and (4.9) are applicable to any 3D microstructure and the probe surfaces of any geometry (for example, probes can be surfaces of ellipsoids, polyhedrons, or planes). The only requirement is that the sampling must be unbiased, which implies that the surfaces of the probes and the surfaces of interest must have uniform random orientations and locations with respect to one another. This requirement is satisfied in our extended microstructure having uniform random orientations and locations of YSZ and LSM particles. Now, consider estimation of the total length of the TPB per unit volume $(L_{TPB})_{ex}$ in the extended microstructure using Eqn. (4.9) . Consider a thought experiment where the total surface area of YSZ particle surfaces per unit volume $(S_{YZ})_{ex}$ is to be estimated (i.e., S_1/Σ in Eqn. (4.9)) using LSM particle surfaces as *probes* via application

---

[4] Unbiased sampling implies that sampling at all locations with probes having all possible orientations is equally likely. Therefore, each microstructural feature has the same probability of being included in the statistical sample.

of Eqn. (4.9). Let $(S_{\mathrm{LM}})_{\mathrm{ex}}$ be the total area of the LSM surfaces per unit volume (i.e., probe surface area per unit volume, S_{probe}/Σ). Intersections of YSZ and probe LSM surfaces are the TPB whose total length per unit volume is $(L_{\mathrm{TPB}})_{\mathrm{ex}}$ (i.e., L_{total}/Σ). For isotropic uniform random YSZ and LSM particles, Eqn. (4.9) gives the following result[5].

$$(S_{YZ})_{ex} = \frac{4}{\pi}\left[\frac{(L_{TPB})_{ex}}{(S_{LM})_{ex}}\right] \tag{4.10}$$

or,

$$(L_{TPB})_{ex} = \frac{\pi}{4}(S_{YZ})_{ex}(S_{LM})_{ex} \tag{4.11}$$

Combining Eqn.(4.7) and (4.11) gives the following expression for the triple phase boundary length per unit volume in the corresponding real microstructure.

$$L_{TPB} = \frac{\pi}{4}\theta_P(S_{YZ})_{ex}(S_{LM})_{ex} \tag{4.12}$$

Let $\langle S_Y \rangle$ and $\langle S_L \rangle$ be the mean values of the surface areas and let $\langle V_Y \rangle$ and $\langle V_L \rangle$ be the mean volumes of the YSZ and LSM powder particles, respectively. Let N_Y and N_L be the number of YSZ and LSM particles per unit volume, respectively. Therefore,

$$(S_{YZ})_{ex} = \langle S_Y \rangle N_Y \tag{4.13}$$

$$(S_{LM})_{ex} = \langle S_L \rangle N_L \tag{4.14}$$

$$(\theta_Y)_{ex} = \langle V_Y \rangle N_Y \tag{4.15}$$

$$(\theta_L)_{ex} = \langle V_L \rangle N_L \tag{4.16}$$

---

[5] 5 If the sampling surfaces are planes (such as metallographic sectioning planes) then Eqn.(4.9) reduces to Eqn. (2.8)

Combining Eqn. (4.5) with Eqn. (4.13) to (4.16) yields the following result.

$$(S_{YZ})_{ex}(S_{LM})_{ex} = \frac{\langle S_Y\rangle\langle S_L\rangle}{\langle V_Y\rangle\langle V_L\rangle}\frac{\alpha}{(1+\alpha)^2}\left[\ln(\theta_P)\right]^2 \tag{4.17}$$

Combining Eqn. (4.12) and (4.17) gives the following result for L_{TPB}.

$$L_{TPB} = \frac{\pi}{4}\frac{\alpha}{(1+\alpha)^2}\left\{\theta_P\left[\ln(\theta_P)\right]^2\right\}\left[\frac{\langle S_Y\rangle\langle S_L\rangle}{\langle V_Y\rangle\langle V_L\rangle}\right] \tag{4.18}$$

Eqn. (4.18) is applicable to YSZ and LSM particles of any convex morphology and any size-shape distribution provided that the angular orientations and locations of the YSZ and LSM particles are uniform random. The YSZ and LSM particles need not be of the same convex morphology or same size-shape distribution; the only requirement is that each particle must have a convex shape. For example, YSZ particles can be spheres and LSM particles can be plate shaped. The result is valid for any porosity volume fraction θ_P, and any value of the ratio of the amounts of YSZ and LSM, α. It is convenient to write Eqn. (4.18) in the following form

$$L_{TPB} = \frac{\pi}{4}F_1(\alpha)F_2(\theta_P)\left[\frac{\langle S_Y\rangle\langle S_L\rangle}{\langle V_Y\rangle\langle V_L\rangle}\right] \tag{4.19}$$

where,

$$F_1(\alpha) = \frac{\alpha}{(1+\alpha)^2} \tag{4.20}$$

and,

$$F_2(\theta_P) = \theta_P\left[\ln(\theta_P)\right]^2 \tag{4.21}$$

In Eqn. (4.19), the term $F_2\left(\theta_P\right)$ *explicitly* brings out the dependence of L*TPB* on the porosity volume fraction θ_P, whereas the term $F_1(\alpha)$ captures the dependence of L$_{TPB}$ on the relative proportions of YSZ and LSM, α, in an *explicit* manner. Recall that α is equal to θ_Y / θ_L (see Eqn.(4.3)). Therefore, the factors $F_1(\alpha)$ and $F_2\left(\theta_P\right)$ completely determine how the L*TPB* varies with the volume fractions of the three phases YSZ, LSM, and porosity, θ_Y, θ_L and θ_P. The dependence of L*TPB* on the morphology, mean size, and size-shape distributions of the YSZ and LSM particles resides in the last term in the square bracket in Eqn. (4.18) and (4.19), i.e., $\frac{\langle S_Y\rangle\langle S_L\rangle}{\langle V_Y\rangle\langle V_L\rangle}$. The mean volume and surface areas of particles can expressed in terms of shape factors (that depend on morphology/shape of YSZ and LSM particles) and size as follows.

$$\langle S_Y\rangle = K_{1Y}\left\langle D_Y{}^2\right\rangle \tag{4.22}$$

$$\langle S_L\rangle = K_{1L}\left\langle D_L{}^2\right\rangle \tag{4.23}$$

$$\langle V_Y\rangle = K_{2Y}\left\langle D_Y{}^3\right\rangle \tag{4.24}$$

$$\langle V_L\rangle = K_{2L}\left\langle D_L{}^3\right\rangle \tag{4.25}$$

In the above equations, K_{1Y}, K_{1L}, K_{2Y}, K_{2L} are the shape factors that depend on the morphology of the YSZ and LSM particles. $\left\langle D_Y{}^2\right\rangle$ is the mean value of the *square* of the YSZ particle size (i.e., the second moment of the YSZ particle size distribution), and $\left\langle D_L{}^2\right\rangle$ is the mean values of *square* of the LSM particle size[6] (i.e., the second moment of

---

[6] In general, mean value of the square of the particles sizes is not equal to the square of the mean value of the particle sizes, except when all particles are of the same size. Similarly, mean value of the cube of the

the LSM particle size distribution). Similarly, $\langle D_Y{}^3 \rangle$ is the mean value of the *cube* of the YSZ particle sizes (i.e., the third moment of the YSZ particle size distribution), and $\langle D_L{}^3 \rangle$ is the mean values of *cube* of the LSM particle size (i.e., the third moment of the LSM particle size distribution). Combining Eqn. (4.19) with the Eqn. (4.22) to (4.25) gives the following result.

$$L_{TPB} = \frac{\pi}{4} F_1(\alpha) F_2(\theta_P) F_3(K) \frac{\langle D_Y{}^2 \rangle \langle D_L{}^3 \rangle}{\langle D_Y{}^3 \rangle \langle D_L{}^3 \rangle} \tag{4.26}$$

where,

$$F_3(K) = \frac{K_{1Y} K_{1L}}{K_{2Y} K_{2L}} \tag{4.27}$$

$F_3(K)$ depends only on the morphology/shape of YSZ ad LSM particles. For spherical YSZ and LSM particles, then $F_3(K)$ is equal to 36 and the diameters are the size parameters. It remains to deconvolute the effects of the mean particles sizes, spreads, and skewness of the size distributions of YSZ and LSM on the TPB that are contained in the term $\frac{\langle D_Y{}^2 \rangle \langle D_L{}^3 \rangle}{\langle D_Y{}^3 \rangle \langle D_L{}^3 \rangle}$ on the TPB. Let the variable D represent the particle sizes in a size distribution. The arithmetic mean particle size $\langle D \rangle$, the variance σ^2, the coefficient of variation CV, and the skewness γ for a size distribution function $f(D)$ are defined as follows [79, 80].

---

particles sizes is not equal to the cube of the mean value of the particle sizes, except when all particles are of the same size.

$$\langle D\rangle = \int Df\left(D\right)dD \tag{4.28}$$

$$\sigma^2 = \int\left[D-\langle D\rangle\right]^2 f\left(D\right)dD = \left\langle D^2\right\rangle - \langle D\rangle^2 \tag{4.29}$$

$$CV = \frac{\sigma}{\langle D\rangle} \tag{4.30}$$

$$\gamma = \frac{1}{\sigma^3}\int\left[D-\langle D\rangle\right]^3 f\left(D\right)dD \tag{4.31}$$

Combining Eqn. (4.29) and (4.30) gives the following result.

$$\left\langle D^2\right\rangle = \langle D\rangle^2\left(1+CV^2\right) \tag{4.32}$$

Further, Eqn. (4.31) can be cast into the following form.

$$\left\langle D^3\right\rangle = \langle D\rangle^3\left(1+3CV^2+\gamma CV^3\right) \tag{4.33}$$

Substituting Eqn. (4.32) and (4.33) into Eqn. (4.26) leads to the following result.

$$L_{TPB} = \frac{\pi}{4}F_1(\alpha)F_2(\theta_P)F_3(K)F_4(CV,\gamma)\frac{1}{\langle D_Y\rangle\langle D_L\rangle} \tag{4.34}$$

where,

$$F_4(CV,\gamma) = \frac{\left(1+CV_Y{}^2\right)\left(1+CV_L{}^2\right)}{\left(1+3CV_Y{}^2+\gamma_Y CV_Y{}^3\right)\left(1+3CV_L{}^2+\gamma_L CV_L{}^3\right)} \tag{4.35}$$

In Eqn. (4.35), CV_Y and CV_L are coefficient of variation and γ_Y and γ_L are skewness parameters of the YSZ and LSM powder size distributions, respectively. Note that $F_4(CV,\gamma)$ depends *only* on the coefficient of variation and skewness of the powder population distributions, and it *explicitly* brings out the effect of these parameters on the L_{TPB}. To the best of author's knowledge, this is the first treatment of the effects of size distribution characteristics such as coefficient of variation and skewness on the L_{TPB}.

Eqn. (4.34) predicts that for given volume fractions of YSZ, LSM, porosity, and the coefficient of variation and the skewness of the YSZ and LSM size distributions, and particle morphologies, L_{TPB} is inversely proportional to the mean size of YSZ particles, $\langle D_Y \rangle$, and the mean size of LSM particles, $\langle D_L \rangle$. Therefore, the finer the mean particle sizes of YSZ and/or LSM, the higher is the total length of the TPB per unit volume, L_{TPB}. Similar trend has been predicted by earlier simulations and analytical models for L_{TPB} in composite electrodes [3, 19, 39]. Nonetheless, earlier analytical treatments of L_{TPB} were based on an assumption that all YSZ and LSM particles are of the same size, and therefore, did not capture separate effects of different YSZ and LSM mean sizes on the L_{TPB}. The present result shows that L_{TPB} can be increased either by decreasing the mean size of YSZ particles, or LSM particles, or by decreasing the mean sizes of both the particle populations, and it *explicitly* captures the dependence of L_{TPB} on the mean particle sizes. Eqn. (4.34) also explicitly brings out the effects of other geometric characteristics on L_{TPB} through the functions $F_1(\alpha)$, $F_2(\theta_P)$, $F_3(K)$, and $F_4(CV, \gamma)$, which facilitates the parametric studies.

The present model is based on the assumptions that the YSZ and LSM particles are convex, they have uniform random angular orientations and spatial locations, and there are no spatial correlations in their locations. The approach enables a tractable analytical treatment of the geometric problem, and leads to closed form analytical solution that relates L_{TPB} to numerous geometric parameters including volume fractions of the phases; morphologies/shapes of particles; and the mean sizes, the coefficient of variation, and the skewness of YSZ and LSM size distributions. Although Eqn. (4.34) is derived in the context of the microstructures of SOFC composite electrodes, it is equally applicable to any three phase uniform random isotropic microstructure. Unlike the earlier analytical models [3, 19, 39], to calculate the L_{TPB} using Eqn. (4.34), it is not necessary to know the mean coordination number of the particles, which is difficult to measure experimentally (because reconstruction of 3D microstructure is required [49]), and is difficult to compute from theoretical considerations without making numerous simplifying assumptions. Further, earlier models and simulations assume that YSZ and LSM particles are mono-sized spheres, and therefore, did not reveal the effects of the morphology/shape of the YSZ and LSM particles and the powder characteristics such as the coefficient of variation (a measure of spread in the particle sizes) and the skewness of the size distributions on L_{TPB}.

The input size distribution data (mean sizes, coefficient of variation, and skewness) needed for the present model pertain to the electrolyte and electronic conductor particles present in the powder mix *after ball-milling* (or after any attrition process used to obtain a homogeneous powder mix) and prior to sintering (i.e., not the size distributions in the unmixed initial powders of electrolyte and electronic conductor) because operations like ball milling fragment the particles and alter the size distributions. Further, if the powder particles agglomerate during any of the powder processing steps then the distribution characteristics of the agglomerated powders must be used in Eqn. (4.34).

It is important to point out that the present model predicts the *total* (active plus inactive) triple phase boundary length. Some triple phase boundaries are *not* topologically connected to the electrical conducting paths and gas permeating pores in the microstructure, and therefore, do not participate in the electrochemical processes.

Computer simulation study reported in CHAPTER 6 shows that *beyond the percolation thresholds of electrolyte, electronic conductor, and porosity phases*, more than 80% of the total triple phase boundary length is connected to the electrical conducting paths and gas permeating pores in the microstructure. For a SOFC porous composite electrode to function, it is imperative that all three phases must percolate so that the flow of ions, electrons, and fuel/oxidant is maintained. Consequently, in the microstructural regime of interest for SOFC electrode applications, for all practical purposes, L_{TPB} predicted by Eqn. (4.34) can be regarded as the topologically connected total triple phase boundary length. However, all triple phase boundaries that are topologically connected to the electrical conductive paths and gas permeating pores also may not be *electrochemically active*. The electrochemical activity at a triple phase boundary depends on the availability of the electro-active species involved in the electrochemical reactions (e.g., $V_O^{\bullet\bullet}$, $h^{\bullet}$, and O_2) at or near the triple phase boundary, which is dictated by $V_O^{\bullet\bullet}$ transport through YSZ, $h^{\bullet}$ transport through LSM, and O_2 transport through the pores of the electrode. For a typical YSZ/LSM cathode with sufficient porosity for O_2 transport, the electrochemical activity induced by a triple phase boundary often diminishes with the distance from the interface between the YSZ/LSM composite cathode and the YSZ electrolyte because the ionic conductivity of YSZ is orders of magnitudes smaller than the electronic conductivity of LSM. Therefore, only triple phase boundary segments within a certain *effective* membrane thickness (which is less than the geometric thickness of the cathode) that are connected to the electrical conductive paths and gas permeating pores are electrochemically active [81]. Nonetheless, it can be said that in a composite cathode (or anode) having isotropic uniform random microstructure, an increase in the L_{TPB} is expected to lead to an increase in the electrochemically active triple phase boundary length per unit volume. Therefore, the microstructural engineering to optimize L_{TPB} using the present approach should also lead to an increase in the electrochemically active triple phase boundary length per unit volume, which is likely to improve the performance of the electrode.

4.2 Parametric Studies

Total triple phase boundary length per unit volume in porous composite electrode microstructures is expected to depend on the following parameters.

- Volume fractions of electrolyte, electronic conductor, and porosity phases
- Mean sizes of electrolyte and electronic conductor particles in the powder mix
- Variance and skewness of the electrolyte and electronic conductor particle size distributions in the powder mix
- Shapes/morphologies of electrolyte and electronic conductor particles

Eqn. (4.34) captures the effects of these parameters explicitly, which makes the parametric studies straightforward.

4.2.1 Effects of Mean Sizes of Electrolyte and Electronic Conductor Particles

Eqn. (4.34) predicts that for given morphologies, volume fractions, coefficient of variation, and skewness of the electrolyte and electronic conductor particle populations, L_{TPB} is inversely proportional to the mean sizes of electrolyte and electronic conductor particles, $\langle D_Y \rangle$ and $\langle D_L \rangle$ in the powder mix prior to sintering: the finer the mean particle sizes, the higher is the total triple phase boundary length. This trend is also predicted by earlier simulations and analytical models [3, 19, 39]. Nonetheless, earlier analytical treatments of L_{TPB} assumed that electrolyte and electronic conductor particles are of the same mono-size, and therefore, did not reveal the separate effects of different electrolyte and electronic conductor particle mean sizes on L_{TPB}. The present result shows that L_{TPB} can be increased by reducing the mean sizes of electrolyte or electronic conductor particles, or both, and it *explicitly* captures the dependence of L_{TPB} on the mean particle sizes.

4.2.2 Effect of Relative Proportion of Electrolyte and Electronic Conductor Phase on L_{TPB}

Relative proportion of YSZ and LSM is specified by the parameter α, which is equal to the ratio of the volume fractions of YSZ and LSM, $[\theta_Y/\theta_L]$. In Eqn. (4.34), the dependence of L_{TPB} on α is expressed by the function $F_1(\alpha)$. In principle, α can vary from zero to infinity, and at these two limits, $F_1(\alpha)$ and L_{TPB} , approach zero as they must for the model to be physically tenable. Nonetheless, for SOFC applications, YSZ, LSM, and porosity phases must percolate, and therefore, α is expected to be in the range of 0.5 to 2.5. Figure 17 shows the variation of $F_1(\alpha)$ with *α*. Observe that $F_1(\alpha)$ reaches the maximum value of 0.25 when α is equal to 1, and it varies only from 0.225 to 0.25 as α varies from 0.5 to 2.5. Consequently, L_{TPB} does not vary by more than 10% in the range of α values of interest in SOFC composite cathode applications when other geometric attributes are held constant.

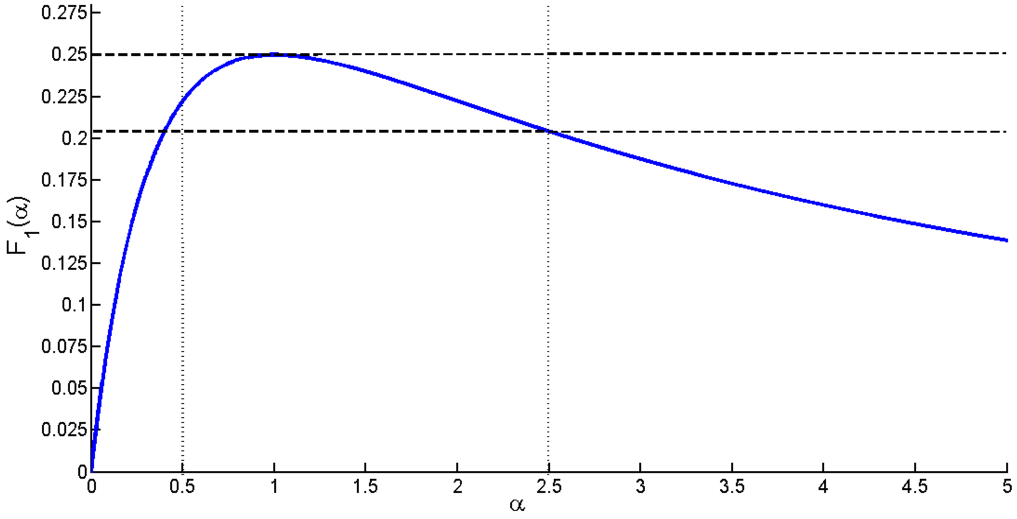

Figure 17 Plot of $F_1(\alpha)$ in the range of $0 \leq \alpha \leq 5$.

4.2.3 Porosity

In Eqn. (4.34), dependence of L_{TPB} on porosity volume fraction θ_P is captured in the function $F_2(\theta_P)$, which is equal to $\left\{\theta_P \left[\ln \theta_P\right]^2\right\}$. In principle, θ_P can vary from zero to one. At these two limits, $F_2(\theta_P)$ and consequently L_{TPB}, approach zero as they must for the model to be physically tenable. Figure 18 shows the variation of $F_2(\theta_P)$ with θ_P. Note that $F_2(\theta_P)$ has a maximum value of 0.541, when θ_P is equal to 0.135. Nonetheless, for practical SOFC composite cathode applications, YSZ, LSM, and porosity phases, must percolate. In addition, the porosity volume fraction must not be too low so that the mass transfer of gaseous species (oxygen in the cathode and fuel in the anode) is not impeded. Therefore, θ_P is expected to be in the range of 0.2 to 0.5. As the porosity volume fraction increases from 0.2 to 0.5, $F_2(\theta_P)$ decreases. *Thus, for SOFC* *composite cathode applications, for given values of α, and mean particle sizes, CV, and the skewness of the YSZ and LSM powder populations, the highest value of L_{TPB} is obtained at the lowest porosity volume fraction that permits sufficient percolation and connectivity of pores for gas permeability.*

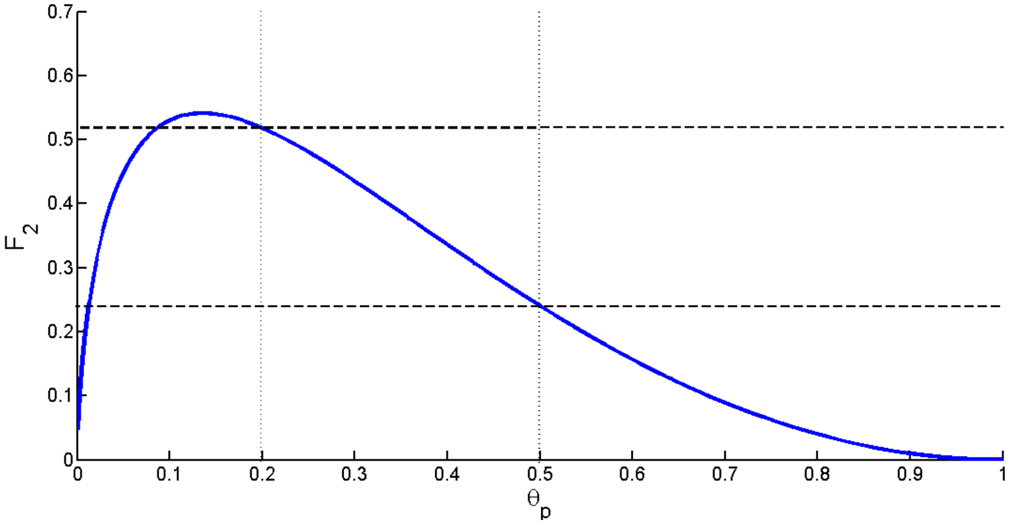

Figure 18 Plot of $F_2(\theta_p)$.

4.2.4 Effects of The Spread in the Size Distribution (CV) on L_{TPB}

In Eqn. (4.34), for given volume fraction of each constituent and mean sizes of YSZ and LSM powder particles, the dependence of L_{TPB} on the coefficient of variation CV and the skewness of YSZ and LSM particle size distributions is contained in the function $F_4(CV,\gamma)$, given by Eqn. (4.35). For mono-sized YSZ and LSM, coefficients of variation, CV_Y and CV_L, and skewness, γ_Y and γ_L are zero, and therefore, $F_4(CV,\gamma)$ is equal to one. It is well known that for any physically realizable size distribution function, skewness $\gamma \geq (-2/CV)$, and therefore, $F_4(CV,\gamma) \leq 1$. Consequently, for given relative proportion of YSZ and LSM, porosity volume fraction, and mean particle sizes of YSZ and LSM, L_{TPB} has the maximum value for *mono-size* powders of YSZ and LSM. Any spread in the size distribution (i.e., non-zero CV) reduces L_{TPB}. For symmetric size distribution functions such as the normal distribution, the skewness γ is equal to zero. For such populations, as CV_Y and CV_L become very large (strictly speaking, as they go to infinity), $F_4(CV,\gamma)$ approaches 1/9. Therefore, L_{TPB} can decrease almost by an order of magnitude as coefficients of variation of YSZ and LSM powder populations increase from zero (corresponding to mono-size) to infinity. Thus, there is a strong dependence of $F_4(CV,\gamma)$ on CV. For example, relatively small values $CV_Y = CV_L = 0.5$ in normal distributions of YSZ and LSM powders reduce F_4 (CV, γ) to 0.51 from the value of 1.0 for mono-size powders (i.e., $CV_Y = CV_L = 0$), which leads to a decrease in L_{TPB} approximately by a factor of 2 as compared to that for the mono-sized powders. Therefore, mono-size particle populations (although YSZ and LSM can have different mono-sizes) optimize L_{TPB} for given mean sizes, shapes, and volume fractions of YSZ and LSM.

4.2.5 Effect of Skewness of Size Distribution on L_{TPB}

Skewness of a size distribution (see Eqn. (4.31)) can be negative, positive, or zero. Inspection of Eqn. (4.35) reveals that for given values of CV of YSZ and LSM particles, $F_4(CV,\gamma)$ is higher (and therefore, L_{TPB} is higher) for YSZ and LSM populations that have a *negative skewness*, than for the size distributions that have *positive* skewness. In a distribution having negative skewness, the mean is lower than the median (which is lower than the mode). As particle sizes cannot be negative, clearly there is a limit on the extent to which the skewness can be negative in a physically realizable size distribution function. It is not clear if the current powder processing technologies can yield YSZ and LSM powder populations with a specified CV and/or skewness values, but if that is possible, Eqn. (4.34) and (4.35) provide a framework to compute how much improvement in L_{TPB} is possible via such process designs.

4.2.6 Effect of Powder Particle Shape/Morphology on L_{TPB}

Earlier investigations on modeling and simulations of L_{TPB} assumed that YSZ and LSM particles are spherical, and therefore, did not reveal the effects of particle shape(s) on L_{TPB}. In Eqn. (4.34), the effect of particle shape(s) on L_{TPB} is contained in the function $F_3(K)$, defined in Eqn. (4.27). For spherical YSZ and LSM particles, $F_3(K)$ is equal to 36. For given size distributions and the volume fractions of YSZ and LSM, an increase in the function $F_3(K)$ leads to an increase in L_{TPB}. Therefore, it is of interest to determine if there are particle shape(s) that increase the value of $F_3(K)$ substantially above 36. For such an analysis it is imperative to use the same geometric measure of "size" for particles of different shapes, because the objective is to determine which shape(s) increase L_{TPB} for constant values of mean sizes, size distributions, and volume fractions of the phases. For convex particles, the orientation averaged particle caliper diameter[7] is a rigorously defined unique measure of "size" that can be used to compare the "sizes" of convex particles of different shapes (say, plates and spheres). For a spherical particle, the caliper

---

[7] Caliper diameter is equal to the distance between two parallel tangent planes of a particle. For a convex particle, there are two (and exactly two) parallel tangent planes for every angular orientation. Therefore, there is a unique caliper diameter for each orientation. Caliper diameter can vary with the tangent plane orientation. The orientation averaged caliper diameter D is obtained by averaging the caliper diameter over all tangent plane orientations.

diameter is the same in all orientations, and therefore, the orientation averaged caliper diameter of a sphere is equal to its diameter. The orientation averaged caliper diameter D of any convex particle can be computed by using Minkowski's equation of integral geometry given below [76].

$$D = \frac{1}{2\pi}\left[\iint H dA + \frac{1}{2}\int \chi d\lambda\right] \tag{4.36}$$

In Eqn. (4.36), H is the local mean curvature of an infinitesimal surface element dA on the smooth surface(s) of the convex particle and the surface integral is to be performed over all smooth surfaces of the particle. The second term arises from the edges (if present) on the particle surface(s) and χ is the dihedral angle of an edge element of length dλ. The second integral is to be performed over all the edges of the particle. If the particle has only smooth surfaces (for example, ellipsoids), then the second integral is zero. In the particle population having a distribution of D values, the mean size is denoted by $\langle D \rangle$. In Eqn. (4.34), $\langle D_Y \rangle$ and $\langle D_L \rangle$ are these measures of the mean sizes of the YSZ and LSM particles.

For parametric analysis it is convenient to use cylinder as a model shape to generate equiaxed, plate-like (or flake-like), and needle-like morphologies by varying the ratio of the cylinder radius R and length L. The volume V_{cyl}, surface area S_{cyl} of a cylinder are given as follows.

$$V_{cyl} = \left[\pi (L/R)\right] R^3 \tag{4.37}$$

$$S_{cyl} = 2\pi\left[1 + (L/R)\right] R^2 \tag{4.38}$$

Applying Eqn. (4.36) to surfaces and edges of a cylinder yields the following result for the orientation averaged caliper diameter D of a cylinder.

$$D = \frac{1}{2}\left[\pi + \left(L/R\right)\right]R \tag{4.39}$$

Combining Eqn.(4.37) to (4.39) yields the following result.

$$V_{cyl} = \frac{8\pi\left(L/R\right)}{\left[\pi + \left(L/R\right)\right]^3} D^3 \tag{4.40}$$

and

$$S_{cyl} = \frac{8\pi\left[1 + \left(L/R\right)\right]}{\left[\pi + \left(L/R\right)\right]^2} D^2 \tag{4.41}$$

For cylindrical YSZ and LSM particles having constant $\left(R/L\right)$ ratio, one can write:

$$\left\langle V_Y \right\rangle = \frac{8\pi\left(L/R\right)}{\left[\pi + \left(L/R\right)\right]^3} \left\langle {D_Y}^3 \right\rangle \tag{4.42}$$

$$\left\langle S_Y \right\rangle = \frac{8\pi\left[1 + \left(L/R\right)\right]}{\left[\pi + \left(L/R\right)\right]^2} \left\langle {D_Y}^2 \right\rangle \tag{4.43}$$

$$\left\langle V_L \right\rangle = \frac{8\pi\left(L/R\right)}{\left[\pi + \left(L/R\right)\right]^3} \left\langle {D_L}^3 \right\rangle \tag{4.44}$$

$$\left\langle S_L \right\rangle = \frac{8\pi\left[1 + \left(L/R\right)\right]}{\left[\pi + \left(L/R\right)\right]^2} \left\langle {D_L}^2 \right\rangle \tag{4.45}$$

$\left\langle {D_Y}^3 \right\rangle$, $\left\langle {D_L}^3 \right\rangle$, $\left\langle {D_L}^2 \right\rangle$, $\left\langle {D_Y}^2 \right\rangle$ are the population average values of D^3 and D^2 for YSZ and LSM size distributions, respectively. Comparing Eqn. (4.42) to (4.45) with Eqn. (4.22) to (4.25) yields the shape factors K_{1Y}, K_{1L}, K_{2Y}, K_{2L}. Substituting these shape factors in Eqn. (4.25) gives the following result for cylindrical particle populations of YSZ and LSM having constant $\left(R/L\right)$.

$$F_3\left(K\right) = \left[1 + \left(L/R\right)\right]^2 \left[1 + \pi\left(R/L\right)\right]^2 \tag{4.46}$$

Figure 19 shows a plot of F_3 (K) versus (R/L). Observe that (i) for any value of (R/L), F_3 (K) for cylindrical particles is higher than that for spherical particles, (ii) F_3 (K) reaches high values for large (R/L) ratios that correspond to plate-like or flake-like particle shapes, and (iii) F_3 (K) reaches high values also when (R/L) approaches zero, which corresponds to needle-like shapes. Even for equiaxed cylindrical particles ((R/L) = 0.5), F_3 (K) = 59.44, which is higher than the value of 36 for the spherical particles. For (R/L) equal to 2, F_3 (K) is equal to 119.25: an increase of more than a factor of three over the value of 36 for spheres. Eqn. (4.32) reveals that for any given YSZ and LSM size distributions and volume fractions, L_{TPB} is directly proportional to F_3 (K). Thus, it can be concluded that for given volume fractions of the phases and particle size distributions, L_{TPB} depends significantly on the particle shape, and it is the lowest for spherical particles. *Therefore, changing the YSZ and LSM particle shapes from spherical to plate-like, or flake-like, or needle-like, can substantially increases* L_{TPB}. It is reported in the literature that at least LSM particles can be produced in a flake-like morphology [82]. Thus, the analysis brings an interesting opportunity to optimize L_{TPB} via a suitable choice of particle shapes.

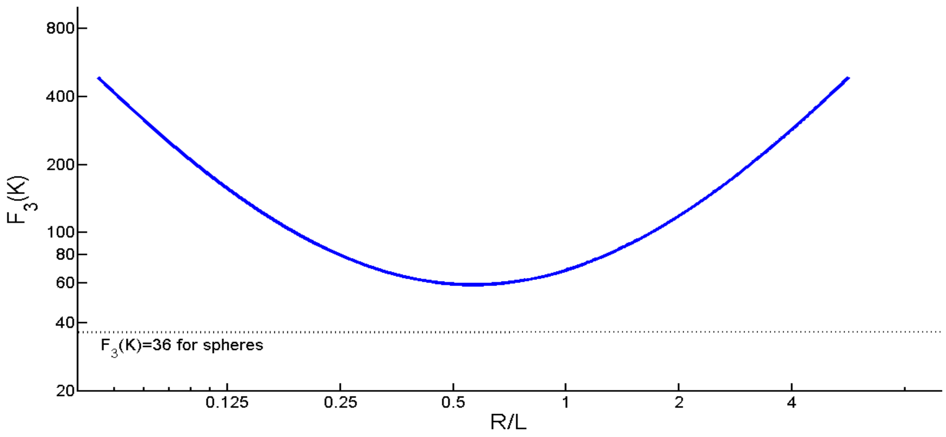

Figure 19 Plot of $F_3(K)$ with the variation of R/L, assuming cylindrical particle morphology.

4.3 Comparison of Predictions of Model with Experimental Data

In the present research, experimental measurements of total triple phase boundaries length per unit volume L_{TPB} have been performed in the microstructures of (i) porous YSZ-LSM cathode material, (ii) porous LSCF-BZCY cathode material, and (iii) porous Ni-YSZ anode material fabricated using ponder processing techniques. The details of these experiments are given in Chapter 3. In this section, these experimental data as well those reported in the literature by other researchers are used for validation of the model for L_{TPB} developed in previous section.

To verify the present model (Eqn. (4.34)), the following experimental data are needed: (i) experimentally estimated L_{TPB} either via reconstruction of 3D microstructure or by using the stereological techniques, (ii) volume fractions of YSZ, LSM, and porosity, and (iii) mean sizes, coefficient of variation, and skewness of the YSZ and LSM particle size distributions after ball milling or powder mixing operations and prior to sintering. In practice, it is very difficult to obtain precise unbiased experimental data on the CV and skewness of the powder size distributions and morphologies/shapes of the electrolyte and electronic powder populations in the powder mix because the powder particle shapes are usually complex. Nonetheless, Eqn. (4.12) (from which Eqn. (4.34) has been obtained without any additional assumptions) can be cast into a form that can be verified using the readily available data. For a isotropic uniform random microstructure, it can be shown that [83, 84]:

$$S_{YP} = \theta_P \left(S_Y\right)_{ex} \tag{4.47}$$

and,

$$S_{LP} = \theta_P \left(S_L\right)_{ex} \tag{4.48}$$

S_{YP} and S_{LP} are the total surface areas of YSZ/porosity surfaces and LSM/porosity surfaces per unit volume of specimen in the real microstructure, which can be experimentally measured. Therefore, combining Eqn.(4.12), (4.47) and (4.48) leads to the following result.

$$L_{TPB} = \frac{\pi}{4}\frac{S_{YP}S_{LP}}{\theta_P} \tag{4.49}$$

An equation analogous to Eqn. (4.49) was reported earlier in the context of microstructural evolution during phase transformations [85]. Wilson et al. [86] reconstructed 3D microstructure of SOFC *anode* containing YSZ, Ni, and porosity, and measured L_{TPB}, porosity volume fraction θ_P, and total surface areas of YSZ-porosity, S_{YP}, and Ni-Porosity, S_{NP} per unit volume directly from the reconstructed 3D images. Wilson et al. reported L_{TPB} equal to 4.28 µm/ µm^3, and θ_P, S_{YP}, and S_{NP} equal to 0.195, 0.5 µm^2/

μm^3 and 1.9 μm^2/ μm^3, respectively. Substituting these data in Eqn. (4.49) yields the value of L_{TPB} equal to 3.83 μm/μm^3, which is in very good agreement with the experimental value of 4.28 μm/μm^3. Wilson et al. [53] performed 3D microstructure reconstructions of a series of composite cathodes having different proportions of YSZ and LSM, and reported that the L_{TPB} is in the range 8-10 μm/μm^3 and it is not sensitive to the proportion of YSZ and LSM. This trend can be predicted from Eqn. (4.34), where the dependence of L_{TPB} on the relative proportion of YSZ and LSM represented by parameter α resides in the function $F_1(\alpha)$. When α is in the range 0.5 to 2.5, $F_1(\alpha)$ is in the range of (0.225 ± 0.0225), i.e., a variation of ± 10%. Thus, it is predicted that L_{TPB} is not sensitive to relative proportion of YSZ and LSM when α is in the range 0.5 to 2.5 (the range for practical applications), as observed by Wilson et al [53].

In the present research, L_{TPB} has been experimentally measured in a porous YSZ-LSM composite cathode microstructure using atomic force microscopy and stereological techniques (see section 3.1) and it is equal[8] to 10.8 ± 1.2 μm/ μm^3. The experimentally measured volume fractions of YSZ and LSM are (0.28 ± 0.03) and (0.26 ± 0.02) (Table 2), respectively, and the experimentally measured S_{YP} and S_{LP} are (3.87 ± 0.21) and (2.32 ± 0.3) μm^2/ μm^3 (Table 3), respectively. Recall that θ_P is equal to $(1-\theta_Y-\theta_L)$. Substituting these data into Eqn.(5.2) yields the computed value of L_{TPB} equal to (15.8 ± 4.3) μm/ μm^3. The large error bar in the computed L_{TPB} is because each of the three experimentally measured parameters on the right hand side in Eqn. (4.49) has a statistical sampling error. Considering large sampling error associated with computed L_{TPB}, there is reasonable agreement between the computed and experimentally measured L_{TPB} values.

---

[8] The error bars are statistical sampling errors for 95% confidence interval

In this research, the powder processing technique used for fabrication of Ni-YSZ composite anode is different from that used for the YSZ-LSM and BZCY-LSCF composite cathodes (see section 3.3.1). The starting powders for Ni-YSZ anode are nickel-oxide (NiO) and YSZ. The powder mix is fired first and then treated in a hydrogen atmosphere, which reduces NiO to Ni. The volume change associated with the reaction changes the size of Ni and increases the porosity volume fraction in the sintered microstructure. Consequently, the initial size distribution of NiO cannot be used as input data to compute L_{TPB} using Eqn. (4.34). Nonetheless, as before, Eqn. (4.49) can be used to validate the model. In this case, the L_{TPB} calculated using experimental data on volume fraction of porosity, surface area per unit volume of Ni-pore interfaces, and surface area part unit volume of YSZ-pore interfaces and Eqn. (4.49) is equal to 1.2 $\mu m/\mu m^3$, which is in good agreement with the experimentally measured value of L_{TPB} of 1.4 $\mu m/\mu m^3$.

The quantitative microstructural data on two BZCY proton conductor based composite cathodes are reported in section 3.2. In the case of LSCF-BZCY composite cathodes, the powder of each component was ultrasonically mixed instead of ball-milled, so that the particle sizes and morphologies remain unchanged before and after powder mixing, and therefore, the powders could be quantitatively characterized. The quantitative characterization combined with the compositions and porosities of the LSCF-BZCY makes it possible to directly verify the predictions of Eqn. (4.34). In the current study, the LSCF powder is a commercial powder and the particle size distribution is provided by the supplier; the BZCY powder is produced in the lab and has been quantitatively characterized with optical microscopy and Schwartz-Saltykov diameter analysis. The particle size distribution characteristics are summarized in Table 6. Recall that Eqn. (4.34) calculates the length of triple phase boundaries per unit volume with given composition (α), porosity volume fraction (θ_p), particle morphology (K), average particle sizes ($<D_Y>$, $<D_L>$ and particle size distribution characteristics (coefficient of variance CV and skewness γ). The composition and porosity volume fractions are measured experimentally (see Table 5), whereas they can be determined *before* the composite cathode is fabricated by controlling the composition of the powder mixture of BZCY and LSC, and the amount of pore forming agent in the slurry. The average particle sizes and particle size distribution characteristics are summarized in Table 6. Since the particles of both BZCY and LSCF are equiaxed, it is assumed that $F_3(K)=60$ (see section 4.2.6). In Table 7 the L_{TPB} calculated using the model is compared with experimentally measured L_{TBP}. The experimentally measured and predicted L_{TBP} values are comparable.

Table 9 Calculated and experimentally measure L_{TPB} for two composite cathode specimens (S2 and S3)

L_{TPB}	S2	S3
L_{TPB},experimental(μm/μm^3)	1.3	1.8
L_{TPB} calculated using the model, (μm/μm^3)	1.5	1.3

4.4 Comparison of Predictions of the Model with Simulations and Models Reported in Literature

Ali et al. [3] performed simulations of composite cathode microstructures involving random packing of impenetrable mono-sized spheres followed by 10% dilation of the particle diameters to create triple phase boundaries. The simulations predict that the L_{TPB}

decreases with increasing particle size, with a trend similar to that predicted by Eqn. (4.34). Nonetheless, the simulated triple phase boundary length reported by these researchers is the *active* L_{TPB}, whereas Eqn. (4.34) predicts the total (active plus inactive) L_{TPB}. As mentioned earlier, beyond the percolation threshold, about 80% or more of the total L_{TPB} is active L_{TPB}, and therefore, there is no significant difference between the two. Consequently, the simulated L_{TPB} reported by Ali et al. [3] can be compared with the predictions of Eqn. (4.34) for the porosity volume fractions in the range of 0.3 to 0.5, and relative proportions of YSZ and LSM (i.e., parameter α in equation (34)) in the range of 0.5 to 2.5. Table I reveals that the values of simulated L_{TPB} obtained by Ali et al. [3] for the porosity volume fraction and α in this range are in good agreement with the corresponding values computed using Eqn. (4.34).

Table 10 Comparison of L_{TPB} between Ali's simulation model and the current analytical model Eqn. (4.34)

θ_Y	α	θ_P	D_Y , D_L	Simulated L_{TPB} (μm/μm^3) (Ali[3])	Computed L_{TPB} Using Eqn. (4.34) (μm/μm^3)
22%-28%	0.46-0.67	30%	1μm,2μm	1.2-1.3	1.3-1.5
37%-42%	1.1-1.5	30%	2μm,1μm	1.2-1.3	1.3-1.5
28%-42%	0.7-1.5	30%	2μm,2μm	0.5-0.6	0.7-0.8

Schneider et al.[19] have proposed the following analytical equation for total (active plus inactive) L_{TPB} based on random packing of mono-size spheres of radius r.

$$L_{TPB} = \frac{3d}{r^2}\sqrt{1-\left(\frac{d_0}{d}\right)^{1/3}}\,\varphi_{io}\left(1-\varphi_{io}\right)Z \qquad (4.50)$$

where,

$$\phi_{io} = \frac{\theta_Y}{\theta_Y + \theta_L} = \frac{\alpha}{1+\alpha} \tag{4.51}$$

In Eqn. (4.50), d_o is the density of the powder mix before sintering, d is the density after sintering, and Z is the mean coordination number of the particles. Interestingly, the $\phi_{io}\left(1-\phi_{io}\right)$ factor in Eqn. (4.50) is equal to $\alpha/\left(1+\alpha\right)^2$, i.e., $F_1(\alpha)$ in Eqn. (4.34), and for mono-sized YSZ and LSM having the same radius r, equation (39) and equation (34) predict that L_{TPB} is inversely proportional to the square of the particle size. However, Eqn. (4.34) is applicable to YSZ and LSM particles having any size distribution and convex particle shape(s). On the other hand, Schneider et al. assume that YSZ and LSM particles are spherical and mono-sized, and to compute L_{TPB} using their equation it is necessary to *assume* a value for the mean coordination number Z and the density of initial powder mix d_o. Further, Eqn. (4.50) leads to a physically unacceptable limit as d approaches 1 (i.e., fully dense material). In the limit of $d \rightarrow 1$ (i.e., porosity volume fraction $\theta_P \rightarrow 0$) the L_{TPB} must approach zero because YSZ-LSM-porosity Triple phase boundaries cannot exist when there are no pores. However, Eqn. (4.50) predicts a non-zero value of L_{TPB} as $d \rightarrow 1$, which is physically untenable. On the other hand, the L_{TPB} predicted by Eqn. (4.34) reaches the correct limit of zero as the volume fraction of porosity θ_P approaches zero or one. Schneider et al. computed the values of L_{TPB} from Eqn. (4.50) assuming $d_0 = 0.5$ and $Z = 6.3$. For these values of d_0 and *Z*, Eqn. (4.50) gives L_{TPB} in the range of 1.1-1.2 $\mu m/\mu m^3$ when r = 1 μm and D = 0.75 for ϕ_{io} in the range of 0.3 to 0.7. For the same range of ϕ_{io}, and r and d values, Eqn. (4.34) yields L_{TPB} in the range of 0.7-

0.84 μm/μm^3, which is somewhat lower than that obtained from Eqn. (4.50). These differences are probably due to the values of d_0 and Z assumed by Schneider et al. (somewhat different values of these parameters lead to better agreement) and/or because Eqn. (4.50) is inaccurate at high values of d, as it gives physically unacceptable nonzero value of L_{TPB} as d approaches one.

4.5 Guidelines for Optimization of Total Triple Phase Boundary Length

Detailed parametric analysis leads to the following guidelines for the optimization of total triple phase boundary length per unit volume in the porous composite electrode microstructures.

- For electrolyte and electronic conductor volume fraction in the regime of interest in the SOFC applications where both the phases percolate, the relative proportion of electrolyte and electronic conductor in the porous composite electrode does not significantly affect L_{TPB}.
- For given relative proportion of electrolyte and electronic conductor phases, and given mean sizes, CV, and skewness of electrolyte and electronic conductor particle size distributions in the powder mix, the highest value of L_{TPB} is obtained at the *lowest* value of the porosity volume fraction that yields sufficient percolation and connectivity of pores for fuel/oxidant flow.
- For given relative proportion of electrolyte and electronic conductor phases, porosity volume fraction, and given mean sizes, CV, and skewness of electrolyte and electronic conductor particle size distributions in the powder mix, L_{TPB} is the lowest

when electrolyte and electronic conductor particles have spherical shape, and it can be substantially increased by using flake-like, plate-like, or needle-like morphologies of electrolyte and electronic conductor particles.

- L_{TPB} is inversely proportional to the product of the mean sizes of the electrolyte and electronic conductor particles. Therefore, a decrease in the mean size of electrolyte particles or electronic conductor particles, or both increases L_{TPB}.
- Mono-size electrolyte and electronic conductor particle populations lead to higher L_{TPB} as compared to the populations having a distribution of sizes. Size distributions with large spread (high CV) can reduce the L_{TPB} by almost an order of magnitude. For a given CV and mean size, size distributions with negative skewness lead to a *higher* value of L_{TPB}.

CHAPTER 5

THREE-DIMENSIONAL VOXEL-BASED SIMULATION OF COMPOSITE ELECTRODES

A stochastic geometry based analytical model for total triple phase boundary length is presented in the previous chapter. In this chapter, this analytical model is further validated via comparisons with the results of simulations of 3D microstructures of SOFC three-phase composite electrodes. The simulations also enable voxel-based visualizations of these 3D microstructures that are potentially useful for implementations as representative volume elements (RVEs) in the 3D finite-difference based simulations of the electrochemical behavior of the electrodes. The voxel-based 3D microstructure simulations also permit computations of topologically connected triple phase boundary length, which are reported in the next chapter. The algorithm for the voxel-based microstructure simulations is described in the next section, which is followed by comparisons of simulated total triple phase boundary length per unit volume with the predictions of the analytical model presented in the previous chapter.

5.1 Algorithm

The simulations are based on a Monte Carlo scheme [87]. A digitized cube of unit size containing ~6 x 10^7 cubic voxels is first generated in the simulation space. The position of each voxel is specified by its digitized (X, Y, Z) coordinates. Next, N^{IC} number of one voxel size particle centers of ionic conductor phase (electrolyte) and N^{EC} number of centers of electronic conductor phase particles are generated at uniform random locations in the simulated space using a type B lagged-Fibonacci [88] random number generator[9] without any spatial correlations between the electronic conductor and ionic conductor particle locations. The algorithm required for microstructures containing spherical particles is different from the one required for convex non-spherical particles. These algorithms are described as follows.

5.1.1 Algorithm for Simulations with Spherical Particles

In the present simulations, spherical ionic and electronic conductor particles can be of the same or different mono-sizes. The "nucleated" particles are sequentially grown in small voxel increments proportional to their respective final mono-sizes R^{IC} and R^{EC} in the microstructure till the final sizes are attained. The particles are allowed to freely grow in the simulation space (all overlaps are permitted) to simulate "extended" microstructure. This can be visualized as an evolution of an extended microstructure during a site saturated phase transformation where the particles of each constituent grow at a constant rate that is proportional to their final size. During such microstructure evolution the ratio of the extended volume fractions of the ionic conductor and electronic conductor remains constant; let α be this ratio.

To visualize the simulated microstructure is essentially to determine to which microstructural phase each voxel belongs in the digitized microstructure. Without any loss of generality let us assume $R^{IC} > R^{EC}$. A voxel P is labeled as the phase of the particle that *sweeps it first during the microstructure evolution,* or

---

[9] The lagged-Fibonacci pseudorandom number generator has a resolution of 32 bits and the cycle lengths are random, which indicate a more unpredictable behavior than a traditional fixed cycle length pseudorandom number generator such as the ANSI-C random number function.

$$L(P) = \underset{i}{\operatorname{argmin}} \left(\frac{d^i(P)}{R^i} \right), i \in \{EC, IC\}, d^i(P) \leq R^i \qquad (5.1)$$

In Eqn. (5.1), L(P) is the label of voxel P and the possible outcomes are electronic conductor (EC), ionic conductor (IC) or porosity. The variable $d^i(P)$ is the distance between the voxel P and its nearest neighboring particle of phase i, which can be electronic conductor (EC) or ionic conductor (IC). R^i is the radius of a particle of phase i.

One can now arrive at the corresponding "real" microstructure simply by assigning a given voxel to a specific phase using the following rules:

i) If the voxel has no neighboring particle center up to distance R^{IC}, the voxel is labeled as gas pore;

ii) If there is no ionic conductor particle center up to distance R^{IC} and there is at least one electronic conductor particle center within distance R^{EC}, the voxel is labeled as EC;

iii) If there is no electronic conductor particle center up to distance R^{EC} and there is at least one ionic conductor particle center within distance R^{IC}, the voxel is labeled as IC;

iv) If the distances from the nearest neighboring ionic conductor and electronic conductor particle centers are both smaller than their corresponding radii, the voxel is assigned to the phase for which the ratio of its distance to the radius of the particle is smaller (Eqn. (5.1)).

The algorithm is implemented with an in-house computer code in Appendix A.3.

5.1.2 Algorithm for Simulations with Non-spherical Convex Particles

While the algorithm in the previous section limits the particle morphology to spheres, it can be modified to accommodate particles of any convex shape. First the particle centers are randomly positioned in the simulation box in the same way as the simulations with spherical particles. In addition to their positions, particles of convex shaped have three additional degrees of freedom that are associated with their angular orientations. In general, a particle can be rotated to a new orientation in two steps: 1) rotate the particle around its characteristics dimension axis by angle β**;** 2) rotate the characteristic dimension axis by spherical polar angle θ and ϕ with respect to external reference axes. Therefore, three angular parameters are needed to specify the orientation of a particle of a convex shape. Furthermore, the particles must be randomly oriented so that the requirement of isotropy is[10] fulfilled in the simulated microstructure.

In general, a convex-shaped particle can be uniquely specified by a vector function $\vec{\mathbf{R}}$ that gives the position vectors of the points on the surface of the particle. The random orientation of the particle is specified by an orientation matrix **M** generated using the algorithm developed by Arvo[5]. The rotated particle is then obtained by multiplying the column matrix corresponding to $\vec{\mathbf{R}}$ by the matrix **M**:

$$\vec{\mathbf{R}}' = \mathbf{M} \bullet \vec{\mathbf{R}} \tag{5.2}$$

---

[10] The microstructure is required to be isotropic for Eqn. (4.8) to be valid. This requirement is fulfilled in the simulations with spherical particles because spheres have inherent isotropy. Convex shapes particles, however, are not isotropic and therefore the microstructure isotropy must be introduced by orientation randomization.

In Eqn. (5.2), $\vec{\mathbf{R}}$ is in the Cartesian coordinate system. The multiplication is a matrix product.

Now the "real" microstructure having non-spherical convex particles can be simulated with the steps similar to those used to simulate microstructure with spherical particles. A voxel P is labeled as the phase of the particle that *sweeps it first during the microstructure evolution* in which each constituent grow at a constant rate that is proportional to their final sizes, until the final particle sizes is reached. The phase assignment of a spatial point P is therefore given by

$$L(P) = \underset{i}{\operatorname{argmin}}\left(\frac{d^i(P)}{R^i}\right), i \in \{EC, IC\}, d^i(P) \leq R^i \tag{5.3}$$

R^i is the "radius" of the *rotated* particle of phase i (electronic conductor or ionic conductor) in the direction of the vector that starts at the center of the particle and ends at the voxel P (see Figure 20). $\mathbf{d}^i(P)$ is the distance vector between P and the nearest particle center of phase i. Eqn. (5.3) assigns the voxel P to the phase which has the smaller ratio of its distance to the voxel P and the directional radius R^i.

Each voxel is assigned to a phase of ionic conductor (IC), electronic conductor (EC) or gas pores)

i) If the voxel has no neighboring particle center to a distance of R^{IC} and R^{EC}, the voxel is labeled as gas pore;

ii) If there is no ionic conductor particle center to a distance of R^{IC} and there is at least one electronic conductor particle center within a distance of R^{EC}, the voxel is labeled as EC;

iii) If there is no electronic conductor particle center to a distance of R^{EC} and there is at least one ionic conductor particle center within a distance of R^{IC}, the voxel is labeled as IC;

iv) If the distances from the nearest neighboring ionic conductor and electronic conductor particle centers are both smaller than R^{IC} and R^{EC}, respectively, the voxel is labeled according to Eqn.(5.3)

The algorithm is implemented with an in-house computer code in Appendix A.4.

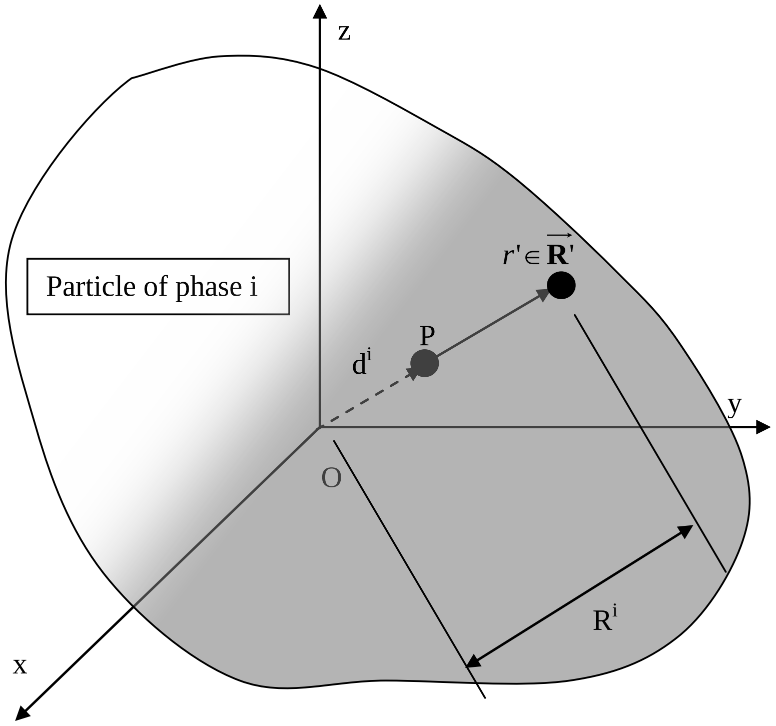

Figure 20 Depiction of the geometric relationships in Eqn. (5.3) .

5.2 Simulated Microstructures of Composite Electrodes

A series of microstructures with different compositions, porosity and particle size ratios have been simulated. The simulations are first implemented in a cubic box and then the boundary of a thickness equal to the larger of the particle radii is removed so that the simulations are free from edge effects. Figure 23 shows 3D surface-renderings and a cross-section of a simulated microstructure composed of spherical component powder particles. Simulations have also been performed to incorporate non-spherical component particles. Cylindrical particles of different aspect ratios (L/R) have been used for these simulations. Figure 24 shows 3D surface-renderings and a cross-section of a simulated microstructure composed of needle-shaped (L/R = 9) component powder particles . Figure 25 shows the renderings of simulations composed of disk-shaped (L/R = 1/3) particles.

5.3 Validation of the Analytical Model

Since all the parametric results rely on Eqn. (4.34), it is necessary to evaluate it further. The most rigorous test is to generate simulations of the model, measure the lengths of the triple phase boundaries in the simulated microstructures and compare them with the predictions of Eqn. (4.34) . For each simulation, L_{TBP} is calculated by Eqn. (4.34) and measured in the simulated microstructure using the technique described in section 2.5. A plot of the calculated L_{TPB} and measured L_{TPB} is given in Figure 21. It can be seen that L_{TPB} in the simulated microstructure matches reasonably well with predictions of Eqn. (4.34). The slight deviation from the y=x line is due to the measurement error caused by pixelation in the digital simulations.

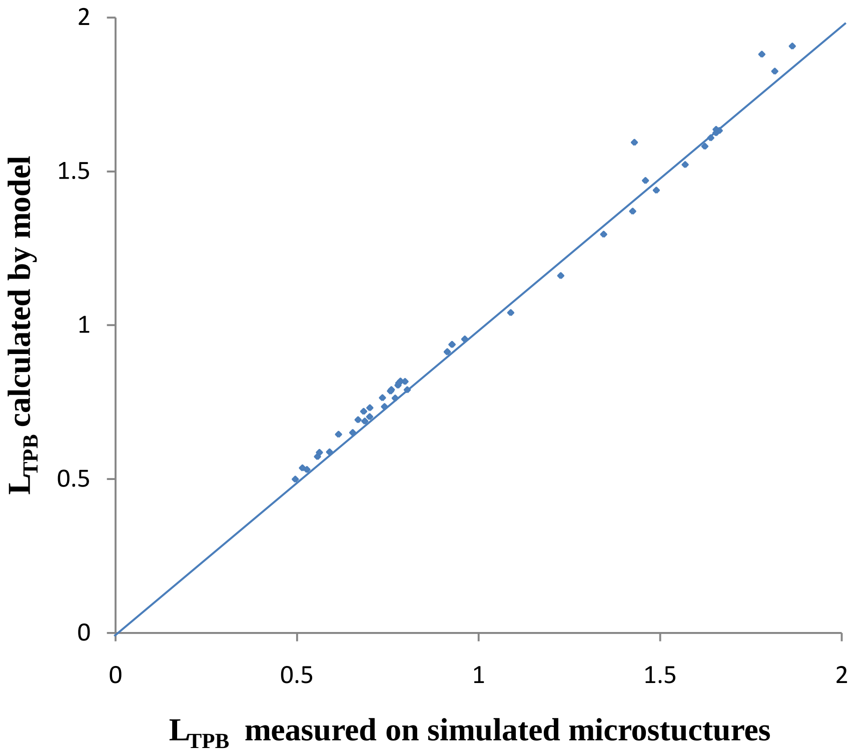

Figure 21 L_{TPB} measured in the simulation with spherical particles and calculated by Eqn. (4.34)

A similar plot has also been generated for simulations with cylindrical particles (see Figure 22). In these simulations, the aspect ratios vary from those of needle-like shapes to plate-like shapes. The L_{TPB} in the simulation is also consistent with the calculated values as demonstrated in Figure 22.

Therefore, the simulations clearly validate the analytical model for LTPB develop in chapter 4.

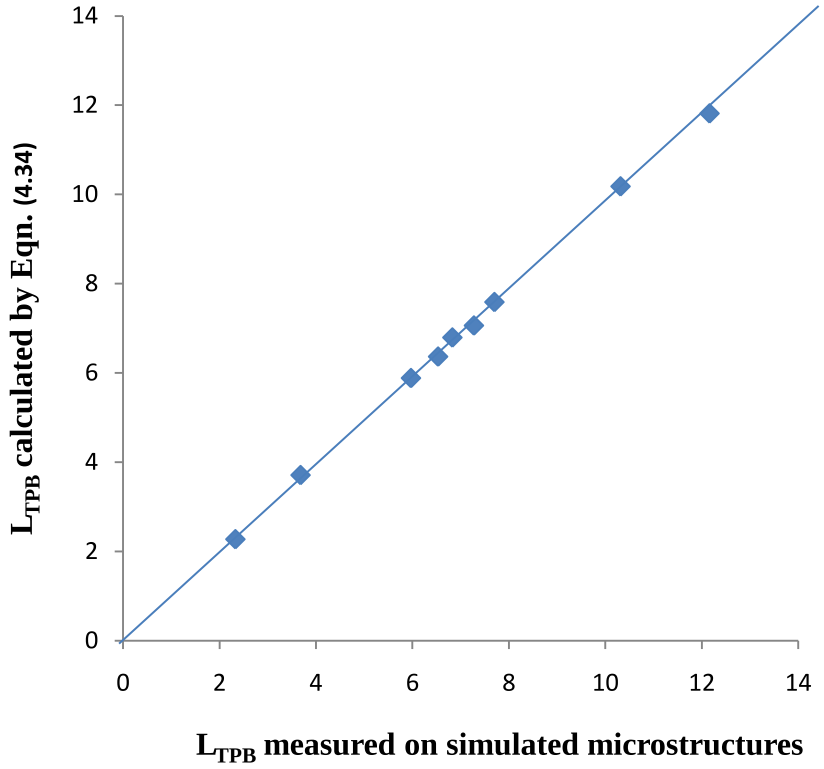

Figure 22 L_{TPB} measured in the simulations with cylindrical particles and calculated by Eqn. (4.34)

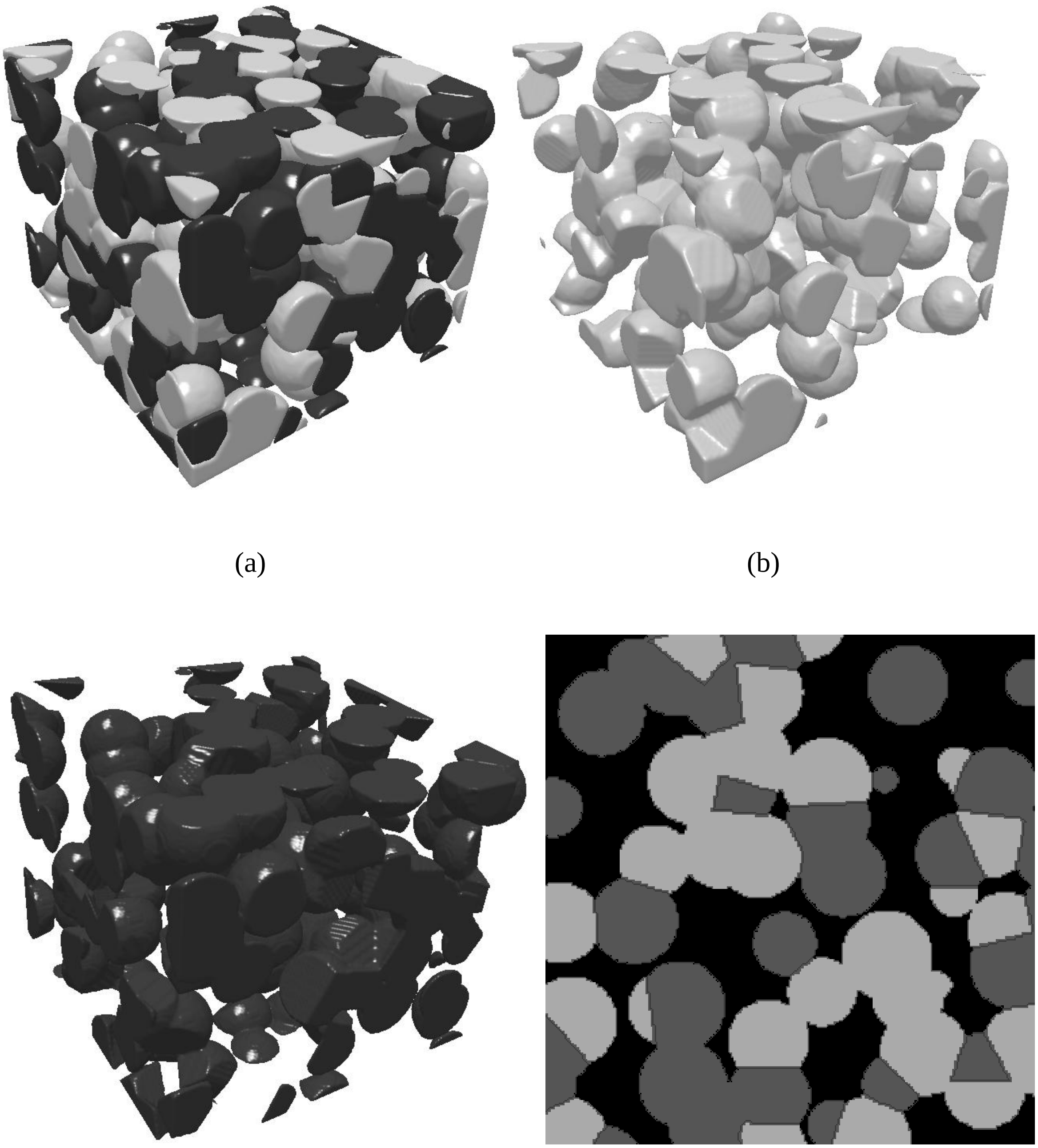

(a) (b)

(c) (d)

Figure 23 A segment of a simulation microstructure of a composite electrode with 40%vol porosity, 30%vol electronic conductor and 30%vol ionic conductor and equal particle sizes. (a) is the surface rendering of the 3D simulation;(b) and (c) are the surface renderings of the electronic and ionic conductor, respectively;(d) is a cross-section in (a).

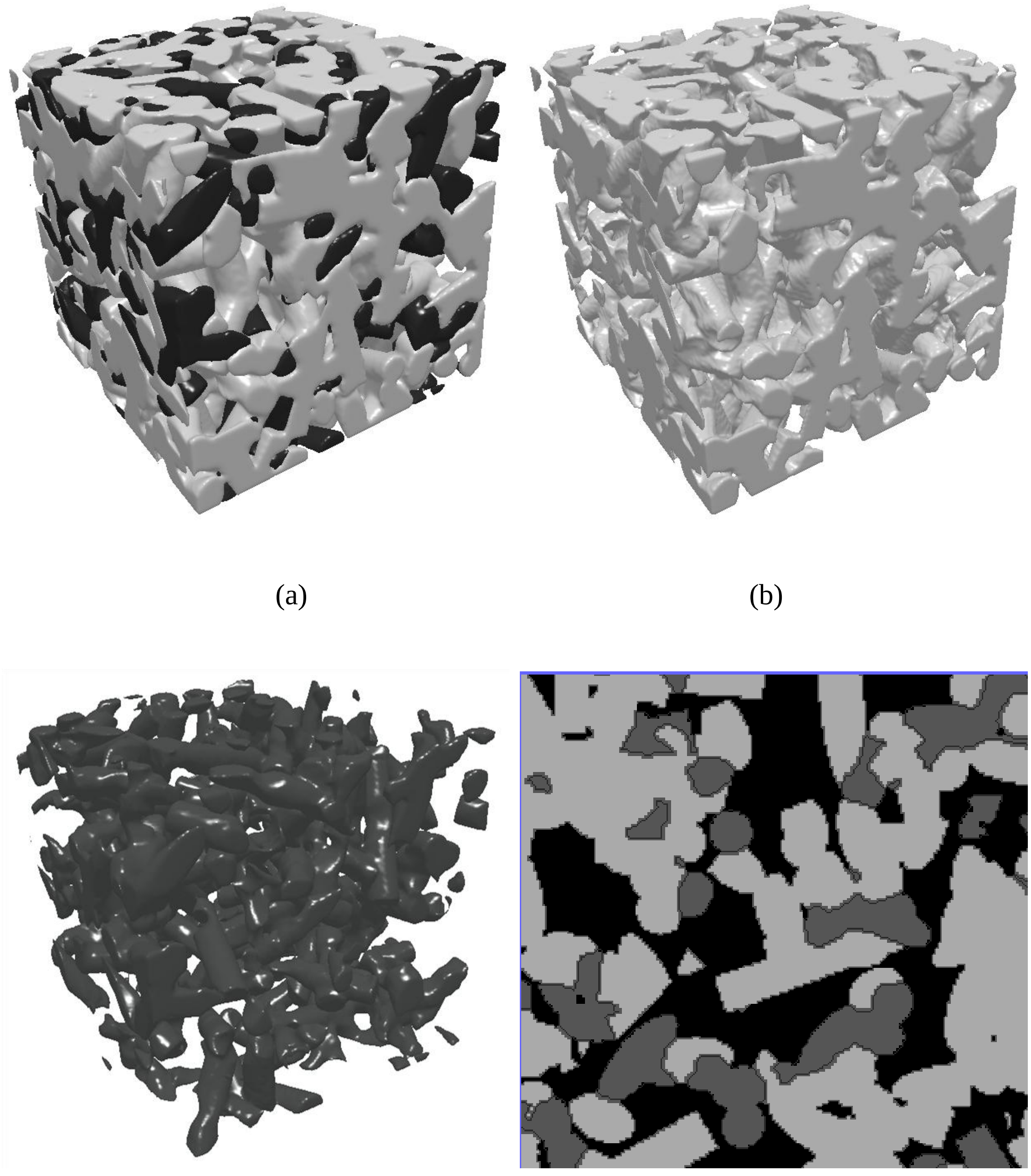

(a) (b)

(c) (d)

Figure 24 A segment of a simulation microstructure of a composite electrode with 27%vol porosity, 51%vol electronic conductor and 22%vol ionic conductor and needle-shaped particles (L/R=9) of equal size. (a) is the surface rendering of the 3D simulation;(b) and (c) are the surface renderings of the electronic and ionic conductor, respectively;(d) is a cross-section in (a).

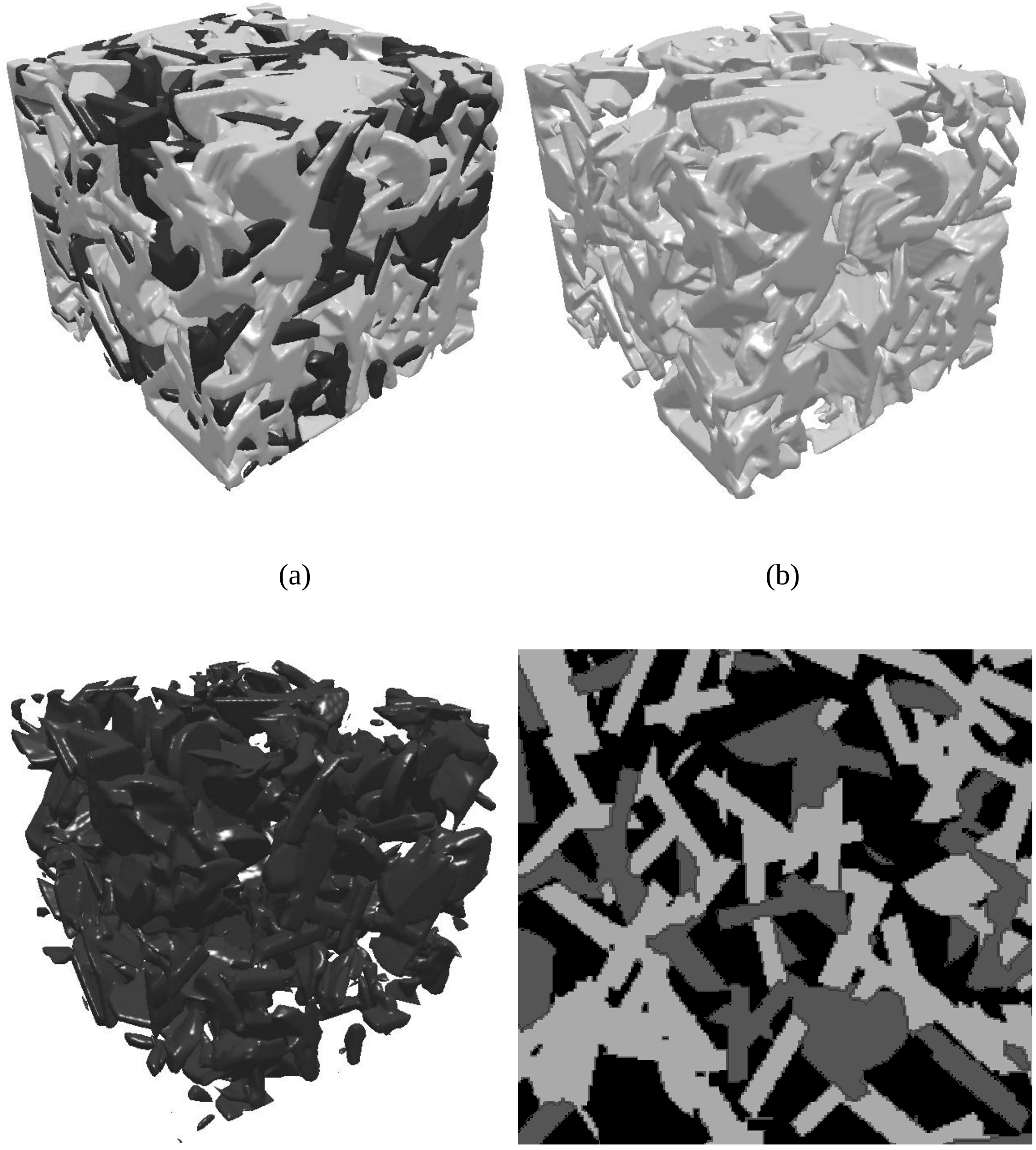

(a) (b)

(c) (d)

Figure 25 A segment of a simulation microstructure of a composite electrode with 27%vol porosity, 51%vol electronic conductor and 22%vol ionic conductor and flake-shaped particles (L/R=1/3) of equal size. (a) is the surface rendering of the 3D simulation;(b) and (c) are the surface renderings of the electronic and ionic conductor, respectively;(d) is a cross-section in (a).

CHAPTER 6

TOPOLOGICAL CONNECTIVITY OF TRIPLE-PHASE BOUNDARIES

Analytical microstructure model presented in chapter 4 yields an expression for total triple phase boundary length per unit volume L_{TPB}. The model is validated via comparisons with the experimental data reported in chapter 3 and microstructure simulations given in chapter 5. Nevertheless, the total triple phase boundary length L_{TPB} computed from the analytical model includes the triple phase boundaries that are topologically connected to the electrolyte and the external circuit at the two opposite faces of the electrode as well as isolated triple phase boundaries that are not topologically connected to the electrolyte and the external circuit. To be a potential site for the electrochemical fuel cell reactions, a triple phase boundary segment must be a part of the electrical conducting path, and therefore, must be topologically connected to the electrolyte, the external circuit and source of oxygen or fuel[11]. Therefore, it is of interest to determine what percentage of total triple phase boundary length is topologically connected and how that percentage varies with the volume fractions of the constituent phases, mean particles sizes, and other relevant geometric attributes. In this chapter, computer simulated 3D microstructures based on the algorithms described in the previous chapter are utilized to address these issues. The simulations reveal that at least 80% of

---

[11] It is important to note that although not all active TPB is of equal catalytic activity in actual SOFC operation. Theoretic studies [19] on the LSM-YSZ composite cathode has shown that a region close to the electrolyte contributes to the majority of the cathodic current while the remaining cathode is less active, which is due to the limited ionic conductivity of porous YSZ. Therefore, this chapter focuses on the active TPB in an electrode of a limited and realistic thickness.

total triple phase boundary length (L_{TPB}) given by Eqn. (4.34) in chapter 4 is topologically connected when all three phases topologically percolate, which is essential for the fuel cell to function. Therefore, in the composition regime of interest in the fuel cell electrode applications the L_{TPB} given by the analytical model can be approximated as the total topologically connected triple phase boundary length. The procedure for calculation of topologically connected triple phase boundary length is briefly described in the next section and that is followed by a detailed parametric analysis.

6.1 Simulation Study of the Topologically Connectivity

Microstructure simulations reported in the previous chapter are utilized for the present analysis. To facilitate computation of the topologically connected triple phase boundary length a layer of current collector (representing the external electrical circuit connection) and electrolyte are attached to the two opposite faces of the simulated microstructure volume segment as illustrated in Figure 26. The connectivity of a given pixel/voxel belonging to a triple phase boundary is then determined by using well-known digital image analysis procedure called connected component labeling [89] using the C++ computer code given in Appendix A.5, and total topologically connected triple phase boundary length per unit length is estimated by using the stereological procedure described in section 2.5.3. These calculations were performed on a numerous simulated microstructures having different volume fractions of electrolyte, electronic conductor, and porosity phases, and different mean sizes, size distributions, and morphologies of the electrolyte and electronic conductor particle populations. The results of this detailed parametric study are given as follows.

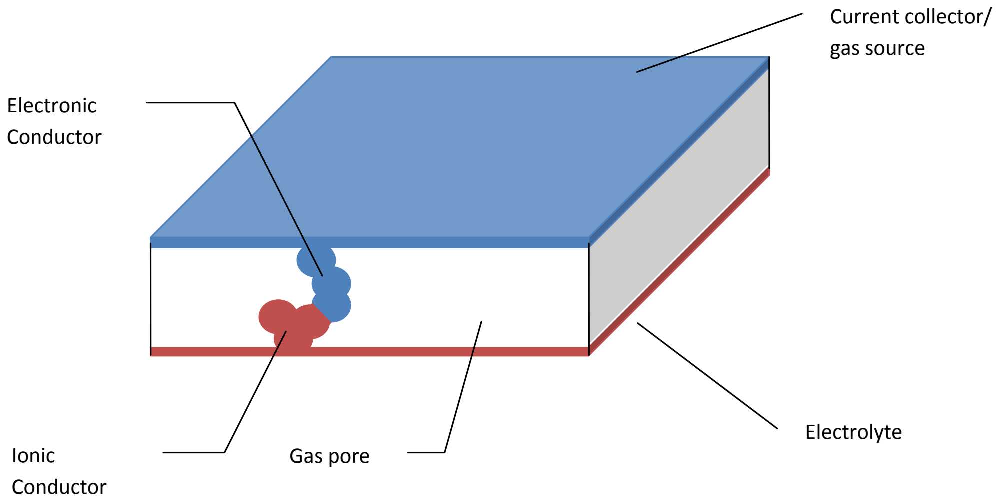

Figure 26 Schematic of the simulated composite electrode for the quantification of active TPB. The gas phase is transferred from the same side of the current collector as in a typical planar SOFC. The ionic conductor phase is labeled "connected" iif it has at least one path to the electrolyte layer; the electronic conductor and the gas pores are labeled "connected" iif they have at least one path to the current collector/gas source layer.

6.2 Results

6.2.1 Effect of Composition and Porosity

A series of 100 microstructures with different compositions have been simulated and analyzed for connectivity of TPB. For each composition 8 realizations were generated so that the effect of randomness can be eliminated. In this parametric study the particle sizes of the ionic conductor and the electronic conductor are identical and the particles are spherical. The size of the simulated microstructure is equal to 20 times the particle radius, which makes the volume for connectivity analysis 18 times the particle radius after cropping to eliminate edge effect.

6.2.1.1 Effects of Volume Fractions of Ionic conductor and Electronic conductor

The effects of volume fractions of ionic conductor and electronic conductor are determined by studying how the percentage of connected TPB varies with composition when porosity, particle size and morphology are constant. Figure 27 is a plot of the percentage of connected TPB in simulations with the porosity level of 27%. Obviously the highest TPB connectivity is achieved with equal volume fractions (36.5%) of the electronic and ionic conductor. Since the porosity volume fraction is constant, the variation of the connected TPB can be attributed to the change of volume fractions of the electronic or ionic conductor. When the volume fraction of ionic conductor is below 36.5%, the connected TPB increases with increasing volume fraction of the ionic conductor, which is due to the percolation of the ionic conductor; when the volume fraction is above 36.5%, the connectivity of TPB decrease, which reflects the percolation of the electronic conductor. The connectivity of TPB increases rapidly when the volume fraction increases above 17%, where the ionic conductor begins to percolate. The rapid increase of connectivity of TPB is accompanied by large standard errors due to the sensitivity of connectivity of TPB to the local fluctuations of volume fractions of the ionic conductor. After the volume fraction increases to 30%, the connectivity of TPB saturates. Depending on the definition of percolation threshold, the percolation threshold of the ionic conductor is between 20% and 30% when the porosity volume fraction is 27%.

In addition to the microstructure simulations with 27% porosity volume fraction, simulations with other porosity volume fractions are performed (see Figure 28 and Figure 29). Comparison of Figure 27, Figure 28 and Figure 29 reveals that that the percolation threshold of the ionic conductor decreases with deceasing porosity. Percolation thresholds decrease from 30% (27% porosity) to 23% (10% porosity) for the ionic conductor.

The discussion on the effect of volume fractions of the ionic conductor is also applicable to the electronic conductor, since the particle sizes of the two component phases are equal.

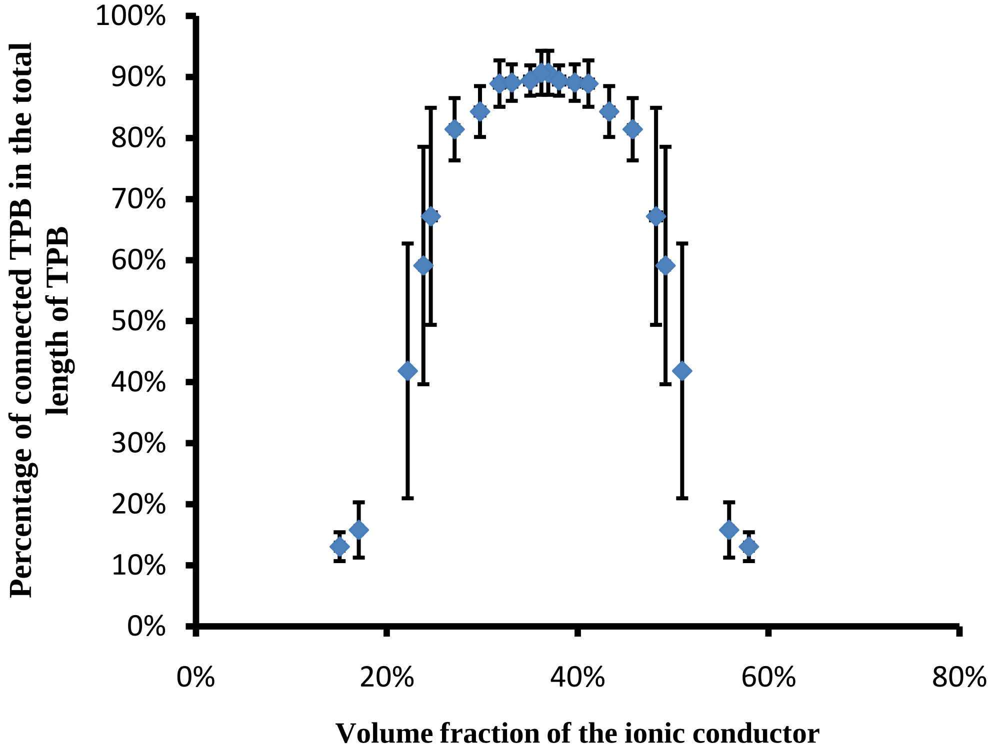

Figure 27 The variation of connected TPB with volume fraction of the ionic conductor when the porosity volume fraction is 27%.

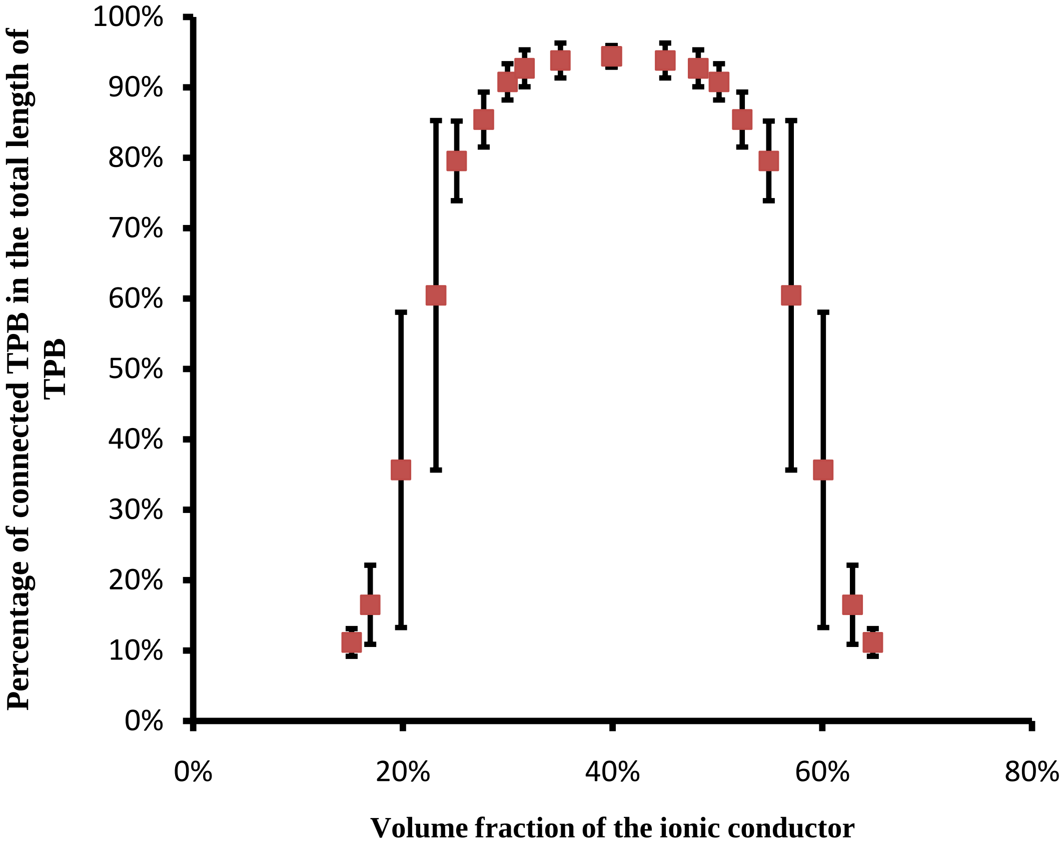

Figure 28 The variation of connected TPB with volume fraction of the ionic conductor when the porosity volume fraction is 20%.

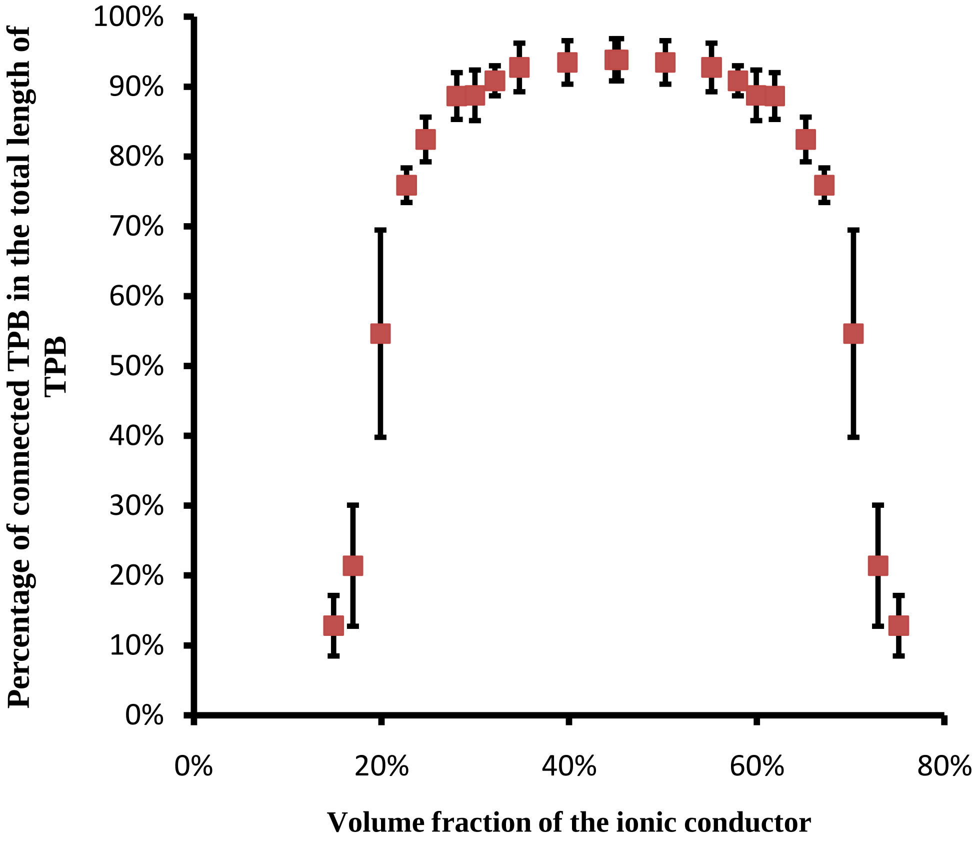

Figure 29 The variation of connected TPB with volume fraction of the ionic conductor when the porosity volume fraction is 20%.

6.2.1.2 The Effect of Porosity Volume Fraction

The effect of the volume fraction of porosity is determined by studying how the percentage of topologically connected TPB varies with porosity when volume fractions of ionic conductor and electronic conductor are equal. Figure 30 is a plot of the percentage of connected TPB in simulations with equal volume fraction of the ionic and electronic conductor. In contrary to Figure 27, Figure 28 and Figure 29 , the curve in Figure 30 is not symmetric around any porosity volume fractions, which indicates that the percolation characteristic of the porosity is different from that of the ionic or electronic conductor. The percolation threshold of porosity is 5%-10%. Such percolation threshold is significantly lower than that of the ionic conductor and electronic conductor (22%-32%). At this point a reasonable hypothesis on the cause of the difference in percolation characteristic is that the morphology of the pores is different from that of the solid components. This hypothesis is supported by a parametric study on the effect of particle morphologies in section 6.2.3. When the porosity volume fraction is in the range of 10-30%, the percentage of connected TPB does not change significantly and it is above 80%. As the porosity get higher than 35%, the connected TPB decreases steadily because the remaining volume fraction for the solid components is lowered towards the percolation threshold. Furthermore, the percolation threshold itself is increased as the porosity volume fraction increases, as was discussed previously.

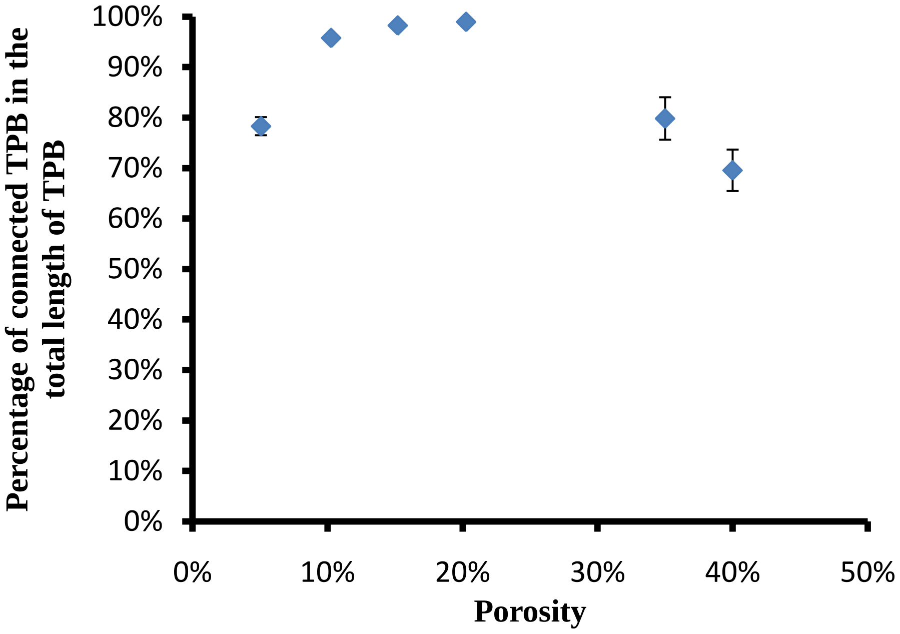

Figure 30 The variation of TPB connectivity with porosity volume fractions when the volume fractions of ionic conductor and electronic conductor are equal.

Finally, the combined effect of volume fractions of ionic conductor, electronic conductor and porosity is presented in a ternary contour plot (Figure 31), with the position of each point specifying the composition and the color representing the percentage of connect TPB in the total TPB. The contour plot shows that a percentage of connected TPB of higher than 80% is achievable when the porosity is below 35%. Recall that the optimal porosity to maximize the *total length* of TPB is determined to be 13.5% (see section 4.2.3) and a higher porosity reduces the length of TPB. Combining these factors, it is desirable to keep the porosity volume fraction between 13.5 -35% and a lower porosity volume fraction increases the length of topologically connected TPB.

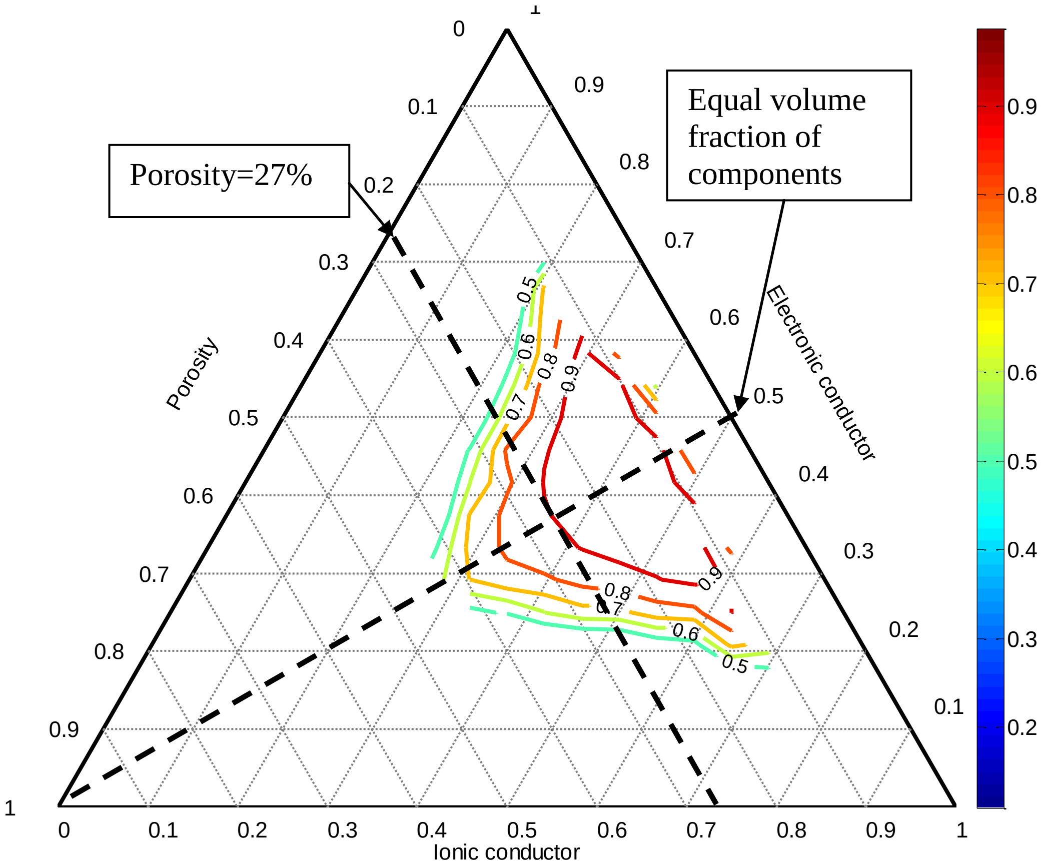

Figure 31 Ternary contour plot of the fraction of the length of connected TPB in the length of total TPB. Particles of the two components are of the same size and spherical shaped. The thickness of the electrodes is 18 times the particle radius.

6.2.2 Effect of Particle Sizes

In the previous section the effect of composition and porosity is investigated with simulated microstructures composed of spherical particle of the same size. In reality the powder sizes of the two components in the composite electrode may be significant different and such difference may affect the connected TPB. In this parametric study, 5 different particle size ratios (PSR) are used for microstructure simulations of different compositions. A porosity volume fraction of 27% is shared by all simulations. The thicknesses of the electrodes are chosen in such a way that the normalized thickness with respect to the particle size of the component with the smaller volume fraction is contant for all simulations. This configuration is to eliminate the effect of thickness of the composite electrode. Figure 32 is plot that compares the change of connected TPB with volume fractions in simulations with different PSRs. Several observations can be made on the plot. First of all, the percolation thresholds are different for different PSR, but all of them fall in the range of 20% - 30%. Secondly, there is no simple correlation between PSR and the corresponding percolation threshold. Last but not least, for all PSR the maximum percentage of connected TPB is almost the same (85% - 90%). With these observations, the PSR does not affect the percentage of connected TPB substantially.

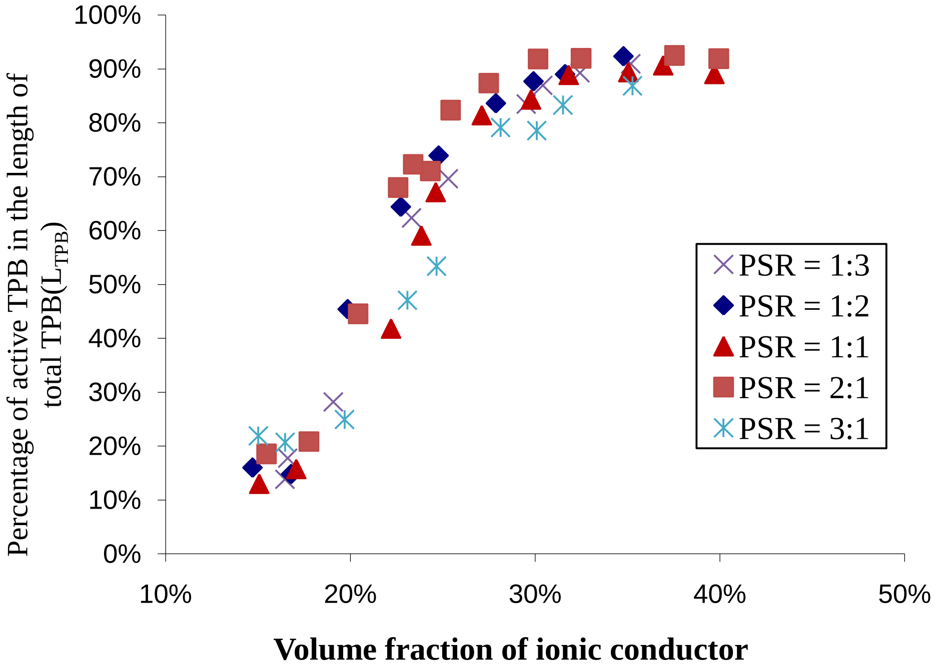

Figure 32 Dependence of the connectivity of TPB on particle size ratios

6.2.3 Effect of particle morphology

In previous studies the particles are assumed to be sphere; however, real particles seldom take a spherical shape, although the particles are sometime described as equiaxed as opposed to whiskers and flakes. The particle morphology not only affects the total length of TPB (L_{TPB}) as discussed in section 4.2.6, but also has substantial effects on the connectivity of TPB. To study the effect of particle morphologies, three series of simulations were performed using cylindrical particles of different height-radius ratios (L/R =9,5 and 1/3), representing needle-shaped (whisker) and plate-shaped (flake) particles, respectively. Like the previous studies, the percentage of connected TPB is plotted against the volume fraction of the connectivity-limiting component (e.g. ionic conductor) (Figure 33). In the plot all three simulations achieves over 80% connected TPB when the volume fraction is above 20%, which makes the percolation threshold volume fraction 10-20%. Recall in the previous study the percolation thresholds were determined to be 20-30%. We can therefore conclude that any non-spherical convex-shaped particle morphology will reduce the corresponding percolation threshold and increase topological connectivity TPB. This also implies that the previous discussions on the fractions of connected TPB give the *lower bound* of the actual connectivity, since the spherical particle morphology leads to the lowest TPB connectivity.

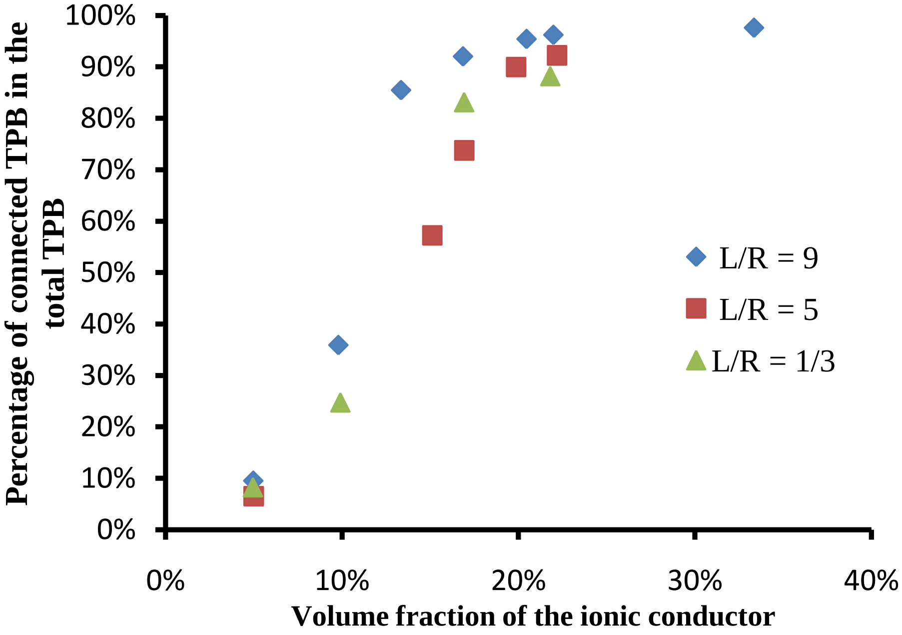

Figure 33 The percentage of connected TPB in electrode with cylindrical particles of different height-radius ratios (L/R)

The effect of particle morphology also helps to explain the low percolation threshold of pore (see section 6.2.1). While the particles in the previous are spheres, the porosity do not exhibit a spherical morphology. Actually as the pore volume fraction decreases, the porosity tends to form thin-walled networks. The current study shows that flake shaped particles tend to reduce the percolation threshold and this finding is consistent with the low percolation threshold of porosity.

6.3 Conclusion

In this chapter the connectivity of TPB in the analytical model in chapter 4 is quantitatively addressed with microstructure simulation using the algorithm in chapter 5, connected component labeling and stereology. By analyzing the quantification results of the fraction of connected TPB in the total TPB, a domain of process parameters is determined in most of the TPB is active. The effects of process parameters on the TPB connectivity are addressed individually by parametric studies using quantification of simulations.

- The particle size ratio does not affect the connectivity of TPB in any significant way, when the normalized electrode thickness is fixed.
- When the porosity volume fraction is between 10-30%, over 80% of the TPB is topologically connected if the volume fractions of the ionic conductor and electronic conductor are above their corresponding percolation thresholds. The percolation threshold of ionic and electronic conductor is around 20-30% when the porosity is 27%.
- Any non-spherical particle morphology improves the connectivity of TPB, or reduces the percolation threshold. It implies that the previous studies on the quantification of connect TPB give the *lower bound* of the actual connectivity, as real particles are seldom spheres though they are often equiaxed.

The conclusion can also be applied to real microstructure because the TPB length experimentally measured in chapter 3 are also total length of TPB instead of connected TPB. Actually, it requires a *complete* 3D reconstruction of an electrode to determine the length of connected TPB in an unbiased way. To the knowledge of the author only reconstruction of a small segment of the composite electrode is reported in literature [54], which leaves the connectivity of a substantial fraction of the TPB site undecided due to the unknown volume outside the reconstruction. Therefore it is important to realize that the *observed* TPB length in a composite electrode may not be electrochemically active and thus irrelevant to the cell performance. The connectivity analysis in this chapter may provide a crude yet justified correction to the experimentally measured length of TPB.

CHAPTER 7

SUMMARY AND CONCLUSIONS

This dissertation research involved experimental work on quantitative characterization of 3D microstructures of three different SOFC porous composite electrode materials; development of an analytical microstructure model for prediction of total triple phase boundary length per unit volume in 3D isotropic uniform random microstructures of porous composite electrodes for SOFCs; and computer simulations of 3D microstructures of the composite electrodes to validate the analytical model and to study the topological connectivity of the triple phase boundaries. The experimental work has led to development of atomic force microscopy and digital image processing based technique for simultaneous observations of the three phases and the triple phase boundaries in the porous composite cathode microstructures containing YSZ, LSM, and porosity phases. The parametric analyses based on the analytical microstructure model and computer simulations lead to the following conclusions that provide useful input for microstructural engineering of SOFC electrode materials for optimization of performance.

- Computer simulation of 3D microstructures show that in the composition regime of interest for SOFC electrode applications where all three phases must percolate, 80% or more geometric triple phase boundary length (i.e., L_{TPB} predicted by the analytical model) is topologically connected, and therefore, can be potentially active for electrochemical fuel cell reactions.
- For electrolyte and electronic conductor volume fractions in the regime of interest for SOFC electrode applications where all three phases must percolate, the relative

proportion of electrolyte and electronic conductor in the porous composite electrode does not significantly affect total length and the topological connectivity of the triple phase boundaries.

- For given relative proportion of electrolyte and electronic conductor phases, and given mean sizes, CV, and skewness of electrolyte and electronic conductor particle size distributions in the powder mix, the highest total length and topological connectivity of the triple phase boundaries are obtained at the *lowest* value of the porosity volume fraction that yields sufficient percolation and connectivity of pores for fuel/oxidant flow.

- For given relative proportion of electrolyte and electronic conductor phases, porosity volume fraction, and given mean sizes, CV, and skewness of electrolyte and electronic conductor particle size distributions in the powder mix, total triple phase boundary length and topological connectivity are the lowest when the electrolyte and electronic conductor particles have spherical shape, and they can be substantially increased by using flake-like, plate-like, or needle-like morphologies of electrolyte and electronic conductor particles.

- Total triple phase boundary length is inversely proportional to the product of the mean sizes of the electrolyte and electronic conductor particles. Therefore, a decrease in the mean size of electrolyte particles or electronic conductor particles, or both increases the total triple phase boundary length. Nonetheless, the topological connectivity of the triple phase boundaries is not significantly affected by the variations in the mean particle sizes of electrolyte and electronic conductor particles.

- Mono-size electrolyte and electronic conductor particle populations lead to higher total triple phase boundary length as compared to the populations having a distribution of sizes. Size distributions with large spread (high CV) can reduce the total triple phase boundary length by almost an order of magnitude. For a given CV and mean size, size distributions with negative skewness lead to a *higher* value of total triple phase boundary length.

The computer simulations reveal that an increase in the porosity volume fraction increases the percolation thresholds of electrolyte and electronic conductor phases for their topological connectivity.

APPENDIX A

SOURCE CODE

All source code has been compiled in Visual C++ 2008. The source code contained here can be used, copied, modified, merged, published, and/or have copies distributed for academic or research purposes only without restriction under the following conditions:

1. The above header and this permission notice shall be included in all copies or substantial portions of the code.

2. The code is provided "as is", without warranty of any kind, express or implied, including but not limited to the warranties of merchantability, fitness for a particular purpose and non-infringement. In no event shall the author(s) be liable for any claim, damages or liability, whether in an action of contract, tort or otherwise, arising from, out of or in connection with this program.

A.1 Multi-phase Image Boundary Segmentation Boundary Correction

- External dependence: CxImage
- Code:

```
class AFMSegmenter{
public:
      AFMSegmenter(CxImage *rawimg, CxImage *preseg, int level=0);
      CxImage* Segment();  //Return the segmented image preseg;

private:
      int level;
      struct PHASES{
            BYTE phases[3];
            int found;
      } phases;
      enum GRAD{INC,DEC};
```

```
	CxImage *rawimg, *preseg;	//Raw is the raw image, preseg is the
pre-segmented image and the output
	void partition();
	void partitionxy();
	void merge(long region_head,long region_end, long row,BYTE
medium);
	void mergexy(long region_head,long region_end, long row,BYTE
medium);
	GRAD gradient_flag(long i,long j);
	void rotate(CxImage *image);
	BYTE getphases();

};


AFMSegmenter::AFMSegmenter(CxImage *rawimg, CxImage *preseg, int
level/* =0 */):rawimg(rawimg),preseg(preseg),level(level){

}

CxImage* AFMSegmenter::Segment(){
	partition();
	rotate(rawimg);
	rotate(preseg);
	partition();
	rotate(preseg);
	rotate(rawimg);
	//xy direction
	partitionxy();

	preseg->Flip();
	rawimg->Flip();
	partitionxy();

	//preseg->Flip();
	preseg->Mirror();
	return(preseg);
}

//dx and dy are indications of direction of iteration
void AFMSegmenter::partition(){

	long region_head;
	int prev_grad,curr_grad;
	BYTE medium=getphases();
	for(long y=0;y<rawimg->GetHeight();y++){
		prev_grad=gradient_flag(rawimg->GetPixelIndex(0,y),rawimg-
>GetPixelIndex(1,y));

		region_head=0;
		int x;
		for(x=2;x<rawimg->GetWidth();x++){
			curr_grad=gradient_flag(rawimg-
>GetPixelIndex(x,y),rawimg->GetPixelIndex(x-1,y));
			if(curr_grad!=prev_grad){  //insert a new monotonic
region
				merge(region_head,x-1,y,medium);
```

```
                    region_head=x-1;
                    prev_grad=curr_grad;
                }
            }
            merge(region_head,x-1,y,medium);
        }

}

void AFMSegmenter::partitionxy(){
        long region_head;
        int prev_grad,curr_grad;
        BYTE medium=getphases();
        for(long y=0;y<rawimg->GetHeight();y++){
            if(rawimg->IsInside(1,y+1))prev_grad=gradient_flag(rawimg-
>GetPixelIndex(0,y),rawimg->GetPixelIndex(1,y+1));
            region_head=0;
            int xx,yy;
            for(xx=2,yy=y+2;xx<rawimg->GetWidth() && yy<rawimg-
>GetHeight();xx++,yy++){
                curr_grad=gradient_flag(rawimg-
>GetPixelIndex(xx,yy),rawimg->GetPixelIndex(xx-1,yy-1));
                if(curr_grad!=prev_grad){  //insert a new monotonic
region
                    mergexy(region_head,xx-1,y,medium);
                    region_head=xx-1;
                    prev_grad=curr_grad;
                }
            }
            mergexy(region_head,xx-1,y,medium);
        }

}
void AFMSegmenter::merge(long region_head,long region_end,long row,
BYTE medium){
        long dx;
        BYTE phase;
        long phaseend=-1;
        phase=preseg->GetPixelIndex(region_head,row);
        for(dx=region_head+1;dx<=region_end;dx++){
            if(preseg->GetPixelIndex(dx,row)!=phase){

                if(phaseend==-1)phaseend=dx;  //The first time phase
changes
                else if(phase==medium){                         //You
dare change it again!!!
                    //Merge the two ends
                    long left_length=(dx-phaseend)/2;

                    //Merge from the left

                    BYTE leftphase=preseg->GetPixelIndex(phaseend-
1,row);
                    int xx;

                    for(xx=phaseend;xx<phaseend+left_length;xx++){
                        preseg->SetPixelIndex(xx,row,leftphase);
```

```
                }

                phaseend=xx;  //phaseend is set to the new
phase boundary
                //Merge from the right
                BYTE rightphase=preseg->GetPixelIndex(dx,row);
                for(;xx<dx;xx++){  //xx start from
phaseend+left_length, where is the new phase boundary
                    preseg->SetPixelIndex(xx,row,rightphase);
                }
                //phase=rightphase;
            }else{
                phaseend=dx;
            }
            phase=preseg->GetPixelIndex(dx,row);
        }
    }
}

void AFMSegmenter::mergexy(long region_head,long region_end,long
row,BYTE medium){
    long dx,dy;
    BYTE phase;
    long phaseend=-1;
    phase=preseg->GetPixelIndex(region_head,row);
    for(dx=region_head+1,dy=row+region_head+1;dx<=region_end;dx++,dy+
+){
        if(preseg->GetPixelIndex(dx,dy)!=phase){

            if(phaseend==-1)phaseend=dx;  //The first time phase
changes
            else if(phase==medium){                          //You
dare change it again!!!
                //Merge the two ends
                long left_length=(dx-phaseend)/2;

                //Merge from the left

                BYTE leftphase=preseg->GetPixelIndex(phaseend-
1,row+phaseend-1);
                int xx,yy;

    for(xx=phaseend,yy=row+phaseend;xx<phaseend+left_length;xx++,yy++
){
                    preseg->SetPixelIndex(xx,yy,leftphase);
                }

                phaseend=xx;  //phaseend is set to the new
phase boundary
                //Merge from the right
                BYTE rightphase=preseg->GetPixelIndex(dx,dy);
                for(;xx<dx;xx++,yy++){  //xx start from
phaseend+left_length, where is the new phase boundary
                    preseg->SetPixelIndex(xx,yy,rightphase);
                }
                //phase=rightphase;
            }else{
```

```
                        phaseend=dx;
                  }
                  phase=preseg->GetPixelIndex(dx,dy);
            }
      }


}

AFMSegmenter::GRAD AFMSegmenter::gradient_flag(long i,long j){
      long diff=j-i;
      if(diff<-level)return DEC;
      else if(diff>level)return INC;
      else return LVL;
}

void AFMSegmenter::rotate(CxImage *image){

      image->RotateLeft();
}

BYTE AFMSegmenter::getphases(){
      long x,y;
      //phase registering
      phases.phases[0]=-1;
      phases.phases[1]=-1;
      phases.phases[2]=-1;
      phases.found=-1;

      for(x=0;x<preseg->GetWidth();x++)
            for(y=0;y<preseg->GetHeight();y++){
                  BYTE p=preseg->GetPixelIndex(x,y);
                  if(phases.phases[0]!=p && phases.phases[1]!=p &&
phases.phases[2]!=p && phases.found<3){
                        phases.found++;
                        phases.phases[phases.found]=p;
                  }

            }

      //find the medium one
      if((phases.phases[0]-phases.phases[1])*(phases.phases[1]-
phases.phases[2])>0) return phases.phases[1];
      if((phases.phases[1]-phases.phases[2])*(phases.phases[2]-
phases.phases[0])>0) return phases.phases[2];
      if((phases.phases[1]-phases.phases[0])*(phases.phases[0]-
phases.phases[2])>0) return phases.phases[0];

}
```

A.2 Multi-phase color-coded image small object removing

- External dependece: CxImage, connected.h (by Ali Rahimi)
- Code:

```
struct PIXEL{
	int x,y;
	//PIXEL(int x,int y):x(x),y(y){};
};
typedef vector<PIXEL> Component;
struct ComponentEntry{
	Component c;
	bool removed;
};
typedef map<unsigned long,ComponentEntry> ComponentList;

class PebbleRemover
{
public:
	void remove();
	PebbleRemover(CxImage *in, CxImage *out, long size,bool
pitfilling=false);
	virtual ~PebbleRemover();

private:
	void ChangePhase(Component &cp,BYTE phase);
	BYTE InterfaceWinner(Component &cp);

	long extract(long size, unsigned long *buffer,ComponentList
&components);
	bool pitfilling;
	long size;
	CxImage *imgout;
	CxImage *imgin;
};


PebbleRemover::~PebbleRemover()
{

}

PebbleRemover::PebbleRemover(CxImage *in, CxImage *out, long size, bool
pitfilling):imgin(in),imgout(out),size(size),pitfilling(pitfilling)
{

}
#define B(x,y) buffer[(long)x+y*imgin->GetEffWidth()]
void PebbleRemover::remove()
{
	//Connected Component Labelling

	unsigned long *buffer=new unsigned long[imgin-
>GetEffWidth()*imgin->GetHeight()];
```

```
     ConnectedComponents<BYTE, unsigned long, std::equal_to<BYTE>,bool>
cc(20000);

      ComponentList cl;
      cl.clear();
      cc.connected(imgin->GetBits(),buffer,imgin->GetEffWidth(),imgin-
>GetHeight(),std::equal_to<BYTE>(),true);
            ofstream debugfile("debug.txt");
            BYTE *bits=imgin->GetBits();
           //for(int  i=0;i<imgin->GetEffWidth()*imgin->GetHeight();i++)
      debugfile<<(int)bits[i]<<" ";
            cout<<"imgin->GetEffWidth()"<<imgin->GetEffWidth()<<endl;
      int np=extract(size,buffer,cl);
      do{
            cout<<np<<" isolated regions found."<<endl;
            ComponentList::iterator i;
            for(i=cl.begin();i!=cl.end();i++){
                  if(!(i->second.removed)){
                        //Calculate the interface areas, store pixels
and numbers
                        BYTE winner=InterfaceWinner(i->second.c);
                        ChangePhase(i->second.c,winner);

                  }
            }

            cl.clear();


            debugfile.close();

            cout<<"Start component labelling"<<endl;
            cc.connected(imgin->GetBits(),buffer,imgin-
>GetEffWidth(),imgin->GetHeight(),std::equal_to<BYTE>(),true);
            cout<<"Component Labelling finished"<<endl;
      }while((np=extract(size,buffer,cl))!=0 && !pitfilling);


      delete(buffer);
}


long PebbleRemover::extract(long size,unsigned long
*buffer,ComponentList &components)
{
      components.clear();
      PIXEL p;
      long pebblecount=0;
      for(p.x=0;p.x<imgin->GetEffWidth();p.x++)
            for(p.y=0;p.y<imgin->GetHeight();p.y++){
                  unsigned long px=B(p.x,p.y);
                  ComponentList::iterator i;
                  if((i=components.find(px))==components.end()){
                        ComponentEntry c;
                        c.c.clear();
                        c.c.push_back(p);
                        c.removed=false;
```

```
                        components[px]=c;
                        pebblecount++;
                  }else{
                        if(i->second.removed==false){
                              i->second.c.push_back(p);
                              if(i->second.c.size()>size){
                                    i->second.removed=true;
                                    i->second.c.clear();
                                    pebblecount--;
                              }
                        }
                  }
            }
            return pebblecount;
}

BYTE PebbleRemover::InterfaceWinner(Component &cp)
{
      ComponentList interfaces;
      BYTE thisphase=imgin->GetPixelIndex(cp.begin()->x,cp.begin()->y);
//Get the phase of this component from original image

      interfaces.clear();
      Component::iterator i;
      for(i=cp.begin();i!=cp.end();i++){
            //Get all eight neighbours
            PIXEL p;
            for(p.x=i->x-1;p.x<=i->x+1;p.x++){
                  for(p.y=i->y-1;p.y<=i->y+1;p.y++){
                        BYTE phase=imgin->GetPixelIndex(p.x,p.y);
                        if(phase!=thisphase){  // p is an interface
pixel
                              //is p already in interfaces?
                             //first, is p phase present in interfaces?
                              ComponentList::iterator clsi;

      if((clsi=interfaces.find(phase))==interfaces.end()){ //no phase
in interfaces?
                                    //add the first pixel of phase
                                    ComponentEntry ce;
                                    ce.c.clear();
                                    ce.c.push_back(p);
                                    interfaces[phase]=ce;
                              }else{  //phase already has an entry
                                   //is phase already in the interface?
                                    //The naive way
                                    bool found=false;
                                    for(Component::iterator ci=clsi-
>second.c.begin();ci!=clsi->second.c.end();ci++){
                                          if(ci->x==p.x && ci-
>y==p.y){found=true;break;}
                                    }
                                    if(!found)clsi-
>second.c.push_back(p);  //if not found, then add to the interface
                              }

                        }
```

```
			}
		}
	}
	//find the longest interface

	if(!pitfilling){
		long max=0;
		BYTE maxphase;
		for(ComponentList::iterator 
clsi=interfaces.begin();clsi!=interfaces.end();clsi++){
			if(max<=clsi->second.c.size()){
				max=clsi->second.c.size();
				maxphase=clsi->first;
			}
		}
		return maxphase;
	}else{
		//Pit Filling mode: if a particle is surround by phase=150, 
fill it with phase=50
		if(interfaces[50].c.size()==0 || 
(double)interfaces[150].c.size()/interfaces[50].c.size()>4)
		{
			return 50;
		}
		else return thisphase;
	}
}

void PebbleRemover::ChangePhase(Component &cp, BYTE phase)
{
	for(Component::iterator i=cp.begin();i!=cp.end();i++)imgin-
>SetPixelIndex(i->x,i->y,phase);
}
```

A.3 Simulation of Microstructure of Composite Electrodes Using Spherical Particles

- External dependence: CxImage, randomc.h (by A. Fog)
- Code:

  Class Multibool:

```
class MultiBool
{
```

```
public:
     MultiBool(std::string filename,int height, int length, int width);
      ~MultiBool(void);
      void GeneratePoisson(std::vector<int> &nPoints);
      void SphereFill(std::vector<unsigned int> &radius);
private:
      std::vector<Cells> pointsets;
      std::string filename;
      int height,length,width;

private:
      unsigned int find_max_radius(vector<unsigned int> &radius);


};

#define MAX_RADIUS 1e15
MultiBool::MultiBool(std::string filename,int height, int length, int
width):filename(filename),length(length),height(height),width(width)
{

}

MultiBool::~MultiBool(void)
{

}
void MultiBool::GeneratePoisson(std::vector<int> &nPoints){
      using namespace std;
      TRanrotBGenerator random((unsigned)time(NULL));

      //EDIT: Oct 23, 2008
      //Separate the Cells multimap by phase

      unsigned int count=0;
      for(std::vector<int>::iterator
i=nPoints.begin();i!=nPoints.end();i++){
            Cells pointset(*i,width,length,height);
            pointsets.push_back(pointset);
      }

      //Init pointsets

      //pointset=new Cells(count,width,length,height);

      //Generate random sphere center
      for(std::vector<int>::iterator
i=nPoints.begin();i!=nPoints.end();i++){
            for(int j=1;j<=*i;j++){
                  POINTXYZ p;
                  p.x=random.Random()*length+0.5;
                  p.y=random.Random()*width+0.5;
                  p.z=random.Random()*height+0.5;
                  p.phase=(i-nPoints.begin())+1;
                  pointsets[i-nPoints.begin()].RegisterPoint(p);
            }
```

```
      }
}
void MultiBool::SphereFill(std::vector<unsigned int> &radius){

      //unsigned int max_radius=find_max_radius(radius);
      CxImage layer(length,width,8);
      layer.SetGrayPalette();
      for(int z=0;z<height;z++){
            for(int x=0;x<length;x++){
                  for(int y=0;y<width;y++){

                        double
norm_mindist=MAX_RADIUS,mindist,dist,norm_dist;
                        BYTE mindist_phase=0;  //Set to porosity by
default

                        for(vector<Cells>::iterator
i=pointsets.begin();i!=pointsets.end();i++){
                              size_t index=i-pointsets.begin();
                              //Range of the search cube
                              POINTXYZ p_min={x-radius[index],y-
radius[index],z-radius[index],0};
                              POINTXYZ
p_max={x+radius[index],y+radius[index],z+radius[index],0};

                              //cout<<p_min.x<<" "<<p_min.y<<"
"<<p_min.z<<endl;
                              Cells::CellList &cl=i-
>FindPointsInCell(p_min,p_max);

                              mindist=MAX_RADIUS;
                              for(Cells::CellList::iterator
cli=cl.begin();cli!=cl.end();cli++){
                                    PointsMap::iterator pmi=*cli;
                                    unsigned int key=pmi->first;

                                    for(;pmi!=i->GetPointMap().end() &&
pmi->first==key;pmi++){
                                          int dx,dy,dz;
                                          if(abs(dx=pmi->second.x-
x)<=radius[index] && abs(dy=pmi->second.y-y)<=radius[index] &&
abs(dz=pmi->second.z-z)<=radius[index]){
                                                dist=dx*dx+dy*dy+dz*dz;
                                                if(dist<mindist){
                                                      mindist=dist;
                                                }
                                          }
                                    }
                              }
                              delete &cl;

                              //If the normalized nearest neighbour by
far is this phase, change the pixel color assignment
                              if(mindist<radius[index]*radius[index]){

      norm_dist=mindist/radius[index]/radius[index];
                                    if(norm_dist<norm_mindist){
```

```
                                        norm_mindist=norm_dist;
                                        mindist_phase=i-
>GetPointMap().begin()->second.phase;
                                    }
                              }
                        }
                        layer.SetPixelIndex(x,y,mindist_phase);
                  }
            }
            std::ostringstream o;
            o<<z;
            using namespace std;

      layer.Save((filename+"_"+o.str()+".bmp").c_str(),CXIMAGE_FORMAT_B
MP);
            cout<<"Layer "<<z<<" generated"<<endl;

      }
}

unsigned int MultiBool::find_max_radius(vector<unsigned int> &radius){
            unsigned int max_radius=0;
            for(vector<unsigned int>::iterator
i=radius.begin();i!=radius.end();i++){
                  max_radius=(max_radius<*i?*i:max_radius);
            }
            return max_radius;
}
```

Class Cell:

```
struct POINTXYZ{
      int x,y,z;
      int phase;
};
typedef multimap<unsigned int,POINTXYZ> PointsMap;

class Cells
{
public:
      typedef vector<PointsMap::iterator> CellList;
      Cells(const unsigned int n_points, const unsigned int width,
const unsigned int length, const unsigned int height);
      ~Cells(void);
      CellList& FindPointsInCell(const POINTXYZ &min, const POINTXYZ
&max);
      void RegisterPoint(const POINTXYZ &point);
      PointsMap& GetPointMap(){return points;};

private:
      PointsMap points;
      int width, length, height, width_division, length_division,
height_division;
      int width_nd,length_nd,height_nd;

private:
```

```
	void divide_space(unsigned int n_points);
	POINTXYZ find_cell(int x,int y,int z);
	inline unsigned int GetCellID(const POINTXYZ &cell_location);

};




Cells::Cells(const unsigned int n_points, const unsigned int width,
const unsigned int length, const unsigned int height):
width(width),length(length),height(height)
{
	points.clear();
	divide_space(n_points);
	cout<<"Length:"<<length_division<<" "<<length_nd<<endl;
	cout<<"width:"<<width_division<<" "<<width_nd<<endl;
	cout<<"height:"<<height_division<<" "<<height_nd<<endl;

}

void Cells::divide_space(unsigned int n_points){
	unsigned int
trial_number_of_division=(pow((double)n_points/CENTER_DENSITY,0.3333)+0
.5);
	cout<<"Attempted division:"<<trial_number_of_division<<endl;
	length_division=length/trial_number_of_division;
	length_nd=length/length_division+(length % length_division!=0);
	width_division=width/trial_number_of_division;
	width_nd=width/width_division+(width % width_division!=0);
	height_division=height/trial_number_of_division;
	height_nd=height/height_division+(height % height_division!=0);
}

POINTXYZ Cells::find_cell(int x,int y,int z){
	POINTXYZ cell_location;
	cell_location.x=x/length_division;
	cell_location.x=(x<0)?0:cell_location.x;
	cell_location.x=(x>=length)?(length_nd-1):cell_location.x;
	cell_location.y=y/width_division;
	cell_location.y=(y<0)?0:cell_location.y;
	cell_location.y=(y>=width)?(width_nd-1):cell_location.y;
	cell_location.z=z/height_division;
	cell_location.z=(z<0)?0:cell_location.z;
	cell_location.z=(z>=height)?(height_nd-1):cell_location.z;
	return cell_location;

}

Cells::CellList & Cells::FindPointsInCell(const POINTXYZ &min,const
POINTXYZ &max){

	CellList *celllist=new CellList();
	celllist->clear();
	POINTXYZ
&cell_location_min=find_cell(min.x,min.y,min.z),&cell_location_max=find
_cell(max.x,max.y,max.z);
```

```
      POINTXYZ cell_location;
      for(cell_location.x=cell_location_min.x;cell_location.x<=cell_loc
ation_max.x;cell_location.x++){

      for(cell_location.y=cell_location_min.y;cell_location.y<=cell_loc
ation_max.y;cell_location.y++){

      for(cell_location.z=cell_location_min.z;cell_location.z<=cell_loc
ation_max.z;cell_location.z++){
                        PointsMap::iterator i;

      if((i=points.find(GetCellID(cell_location)))!=points.end()){
                              celllist->push_back(i);
                        }
                  }
            }
      }
      return *celllist;
}

unsigned int Cells::GetCellID(const POINTXYZ &cell_location){
      //cout<<"CellIDInquiry:"<<cell_location.z*(length_nd*width_nd)+ce
ll_location.y*length_nd+cell_location.x<<endl;
      return
cell_location.z*(length_nd*width_nd)+cell_location.y*length_nd+cell_loc
ation.x;

}

void Cells::RegisterPoint(const POINTXYZ &point){

      points.insert(pair<unsigned
int,POINTXYZ>(GetCellID(find_cell(point.x,point.y,point.z)),point));
}
Cells::~Cells(void)
{
}
```

A.4 Simulation of Microstructure of Composite Electrodes Using Cylindrical Particles

- External Dependence: CxImage, randomc.h (By A. Fog)
- Code:

<u>Class Multibool:</u>

```
#define MAX_RADIUS 1e15
MultiBool::MultiBool(std::string filename,int height, int length, int
width):filename(filename),length(length),height(height),width(width)
{

}

MultiBool::~MultiBool(void)
{

}
void MultiBool::GeneratePoisson(std::vector<int> &nPoints,bool
seperate,std::vector<unsigned int> &radius){
	using namespace std;
	TRanrotBGenerator random((unsigned)time(NULL));

	//EDIT: Oct 23, 2008
	//Separate the Cells multimap by phase

	unsigned int count=0;
	for(std::vector<int>::iterator
i=nPoints.begin();i!=nPoints.end();i++){
		Cells pointset(*i,width,length,height);
		pointsets.push_back(pointset);
	}

	//Init pointsets

	//Generate random sphere center
	for(std::vector<int>::iterator
i=nPoints.begin();i!=nPoints.end();i++){
		for(int j=1;j<=*i;j++){
			POINTXYZ p;

			p.x=random.Random()*length+0.5;
			p.y=random.Random()*width+0.5;
			p.z=random.Random()*height+0.5;

	rand_rotation(random.Random(),random.Random(),random.Random(),p.r
otationMatrix);
			p.phase=(i-nPoints.begin())+1;

			//EDIT: Dec 19,2008
			//If seperate==true, then test if distance between
centers > max(r1,r2)

			//EDIT: Feb 19,2008
			//New fantom seed treatment:grow, impinge and remove

			//A clever way of adapting the old code: only change
the p.phase and still registering it
			//to its original phase; the color of pixels will
change accordingly.

			if (seperate){
				p.phase=test_seperate(p,i-
nPoints.begin(),radius);
```

```
                  }
                  pointsets[i-nPoints.begin()].RegisterPoint(p);
            }
      }
}
void MultiBool::SphereFill(std::vector<unsigned int>
&radius,vector<ParametricSurface> &surfaces){

      CxImage layer(length,width,8);
      layer.SetGrayPalette();
      for(int z=0;z<height;z++){
            for(int x=0;x<length;x++){
                  for(int y=0;y<width;y++){

                        double mindist=2,dist,normdist;
                        BYTE mindist_phase=0;  //Set to porosity by
default

                        for(vector<Cells>::iterator
i=pointsets.begin();i!=pointsets.end();i++){
                              size_t index=i-pointsets.begin();
                              //Range of the search cube
                              POINTXYZ p_min(x-radius[index],y-
radius[index],z-radius[index]);
                              POINTXYZ
p_max(x+radius[index],y+radius[index],z+radius[index]);

                              Cells::CellList &cl=i-
>FindPointsInCell(p_min,p_max);

                              for(Cells::CellList::iterator
cli=cl.begin();cli!=cl.end();cli++){
                                    PointsMap::iterator pmi=*cli;
                                    unsigned int key=pmi->first;

                                    for(;pmi!=i->GetPointMap().end() &&
pmi->first==key;pmi++){
                                          double dx,dy,dz;

                                          if(fabs(dx=pmi->second.x-
x)<=radius[index] && fabs(dy=pmi->second.y-y)<=radius[index] &&
fabs(dz=pmi->second.z-z)<=radius[index]){
                                                dist=dx*dx+dy*dy+dz*dz;

      normdist=sqrt(dist/surfaces[pmi->second.phase-
1].mapG(dx,dy,dz,pmi->second.rotationMatrix));

                                                if(normdist<1 &&
normdist<mindist){
                                                      mindist=normdist;

                                                      //EDIT:Jan
19,2008
                                                      //The following
line added to implement the "fantom seed" treatment

      mindist_phase=pmi->second.phase;
```

```
                                        }
                                    }
                                }
                            }
                            delete &cl;

                        }
                        layer.SetPixelIndex(x,y,mindist_phase);
                    }
                }
                std::ostringstream o;
                o<<z;
                using namespace std;

            layer.Save((filename+"_"+o.str()+".bmp").c_str(),CXIMAGE_FORMAT_B
MP);
                cout<<"Layer "<<z<<" generated"<<endl;

            }
}

unsigned int MultiBool::find_max_radius(vector<unsigned int> &radius){
                unsigned int max_radius=0;
                for(vector<unsigned int>::iterator
i=radius.begin();i!=radius.end();i++){
                    max_radius=(max_radius<*i?*i:max_radius);
                }
                return max_radius;
}


//test if p satifies that distance > max(r1,r2)
#define MAX(a,b) ((a)>(b)?(a):(b));
unsigned int MultiBool::test_seperate(POINTXYZ &p, unsigned int phase,
std::vector<unsigned int> &radius){
            for(vector<Cells>::iterator
i=pointsets.begin();i!=pointsets.end();i++){
                //Do not test with the same phase
                if(i-pointsets.begin()!=phase){
                    int max_r=abs((int)radius[phase]-(int)radius[i-
pointsets.begin()]);
                    Cells::CellList &l=i->FindPointsInCell(POINTXYZ(p.x-
max_r,p.y-max_r,p.z-max_r),POINTXYZ(p.x+max_r,p.y+max_r,p.z+max_r));
                    for(Cells::CellList::iterator
j=l.begin();j!=l.end();j++){
                        PointsMap::iterator pmi=*j;
                        unsigned int key=pmi->first;
                        for(;pmi!=i->GetPointMap().end() && pmi-
>first==key;pmi++){
                            double dx,dy,dz;
                            if(abs(dx=pmi->second.x-p.x)<=max_r &&
abs(dy=pmi->second.y-p.y)<=max_r && abs(dz=pmi->second.z-p.z)<=max_r){
                                int dist=dx*dx+dy*dy+dz*dz;
                                if(dist<max_r*max_r){
                                    return pmi->second.phase;
                                }
```

```
                              }
                        }
                  }
            }
      }
      return phase+1;
}

//Code by J. Arvo
void MultiBool::rand_rotation(double x0,double x1,double x2,double 
rotationMatrix[3][3]){
    float theta = x0 * PI*2; /* Rotation about the pole (Z).      */
    float phi   = x1 * PI*2; /* For direction of pole deflection. */
    float z     = x2 * 2.0;      /* For magnitude of pole deflection. 
*/

    /* Compute a vector V used for distributing points over the sphere 
*/
    /* via the reflection I - V Transpose(V).  This formulation of V 
*/
    /* will guarantee that if x[1] and x[2] are uniformly distributed, 
*/
    /* the reflected points will be uniform on the sphere.  Note that V 
*/
    /* has length sqrt(2) to eliminate the 2 in the Householder matrix. 
*/

    float r  = sqrt( z );
    float Vx = sin( phi ) * r;
    float Vy = cos( phi ) * r;
    float Vz = sqrt( 2.0 - z );

    /* Compute the row vector S = Transpose(V) * R, where R is a simple 
*/
    /* rotation by theta about the z-axis.  No need to compute Sz since 
*/
    /* it's just Vz.                                                    
*/

    float st = sin( theta );
    float ct = cos( theta );
    float Sx = Vx * ct - Vy * st;
    float Sy = Vx * st + Vy * ct;

    /* Construct the rotation matrix  ( V Transpose(V) - I ) R, which 
*/
    /* is equivalent to V S - R.                                        
*/

    rotationMatrix[0][0] = Vx * Sx - ct;
    rotationMatrix[0][1] = Vx * Sy - st;
    rotationMatrix[0][2] = Vx * Vz;

    rotationMatrix[1][0] = Vy * Sx + st;
    rotationMatrix[1][1] = Vy * Sy - ct;
    rotationMatrix[1][2] = Vy * Vz;
```

```
    rotationMatrix[2][0] = Vz * Sx;
    rotationMatrix[2][1] = Vz * Sy;
    rotationMatrix[2][2] = 1.0 - z;   /* This equals Vz * Vz - 1.0 */
}
```

Class ParametricSurface:

```
typedef map<double,map<double,double>> Gmap;

class ParametricSurface
{
public:
      //ParametricSurface(Gmap &gmap);
      ParametricSurface(double a, double b, double c);
      ~ParametricSurface(void);
      double mapG(double x,double y,double z,double
rotationMatrix[3][3]);
private:
      //Gmap &gmap;
      double a,b,c;
private:
      void rotation(double *x,double *y,double *z,double
rotationMatrix[3][3]);
};


double ParametricSurface::mapG(double x,double y,double z,double
rotationMatrix[3][3]){
      rotation(&x,&y,&z,rotationMatrix);
      //calculate the cooresponding theta and phi
      double phi=atan2((double)a*y,(double)b*x);


      double sintheta=(double)z/c/sqrt(x*x/a/a+y*y/b/b+z*z/c/c);
      //sintheta=(fabs(sintheta)>1?1:sintheta);

      double theta=asin(sintheta);

      //if
(_isnan(pow(a*cos(theta)*cos(phi),2)+pow(b*cos(theta)*sin(phi),2)+pow(c
*sin(theta),2)))cout<<x<<" "<<y<<" "<<z<<endl;
      if (fabs(x)<1e-3 && fabs(y)<1e-3 && fabs(x)<1e-3)return 100;
      else
            return
pow(a*cos(theta)*cos(phi),2)+pow(b*cos(theta)*sin(phi),2)+pow(c*sin(the
ta),2);

}
ParametricSurface::~ParametricSurface(void)
{
}

void ParametricSurface::rotation(double *x,double *y,double *z,double
rotationMatrix[3][3]){
```

```
      double
newX=rotationMatrix[0][0]*(*x)+rotationMatrix[0][1]*(*y)+rotationMatrix
[0][2]*(*z);
      double
newY=rotationMatrix[1][0]*(*x)+rotationMatrix[1][1]*(*y)+rotationMatrix
[1][2]*(*z);
      double
newZ=rotationMatrix[2][0]*(*x)+rotationMatrix[2][1]*(*y)+rotationMatrix
[2][2]*(*z);
      *x=newX;
      *y=newY;
      *z=newZ;
}
```

Class Cell: see A.3

A.5 Measuring Length of Topologically Connected Triple Phase Boundaries

- External Dependence: K3DConnectedComponentLabeler
- Code

```
struct POINTXYZ{
      int x;
      int y;
      int z;
      POINTXYZ(int x=0,int y=0,int z=0):x(x),y(y),z(z){};
};
class ActiveTPBCouter
{
public:
     ActiveTPBCouter(string &listfile,string &keyfile,ostream &result);

      ~ActiveTPBCouter(void);
      double MeasureTPB();
      double MeasureActiveTPB();
      list<POINTXYZ>& GetTPB();
      void SaveVolume(std::string &filepath,DWORD platecolor,DWORD
*volume);
private:
      BYTE *volume;
      int width,length,height;
      list<POINTXYZ> TPBPoints;
```

```
	//Image key
	int solid1,solid2;
	int gas;

private:

	void load_images(string &listfile,string &keyfile);
	void preprocess_volume(BYTE phase); //add a one-pixel shell to 
the volume
	void CheckPercolation(BYTE phase);
	void IdentifyTPB();
	ostream &result;

};


ActiveTPBCouter::ActiveTPBCouter(string &listfile,string 

&keyfile,ostream &result):result(result)


{
	volume=NULL;
	load_images(listfile,keyfile);

}

ActiveTPBCouter::~ActiveTPBCouter(void)
{
	if(volume)delete[] volume;
}

#define V(x,y,z) (z)*length*width+(y)*length+(x)
void ActiveTPBCouter::preprocess_volume(BYTE phase){
	long indexer=0;
	BYTE color;


	//fill the bottom layer with color of phase
	if(phase!=solid2)color=phase;else color=(phase+1)%255;
	for(int x=0;x<length;x++)
		for(int y=0;y<width;y++){
			volume[indexer]=phase;
			indexer++;
		}

	//fill the bottom layer with color of phase
	if(phase==solid2)color=phase;else color=(phase+1)%255;
	indexer=V(0,0,height-1);


	for(int x=0;x<length;x++)
		for(int y=0;y<width;y++){
			volume[indexer]=phase;
			indexer++;
		}
```

```
}
void ActiveTPBCouter::load_images(string &listfile,string &keyfile){

      //load image key
      ifstream imagekey(keyfile.c_str());
      imagekey>>(int)(solid1);
      imagekey>>(int)solid2;
      imagekey>>(int)gas;
      imagekey.close();

      //load image set
      //!!Caution: Large memory allocation!!
            //load image file list
      ifstream imagelist(listfile.c_str());

      string path=listfile.substr(0,listfile.find_last_of('\\')+1);


      vector<string> filenames;
      while(!imagelist.eof()){
            string filename;
            getline(imagelist,filename);
            if(filename!="")filenames.push_back(filename);
      }



      //load first layer
      CxImage layer((path+filenames[0]).c_str(),CXIMAGE_FORMAT_BMP);

      height=filenames.size()+2;
      length=layer.GetWidth();
      width=layer.GetHeight();

      volume=new BYTE[(unsigned)height*length*width];


      unsigned index=length*width; //start from the second bottom layer

      for(int z=1;z<=filenames.size();z++){
            for(int y=0;y<width;y++){
                  for(int x=0;x<length;x++){
                        volume[index]=layer.GetPixelIndex(x,y);
                        index++;
                  }
            }
            if(z<filenames.size()){

      layer.Load((path+filenames[z]).c_str(),CXIMAGE_FORMAT_BMP);
                  cout<<path+filenames[z].c_str()<<endl;
            }
      }


      imagelist.close();
```

```
}
#define VV(x,y) origin[y*length+x]
void ActiveTPBCouter::IdentifyTPB(){
      TPBPoints.clear();

      for(int z=1;z<height-1;z++){
            BYTE *origin=volume+z*length*width;
            for(int x=0;x<length-1;x++){
                  for(int y=0;y<width-1;y++){
                        BYTE p11=VV(x,y);
                        BYTE p12=VV((x+1),y);
                        BYTE p21=VV(x,(y+1));
                        BYTE p22=VV((x+1),(y+1));
                  //four possibilities
                        // p11 p12
                        // p21 p22
                        if( (p11!=p12 && p11!=p21 && p21!=p12) ||
                              (p11!=p12 && p11!=p22 && p12!=p22) ||
                              (p11!=p21 && p11!=p22 && p21!=p22) ||
                              (p21!=p12 && p21!=p22 && p12!=p22)
                              ){

      TPBPoints.push_back(POINTXYZ(x,y,z));
                        }
                  }
            }
      }

}



//#define TV(x,y,z) volume[(z)*length*width+(y)*length+(x)]
#define TLV(x,y,z) labeled_volume[(z)*length*width+(y)*length+(x)]
void ActiveTPBCouter::CheckPercolation(BYTE phase){

      //preprocess volume: add bottom and top layer
      preprocess_volume(phase);

      //Do connected component labelling
      //!!Caution:Large Memory allocation!!
      //!!Caution:Expecting excessive length of time!!

      K3DConnectedComponentLabeler labeler;
      labeler.SetMask(volume,length,width,height,phase);
      labeler.Process();
      DWORD *labeled_volume=labeler.GetOutput();



      //Eliminate TPB points neighbouring isolated phases
      DWORD plate_color=(phase==solid2?TLV(0,0,height-
1):labeled_volume[0]);
      cout<<"Plate_color:"<<plate_color<<endl;
```

```
      list<POINTXYZ>::iterator i=TPBPoints.begin();
      while(i!=TPBPoints.end()){
            //check (x+-1,y+-1,z) (4 points)
            DWORD color;
            bool isolated=true;
            if((color=TLV(i->x,i->y,i-
>z))!=0&&color==plate_color)isolated=false;
            else if((color=TLV(i->x+1,i->y,i-
>z))!=0&&color==plate_color)isolated=false;
            else if((color=TLV(i->x,i->y+1,i-
>z))!=0&&color==plate_color)isolated=false;
            else if((color=TLV(i->x+1,i->y+1,i-
>z))!=0&&color==plate_color)isolated=false;


            if(isolated){
                  i=TPBPoints.erase(i);
            }else{
                  if(i!=TPBPoints.end())i++;
            }

      }
      //Clean up...
      labeler.unSetMask();
      labeler.Clear();
}

void ActiveTPBCouter::SaveVolume(std::string &filepath,DWORD
platecolor,DWORD *volume){
CxImage image(length,width,8);
image.SetGrayPalette();
      for(int z=0;z<height;z++){
            long indexer=0;
            for(int y=0;y<width;y++){
                  for(int x=0;x<length;x++){
                        image.SetPixelIndex(x,y,volume[indexer]);
                        indexer++;
                  }
            }
            char filename[255];
            sprintf(filename,"%s\\%d.bmp",filepath.c_str(),z);
            image.Save(filename,CXIMAGE_FORMAT_BMP);
      }
}
double ActiveTPBCouter::MeasureTPB(){
      IdentifyTPB();
      return (double)TPBPoints.size()/length/width/(height-2)*2;
}

double ActiveTPBCouter::MeasureActiveTPB(){
      cout<<"solid1:"<<(int)solid1<<endl;
      cout<<"solid2:"<<(int)solid2<<endl;
      cout<<"gas:"<<(int)gas<<endl;
      cout<<"Checking gas percolation..."<<endl;
      CheckPercolation(gas);
```

```
      result<<"After checking pore
percolation:"<<(double)TPBPoints.size()/length/width/(height-2)*2<<endl;
      cout<<"Checking solid1 percolation..."<<endl;
      CheckPercolation(solid1);
      result<<"After checking solid1
percolation:"<<(double)TPBPoints.size()/length/width/(height-2)*2<<endl;
      cout<<"Checking solid2 percolation..."<<endl;
      CheckPercolation(solid2);
      return (double)TPBPoints.size()/length/width/(height-2)*2;
}

list<POINTXYZ>& ActiveTPBCouter::GetTPB(){
      return TPBPoints;
}
```

A.6 Measuring Triple Phase Boundary Length

- External Dependence: CxImage

- Code:

```
double measureTPB(CxImage *image,bool save,CString &path){
      long tpb=0;
      CString TPBfile;
      TPBfile=path+CString("tpb.bmp");
      CxImage *TPBimage;
      if(save){
            TPBimage=new CxImage(image->GetWidth(),image-
>GetHeight(),1);
            TPBimage->SetGrayPalette();
      }
      for(unsigned long x=0;x<image->GetWidth()-1;x++)
            for(unsigned long y=0;y<image->GetHeight()-1;y++){
                  BYTE p11=image->GetPixelIndex(x,y);
                  BYTE p12=image->GetPixelIndex(x+1,y);
                  BYTE p21=image->GetPixelIndex(x,y+1);
                  BYTE p22=image->GetPixelIndex(x+1,y+1);
            //four possibilities
                  // p11 p12
                  // p21 p22
                  if( (p11!=p12 && p11!=p21 && p21!=p12) ||
                        (p11!=p12 && p11!=p22 && p12!=p22) ||
                        (p11!=p21 && p11!=p22 && p21!=p22) ||
                        (p21!=p12 && p21!=p22 && p12!=p22)
                        ){
                              tpb++;
                              if(save){
                                    TPBimage->SetPixelIndex(x,y,1);
```

```
                                    }
                              }
                  }


            if(save){
                  TPBimage->Save(TPBfile,CXIMAGE_FORMAT_BMP);
                  delete(TPBimage);
            }
            return (double)2*tpb/image->GetWidth()/image->GetHeight();

}
```

A.7 Measuring Surface Areas and Volume Fractions

- External Dependence: CxImage
- Code:

```
struct InterfaceArea{
      BYTE phase1,phase2; //phase1>phase2
      long count;
      double area;
};

typedef std::map<BYTE,double> VolumeFractions;
typedef std::vector<InterfaceArea>  InterfaceAreas;

class SurfaceAreaLiner
{
public:
      SurfaceAreaLiner(CxImage *img);

      std::pair<InterfaceAreas,VolumeFractions> Measure(InterfaceAreas
*ias=NULL);
private:
      void count(BYTE previouspixel, BYTE currentpixel, InterfaceAreas
*ias);
      CxImage *image;
};



SurfaceAreaLiner::SurfaceAreaLiner(CxImage *img):image(img){};

std::pair<InterfaceAreas,VolumeFractions>
SurfaceAreaLiner::Measure(InterfaceAreas *measured)
```

```
{
	InterfaceAreas *ias;
	if(measured){
		ias=measured;
	}else{
		ias=new InterfaceAreas();
		ias->clear();
	}

	int x,y;
	VolumeFractions vf;
	vf.clear();
	for(x=0;x<image->GetWidth();x++){
		BYTE previouspixel=image->GetPixelIndex(x,0);
		for(y=1;y<image->GetHeight();y++){
			BYTE currentpixel=image->GetPixelIndex(x,y);
			if(currentpixel!=previouspixel){ // an intersection
				count(currentpixel,previouspixel,ias);
			}
			previouspixel=currentpixel;
			vf[currentpixel]+=1;   //Count volume fractions
		}
	}
	for(y=0;y<image->GetHeight();y++){
		BYTE previouspixel=image->GetPixelIndex(0,y);
		for(x=1;x<image->GetWidth();x++){
			BYTE currentpixel=image->GetPixelIndex(x,y);
			if(currentpixel!=previouspixel){ // an intersection
				count(currentpixel,previouspixel,ias);
			}
			previouspixel=currentpixel;
		}
	}

	//Do the division
	VolumeFractions::iterator i;
	for(i=vf.begin();i!=vf.end();i++){
		i->second=i->second/(image->GetWidth()*image->GetHeight());
	}
	return std::pair<InterfaceAreas,VolumeFractions>(*ias,vf);
}

void SurfaceAreaLiner::count(BYTE previouspixel, BYTE currentpixel,
InterfaceAreas *ias){
	BYTE phase1,phase2;
	if(previouspixel>currentpixel){
		phase1=previouspixel;
		phase2=currentpixel;
	}else{
		phase1=currentpixel;
		phase2=previouspixel;
	}

	InterfaceAreas::iterator i;
	bool newinterface=true;
	for(i=ias->begin();i!=ias->end();i++){
		if (i->phase1==phase1 && i->phase2==phase2){
```

```
                    i->count++;
                    newinterface=false;
                    break;
              }
        }

        if(newinterface){
              InterfaceArea ia;
              ia.phase1=phase1;
              ia.phase2=phase2;
              ia.count=1;
              ia.area=2*image->GetWidth()*image->GetHeight();
              ias->push_back(ia);
        }
}
```

A.8 Measuing two-point correlation functions

- External Dependence: CxImage
- Code:

```
class TwoPointCorrelationFunction
{
public:
        TwoPointCorrelationFunction(void);
        typedef pair<BYTE,BYTE> IJ;
        typedef map<IJ,unsigned int> Pij;
        typedef map<unsigned int,Pij> Pijl;
        typedef map<unsigned int,unsigned int> Normalizer;
        void CumulativeMeasure(CxImage &image, Pijl &pijlx,Pijl
&pijly,Normalizer &norm);
        ~TwoPointCorrelationFunction(void);
};


TwoPointCorrelationFunction::TwoPointCorrelationFunction(void)
{
}

TwoPointCorrelationFunction::~TwoPointCorrelationFunction(void)
{
}

void TwoPointCorrelationFunction::CumulativeMeasure(CxImage &image,
Pijl &pijlx,Pijl &pijly,Normalizer &norm){

        long width=image.GetWidth(),height=image.GetHeight();
```

```
	long
lmax=min(width,height)/3,lstep_small=(lmax/800>1?lmax/800:1),lstep_larg
e=lmax/100;  //small step for local, large step for long range;

	for(int
k=0,l=0;l<=lmax;++k,k<50?(l+=lstep_small):(l+=lstep_large)){
		long imax=width-l;  //iteration boundary
		long jmax=height-l;
		long total=imax*jmax;  //total number of pixels
		for(int i=1;i<=imax;i++){
			for(int j=1;j<=jmax;j++){

	pijlx[l][IJ(image.GetPixelIndex(i,j),image.GetPixelIndex(i+l,j))]
++;

	pijly[l][IJ(image.GetPixelIndex(i,j),image.GetPixelIndex(i,j+l))]
++;
				norm[l]++;
			}
		}
	}
}
```

REFERENCES

1. Carrette, L., K.A. Friedrich, and U. Stimming, *Fuel cells: Principles, types, fuels, and applications.* Chemphyschem, 2000. **1**(4): p. 162-193.

2. Steele, B.C.H. and A. Heinzel, *Materials for fuel-cell technologies.* Nature, 2001. **414**(6861): p. 345-352.

3. Ali, A., et al., *Geometrical modeling of microstructure of solid oxide fuel cell composite electrodes.* Journal of Power Sources, 2008. **185**(2): p. 961-966.

4. Sunde, S., *Monte Carlo simulations of polarization resistance of composite electrodes for solid oxide fuel cells.* Journal of The Electrochemical Society, 1996. **143**(6): p. 1930-1939.

5. Arvo, J., ed. *Fast Random Roration Matrices*. Graphics Gems III, ed. D. Kirk. 1992, Academic Press: New York. 117-120.

6. Ormerod, R.M., *Solid oxide fuel cells.* Chemical Society Reviews, 2003. **32**(1): p. 17-28.

7. Fleig, J., *Solid oxide fuel cell cathodes: Polarization mechanisms and modeling of the electrochemical performance.* Annual Review of Materials Research, 2003. **33**: p. 361-382.

8. Brichzin, V., et al., *The geometry dependence of the polarization resistance of Sr-doped LaMnO3 microelectrodes on yttria-stabilized zirconia.* Solid State Ionics, 2002. **152-153**: p. 499-507.

9. Horita, T., et al., *Oxygen reduction sites and diffusion paths at La0.9Sr0.1MnO3-x/yttria-stabilized zirconia interface for different cathodic overvoltages by secondary-ion mass spectrometry.* Solid State Ionics, 2000. **127**(1-2): p. 55-65.

10. Dusastre, V. and J.A. Kilner, *Optimisation of composite cathodes for intermediate temperature SOFC applications.* Solid State Ionics, 1999. **126**(1-2): p. 163-174.

11. Jorgensen, M.J. and M. Mogensen, *Impedance of solid oxide fuel cell LSM/YSZ composite cathodes.* Journal of The Electrochemical Society, 2001. **148**(5): p. A433-A442.

12. Juhl, M., et al. *Performance/structure correlation for composite SOFC cathodes*. 1996.

13. Murray, E.P. and S.A. Barnett, *(La,Sr) MnO3-(Ce,Gd)O2-x composite cathodes for solid oxide fuel cells.* Solid State Ionics, 2001. **143**(3-4): p. 265-273.

14. Song, H.S., et al., *Effect of starting particulate materials on microstructure and cathodic performance of nanoporous LSM-YSZ composite cathodes.* Journal of Power Sources, 2007. **167**(2): p. 258-264.

15. Song, H.S., et al., *Influences of starting particulate materials on microstructural evolution and electrochemical activity of LSM-YSZ composite cathode for SOFC.* Journal of Electroceramics, 2006. **17**(2-4): p. 759-764.

16. McIntosh, S., et al., *Effect of polarization on and implications for characterization of LSM-YSZ composite cathodes.* Electrochemical and Solid State Letters, 2004. **7**(5): p. A111-A114.

17. Sasaki, K., et al., *Microstructure-property relations of solid oxide fuel cell cathodes and current collectors - Cathodic polarization and ohmic resistance.* J. Electrochem. Soc., 1996. **143**(2): p. 530-543.

18. Jorgensen, M.J., et al., *Effect of sintering temperature on microstructure and performance of LSM-YSZ composite cathodes.* Solid State Ionics, 2001. **139**(1-2): p. 1-11.

19. Schneider, L.C.R., et al., *Discrete modelling of the electrochemical performance of SOFC electrodes.* Electrochimica Acta, 2006. **52**(1): p. 314-324.

20. Ji, Y., K. Yuan, and J.N. Chung, *Monte-Carlo simulation and performance optimization for the cathode microstructure in a solid oxide fuel cell.* Journal of Power Sources, 2007. **165**(2): p. 774-785.

21. Abbaspour, A., et al., *A novel approach to study the structure versus performance relationship of SOFC electrodes.* Journal of Power Sources, 2006. **161**(2): p. 965-970.

22. Han, D.G. and G.M. Choi, *Computer simulation of the electrical conductivity of composites: the effect of geometrical arrangement.* Solid State Ionics, 1998. **106**(1-2): p. 71-87.

23. Costamagna, P., P. Costa, and E. Arato, *Some more considerations on the optimization of cermet solid oxide fuel cell electrodes.* Electrochimica Acta, 1998. **43**(8): p. 967-972.

24. Sunde, S., *Calculation of conductivity and polarization resistance of composite SOFC electrodes from random resistor networks.* Journal of The Electrochemical Society, 1995. **142**(4): p. L50-L52.

25. Sunde, S., *Monte Carlo simulations of conductivity of composite electrodes for solid oxide fuel cells.* Journal of The Electrochemical Society, 1996. **143**(3): p. 1123-1132.

26. Kenney, B., et al., *Computation of TPB length, surface area and pore size from numerical reconstruction of composite solid oxide fuel cell electrodes.* Journal of Power Sources, 2009. **189**(2): p. 1051-1059.

27. Wang, C.Y., et al. *Characterization and microstructure of nanstructrued LSM/YSZ composite cathode for high performance SOFC*. in *Risø International Symposium on Materials Science:Solid State Electrochemistry*. 2005. Denmark.

28. Tarte, L.A.L., et al., *Advanced Characterization Methods for Solid Oxide Fuel Cell Materials.* Microsc Microanal, 2005. **11**(Suppl 2).

29. Singhal, S.C., *Advances in solid oxide fuel cell technology.* Solid State Ionics, 2000. **135**(1-4): p. 305-313.

30. Mogensen, M., N.M. Sammes, and G.A. Tompsett, *Physical, chemical and electrochemical properties of pure and doped ceria.* Solid State Ionics, 2000. **129**(1-4): p. 63-94.

31. Strickler, D.W. and W.G. Carlson, *IONIC CONDUCTIVITY OF CUBIC SOLID SOLUTIONS IN THE SYSTEM CAO-Y2O3-ZRO2.* Journal of the American Ceramic Society, 1964. **47**(3): p. 122-127.

32. Zuo, C.D., et al., *Ba(Zr0.1Ce0.7Y0.2)O3-delta as an electrolyte for low-temperature solid-oxide fuel cells.* Advanced Materials, 2006. **18**(24): p. 3318-+.

33. Yang, L., et al., *A novel composite cathode for low-temperature SOFCs based on oxide proton conductors.* Advanced Materials, 2008. **20**(17): p. 3280-+.

34. Lin, B., et al., *Intermediate-to-low temperature protonic ceramic membrane fuel cells with Ba0.5Sr0.5Co0.8Fe0.2O3-delta-BaZr0.1Ce0.7Y0.2O3-delta composite cathode.* Journal of Power Sources, 2009. **186**(1): p. 58-61.

35. Zhao, L., et al., *High performance of proton-conducting solid oxide fuel cell with a layered PrBaCo2O5+delta cathode.* Journal of Power Sources, 2009. **194**(2): p. 835-837.

36. Yang, L., et al., *A mixed proton, oxygen ion, and electron conducting cathode for SOFCs based on oxide proton conductors.* Journal of Power Sources, 2010. **195**(2): p. 471-474.

37. Lee, S., et al., *Performance of Ni/Y2O3-stabilized ZrO2 cermet cathode prepared by mechanical alloying for high-temperature electrolysis of water vapor.* Japanese Journal of Applied Physics, 2008. **47**(3): p. 1838-1844.

38. San Ping, J. and C. Siew Hwa, *A review of anode materials development in solid oxide fuel cells.* Journal of Materials Science, 2004. **39**(14): p. 4405-4439.

39. Sunde, S., *Simulations of composite electrodes in fuel cells.* Journal of Electroceramics, 2000. **5**(2): p. 153-182.

40. Mebane, D.S., *Impedance Response of Alumina-silicon Carbide Whisker Composites*, in *Materials Science and Engineering*. 2004, Georgia Institute of Techology: Atlanta.

41. Bieberle, A. and L.J. Gauckler, *Reaction mechanism of Ni pattern anodes for solid oxide fuel cells.* Solid State Ionics, 2000. **135**(1-4): p. 337-345.

42. Jiang, S.P., *Activation, microstructure, and polarization of solid oxide fuel cell cathodes.* Journal of Solid State Electrochemistry, 2006. **11**(1): p. 93-102.

43. Choi, J.H., J.H. Jang, and S.M. Oh, *Microstructure and cathodic performance of La0.9Sr0.1MnO3/yttria-stabilized zirconia composite electrodes.* Electrochimica Acta, 2001. **46**(6): p. 867-874.

44. Deseure, J., et al., *Modelling the porous cathode of a SOFC: oxygen reduction mechanism effect.* Journal of Applied Electrochemistry, 2007. **37**(1): p. 129-136.

45. Mogensen, M. and S. Skaarup, *Kinetic and geometric aspects of solid oxide fuel cell electrodes.* Solid State Ionics, 1996. **86-88**(Part 2): p. 1151-1160.

46. Chen, X.J., S.H. Chan, and K.A. Khor, *Simulation of a composite cathode in solid oxide fuel cells.* Electrochimica Acta, 2004. **49**(11): p. 1851-1861.

47. Kenney, B. and K. Karan. *Mathematical Micro-Model of a Solid Oxide Fuel Cell Composite Cathode*. in *Hydrogen and Fuel Cells*. 2004.

48. Jiang, S., *Development of lanthanum strontium manganite perovskite cathode materials of solid oxide fuel cells: a review.* Journal of Materials Science, 2008. **43**(21): p. 6799-6833.

49. Tewari, A., A.M. Gokhale, and R.M. German, *Effect of gravity on three-dimensional coordination number distribution in liquid phase sintered microstructures.* Acta Materialia, 1999. **47**(13): p. 3721-3734.

50. Tewari, A. and A.M. Gokhale, *Nearest neighbor distances in uniform-random poly-dispersed microstructures.* Materials Science and Engineering a-Structural Materials Properties Microstructure and Processing, 2005. **396**(1-2): p. 22-27.

51. Wang, C.Y., et al. *CHARACTERIZATION AND MICROSTRUCTURE OF NANOSTRUCTURED LSM/YSZ COMPOSITE CATHODE FOR HIGH PERFORMANCE SOFC*. in *Risø International Symposium on Materials Science:Solid State Electrochemistry*. 2005. Denmark.

52. Yang, C.C.T., W.C.J. Wei, and A. Roosen, *Electrical conductivity and microstructures of La0.65Sr0.3MnO3-8 mol% yttria-stabilized zirconia.* Materials Chemistry and Physics, 2003. **81**(1): p. 134-142.

53. Wilson, J., et al., *Structural and Electrochemical Characterization of* $La_{0.8}Sr_{0.2}MnO_3$ - Y_2O_3*-Stabilized* ZrO_2 *(LSM-YSZ) Cathodes with Varying Composition*, in *33rd International Conference & Exposition on Advanced Ceramics & Composites*. 2009.

54. Wilson, J.R., et al., *Quantitative three-dimensional microstructure of a solid oxide fuel cell cathode.* Electrochemistry Communications, 2009. **11**(5): p. 1052-1056.

55. Wilson, J.R., et al., *Three-dimensional reconstruction of a solid-oxide fuel-cell anode.* Nature Materials, 2006. **5**: p. 541-544.

56. Thydén, K., Y.L. Liu, and J.B. Bilde-Sørensen, *Microstructural characterization of SOFC Ni-YSZ anode composites by low-voltage scanning electron microscopy.* Solid State Ionics, 2008. **178**(39-40): p. 1984-1989.

57. Mouton, P.R., *Principles and Practices of Unbiased Stereology: An Introduction for Bioscientists*. 2002, Baltimore, MD: The Johns Hopkins University Press.

58. Underwood, E.E., *Quantitative Stereology*. 1970, Massachusetts: Addison Wesley Publishing Co.,Reading.

59. DeHoff, R.T. and F.N. Rhines, *Quantitative Microscopy*. 1968, New York, NY: McGraw Hill Publishing Co.

60. Debye, P., J.H.R. Anderson, and H. Brumberger, *Scattering by an Inhomogeneous Solid. II. The Correlation Function and Its Application.* Journal of Applied Physics, 1957. **28**(6): p. 679-683.

61. Saheli, G., H. Garmestani, and A. Gokhale, *Homogenization relations for elastic properties of two-phase composites using two-point statistical functions.* Journal of Mechanics of Materials and Structures, 2008. **3**(1): p. 85-106.

62. Gokhale, A.M., A. Tewari, and H. Garmestani, *Constraints on microstructural two-point correlation functions.* Scripta Materialia, 2005. **53**(8): p. 989-993.

63. Costa, C.A.R., et al., *Eutectic alloy microstructure: atomic force microscopy analysis.* Applied Surface Science, 2005. **240**(1-4): p. 414-423.

64. Kendall, M.G. and P.A.P. Moran, *Geometrical probability*. 1963, New York: Hafner Pub.

65. Avrami, M., *Kinetics of phase change I - General theory.* Journal of Chemical Physics, 1939. **7**(12): p. 1103-1112.

66. Avrami, M., *Granulation, Phase Change, and Microstructure - Kinetics of Phase Change. III.* Journal of Chemical Physics, 1941. **9**(2): p. 177-184.

67. Johnson, W.A. and R.F. Mehl, *Reaction kinetics in processes of nucleation and growth.* Transactions of the American Institute of Mining and Metallurgical Engineers, 1939. **135**: p. 416-442.

68. Bhadeshia, H.K.D.H., *Kinetics of simultaneous transformations.* Solid-Solid Phase Transform., [Int. Conf.], 4th, 1999(Pt. 2): p. 1445-1452.

69. Jones, S.J. and H.K.D.H. Bhadeshia, *Kinetics of the simultaneous decomposition of austenite into several transformation products.* Acta Mater., 1997. **45**(7): p. 2911-2920.

70. Kasuya, T., et al., *Real and extended volumes in simultaneous transformations.* Mater. Sci. Technol., 1999. **15**(4): p. 471-473.

71. Matheron, G., *Random sets and integral geometry*. 1974, New York: Wiley.

72. Meijering, J.L., *Interface area, edge length, and number of vertices in crystal aggregates with random nucleation.* Philips Research Reports, 1953. **8**(4): p. 270-290.

73. Miles, R. *On estimating aggregate and overall characteristics from thick sections by transmission microscopy*. in *Fourth International Congresss for Stereology*. 1975. NBS, Gaithersbug, Md.: National Bureau of Standards Special Publication.

74. Gokhale, A.M., *Quantitative Characterization and Representation of Global Microstructural Geometry,* in *ASM Handbook: Metallography, and Microstructures*. 2004. p. 428-447.

75. Ohser, J. and F. Muecklich, *Statistical Analysis of Microstructures in Material Science*. 2000, New York: J. Wiley & Sons.

76. Santalo, L.A., *Integral Geometry and Geometric Probability*. 1976, Mass.: Addison-Wesley Publishing Co., Reading.

77. Stoyan, D., S. Kendall, and J. Mecke, *Stochastic Geometry and its Applications*. 2nd ed. 1995, NY: John Wiley and Sons.

78. Smith, C.S. and L. Guttman, *Measurement of internal boundaries in three-dimensional structures by random sectioning.* J. Met., 1953. **5**(Trans.): p. 81-7.

79. Kreyszig, E., *Advanced Engineering Mathematics*. 1998: Wiley.

80. Hays, W., *Statistics*. 4th ed. 1988: Holt McDougal.

81. Juhl, M., et al., *Performance/structure correlation for composite SOFC cathodes.* Journal of Power Sources, 1996. **61**(1-2): p. 173-181.

82. Jiang, S.P., *Issues on development of (La,Sr)MnO3 cathode for solid oxide fuel cells.* Journal of Power Sources, 2003. **124**(2): p. 390-402.

83. DeHoff, R.T., in *Treatise on Materials Science and Technology*. 1972, Academic Press: New York, NY. p. 247.

84. Gokhale, A.M., C.V. Iswaran, and R.T. DeHoff, *Application of Microstructure Modeling to Kinetics of Recrystallization.* Metallurgical Transactions A, 1980. **11A**: p. 1377-1382.

85. Gokhale, A.M., *A Test for Randomness of Spatial Distribution of Particles.* Metall. Trans. A, 1984. **15A**: p. 243-245.

86. Wilson, J.R., et al., *Three-dimensional reconstruction of a solid-oxide fuel-cell anode.* Nature Materials, 2006. **5**: p. 541-544.

87. Torquato, S., *Random Heterogeneous Materials: Microstructure and Macroscopic Properties*. 2001: Springer.

88. Fog, A. (2001) *Chaotic Random Number Generators with Random Cycle Lengths*. http://www.agner.org/random/theory/, accessed on 7/1/2010.

89. Tola, E. 2006, http://cvlab.epfl.ch/~tola/index.html, accessed on 4/23/2009.